

CIAMTIS

U.S. DOT Region 3 University Transportation Center

Bridge Load Rating and Evaluation Using Digital Image Measurements

May 9, 2022

Prepared by:

L. Timber, M. Head, H. W. Shenton, M. J. Chajes (University of Delaware);
M. Ghyabi, D. Lattanzi, R. Jahangiri, W. C. Graves (George Mason University)

r3utc.psu.edu



PennState
College of Engineering

LARSON
TRANSPORTATION
INSTITUTE

1. Report No. CIAM-UTC-REG3	2. Government Accession No.	3. Recipient's Catalog No.	
4. Title and Subtitle Bridge Load Rating and Evaluation Using Digital Image Measurements		5. Report Date May 9, 2022	6. Performing Organization Code
7. Author(s) Luke Timber https://orcid.org/0000-0003-0955-2138 , Monique Head https://orcid.org/0000-0002-0608-9961 , Harry W. Shenton https://orcid.org/0000-0002-9179-1148 , Michael J. Chajes https://orcid.org/0000-0003-1535-2140 (University of Delaware); Mehrdad Ghyabi https://orcid.org/0000-0003-2652-426X , David Lattanzi https://orcid.org/0000-0001-9247-0680 , Reza Jahangiri https://orcid.org/0000-0003-3876-6223 , William C. Graves https://orcid.org/0000-0001-9094-7334 (George Mason University)		8. Performing Organization Report No.	
9. Performing Organization Name and Address University of Delaware 127 The Green Newark, DE 19716		10. Work Unit No. (TRAIS)	11. Contract or Grant No. 69A3551847103
12. Sponsoring Agency Name and Address U.S. Department of Transportation Research and Innovative Technology Administration 3rd Fl, East Bldg E33-461 1200 New Jersey Ave, SE Washington, DC 20590		13. Type of Report and Period Covered Final Report 03/18/2019 – 12/18/2021	
15. Supplementary Notes Work funded through The Pennsylvania State University through the University Transportation Center Grant Agreement, Grant No. 69A3551847103.		14. Sponsoring Agency Code	
16. Abstract The use of digital imaging and other vision-based measurements offers many options for conducting load tests and obtaining the necessary data without having direct contact on the bridge via mounted sensor arrays. The results from this study revealed the sensitivity and accuracy of displacement measurements when compared to measurements from conventional string potentiometers mounted directly to the flange of the girder and 3D point cloud measurements. While there is not one optimal technique for measuring structural displacements based on a video, different techniques have different performance levels, and the applicability of these various methods may vary from case to case. The goal of this study was to compare the performance and accuracy of vision-based displacement measurements in the form of load testing on two bridges in Delaware, and how the data can be used to calibrate finite element models to assess bridge performance based on in-situ conditions. Results from the two diagnostic loads tests are presented. Using the data collected, results are compared to AASHTO live load distribution factors. A finite element bridge model is generated in ABAQUS and calibrated using the field measurements obtained from digital imaging. From the findings, a process to evaluate live load distribution using displacements obtained from vision-based measurement techniques is presented. Lessons learned and the impact of the vision-based measurement techniques deployed for load testing and evaluation are also presented.			
17. Key Words Bridge evaluation; load testing; load rating; video-based displacement measurements; sensors; live load distribution factors		18. Distribution Statement No restrictions. This document is available from the National Technical Information Service, Springfield, VA 22161	
19. Security Classif. (of this report) Unclassified	20. Security Classif. (of this page) Unclassified	21. No. of Pages 79	22. Price

DISCLAIMER

The contents of this report reflect the views of the authors, who are responsible for the facts and the accuracy of the information presented herein. This document is disseminated in the interest of information exchange. The report is funded, partially or entirely, by a grant from the U.S. Department of Transportation's University Transportation Centers Program. However, the U.S. Government assumes no liability for the contents or use thereof.

Table of Contents

List of Tables	Iv
List of Figures	V
CHAPTER 1: INTRODUCTION.....	1
Background.....	1
Objectives	2
Literature Review.....	3
Bridge Load Testing.....	3
Bridge Load Rating and Evaluation.....	3
Sensor Measurements Used for Bridge Load Testing.....	4
CHAPTER 2: METHODOLOGY.....	7
Overview.....	7
Case Study: Bridge 1-911S.....	9
Case Study: Bridge 1-213	13
CHAPTER 3: FINDINGS.....	16
Bridge Live Load Test Results.....	16
Case Study: Bridge 1-911S.....	16
Case Study: Bridge 1-213	27
CHAPTER 4: RECOMMENDATIONS.....	66
Live Load Distribution Factors Using Deflection Measurements	66
Discussion.....	67
Lessons Learned	68
Summary	69
Future Work.....	70
REFERENCES.....	71

List of Tables

Table 1. 1-911S schedule of rolling passes for load tests	11
Table 2. 1-213 schedule of rolling passes for load tests	15
Table 3. 1-911S girder midspan displacement comparison	24
Table 4. Live load distribution factors (LLDF) for lane 1 truck pass	25
Table 5. Live load distribution factors (LLDF) for lanes 1 and 2 tandem truck pass	25
Table 6. Comparison of LLDFs for deflection computed using various methods	26
Table 7. Comparison of LLDFs for moment computed using various methods	26
Table 8. 1-213 girder midspan displacement comparison	53
Table 9. Live load distribution factors (LLDF) for left lane truck pass	53
Table 10. Live load distribution factors (LLDF) for right lane truck pass	54
Table 11. Live load distribution factors (LLDF) for tandem lane truck pass	54
Table 12. Comparison of LLDFs for deflection computed using various methods	56
Table 13. Comparison of LLDFs for moment computed using various methods	56
Table 14. 1-213 bridge model midspan deflection comparison of concrete compressive strength versus load test readings	57
Table 15. Rotational displacement of all girders based on concrete compressive strength	57
Table 16. 1-213 bridge model midspan deflection comparison of boundary condition versus load test readings	58
Table 17. Comparison of LLDFs for deflection	65
Table 18. Comparison of LLDFs for moment	65

List of Figures

Figure 1. Overview of instrumentation placement under bridge	7
Figure 2. Overview of point cloud analysis methodology	8
Figure 3. Placement of fiducial elements.....	9
Figure 4. Bridge 1-911S cross-sectional view	10
Figure 5. Bridge 1-911S load test instrumentation plan	10
Figure 6. Single truck rolling pass (Test 1).....	11
Figure 7. Imetrum target locations (a): 1-911S, (b) 1-213	12
Figure 8. Bridge 1-213 cross-sectional view	13
Figure 9. Bridge 1-213 load test instrumentation plan	14
Figure 10. Imetrum Camera 33 field of view for DE 1-213 bridge load test	15
Figure 11. 1-911S Test 1 Imetrum Midspan Deflection	17
Figure 12. 1-911S Test 1 String pot Midspan Deflection	17
Figure 13. 1-911S Test 2 Imetrum Midspan Deflection	18
Figure 14. 1-911S Test 2 String pot Midspan Deflection	18
Figure 15. 1-911S Test 1 Midspan Bottom Flange BDI Microstrain.....	19
Figure 16. 1-911S Test 2 Midspan Bottom Flange BDI Microstrain	19
Figure 17. 1-911S Test 3 Imetrum Midspan Deflection	21
Figure 18. 1-911S Test 3 String pot Midspan Deflection	21
Figure 19. 1-911S Test 4 Imetrum Midspan Deflection	22
Figure 20. 1-911S Test 4 String pot Midspan Deflection	22
Figure 21. 1-911S Test 3 Midspan Bottom Flange BDI Microstrain	23
Figure 22. 1-911S Test 4 Midspan Bottom Flange BDI Microstrain	23
Figure 23. Comparison of measurement methods: (a) strong correlation of results for fascia girder nearest to the phase-based camera and (b) inaccurate results for the phase-based approach	24
Figure 24. 1-213 Test 1 Imetrum Midspan Deflection	28
Figure 25. 1-213 Test 1 String pot Midspan Deflection	28
Figure 26. 1-213 Test 2 Imetrum Midspan Deflection	29
Figure 27. 1-213 Test 2 String pot Midspan Deflection	29
Figure 28. 1-213 Test 1 Midspan Bottom Flange BDI Microstrain.....	30
Figure 29. 1-213 Test 2 Midspan Bottom Flange BDI Microstrain.....	30
Figure 30. 1-213 Test 3 Imetrum Midspan Deflection	32
Figure 31. 1-213 Test 3 String pot Midspan Deflection	32
Figure 32. 1-213 Test 4 Imetrum Midspan Deflection	33
Figure 33. 1-213 Test 4 String pot Midspan Deflection	33
Figure 34. 1-213 Test 9 Imetrum Midspan Deflection	34
Figure 35. 1-213 Test 9 String pot Midspan Deflection	34
Figure 36. 1-213 Test 3 Midspan Bottom Flange BDI Microstrain	35
Figure 37. 1-213 Test 3 Midspan Bottom Flange BDI Microstrain	35
Figure 38. 1-213 Test 9 Midspan Bottom Flange BDI Microstrain	36
Figure 39. 1-213 Test 5 Imetrum Truck 1 Midspan Deflection	37
Figure 40. 1-213 Test 5 String pot Truck 1 Midspan Deflection	37

Figure 41. 1-213 Test 5 Imetrum Truck 1 Midspan Deflection.....	38
Figure 42. 1-213 Test 5 String pot Truck 2 Midspan Deflection.....	38
Figure 43. 1-213 Test 6 Imetrum Truck 1 Midspan Deflection.....	39
Figure 44. 1-213 Test 6 String pot Truck 1 Midspan Deflection	39
Figure 45. 1-213 Test 6 Imetrum Truck 2 Midspan Deflection	40
Figure 46. 1-213 Test 6 String pot Truck 2 Midspan Deflection	40
Figure 47. 1-213 Test Truck 1 Midspan Bottom Flange BDI Microstrain	41
Figure 48. 1-213 Test 5 Truck 2 Midspan Bottom Flange BDI Microstrain	41
Figure 49. 1-213 Test 6 Truck 2 Midspan Bottom Flange BDI Microstrain	42
Figure 50. 1-213 Test 6 Truck 2 Midspan Bottom Flange BDI Microstrain	42
Figure 51. 1-213 Test 7 Imetrum Midspan Deflection	44
Figure 52. 1-213 Test 7 String pot Midspan Deflection	44
Figure 53. 1-213 Test 8 Imetrum Midspan Deflection	45
Figure 54. 1-213 Test 8 String pot Midspan Deflection	45
Figure 55. 1-213 Test 7 Midspan Bottom Flange BDI Microstrain.....	46
Figure 56. 1-213 Test 8 Midspan Bottom Flange BDI Microstrain.....	46
Figure 57. 1-213 Truck Left Lane Rolling Passes Midspan Girder Deflection	47
Figure 58. 1-213 Truck Right Lane Rolling Passes Midspan Girder Deflection	48
Figure 59. 1-213 Truck Tandem Lane Rolling Passes Midspan Girder Deflection	48
Figure 60. 1-213 Truck Left Lane Rolling Passes Midspan Bottom Flange BDI Microstrain	49
Figure 61. 1-213 Truck Right Lane Rolling Passes Midspan Bottom Flange BDI Microstrain	50
Figure 62. 1-213 Truck Tandem Lane Rolling Passes Midspan Bottom Flange BDI Microstrain	50
Figure 63. 1-213 Truck Left Lane Rolling Passes Live Load Distribution Factors.....	51
Figure 64. 1-213 Truck Right Lane Rolling Passes Live Load Distribution Factors.....	51
Figure 65. 1-213 Truck Tandem Lane Rolling Passes Live Load Distribution Factors	52
Figure 66. Underside of bridge superstructure photo and ABAQUS model (ABAQUS/CAE 2019)	55
Figure 67. Bridge Section View and Truck Axle Locations.....	58
Figure 68. 1-213 Field Test Tandem Truck Pass Photos (a) and (b)	59
Figure 69. 1-213 Truck Tandem Lane Rolling Passes Live Load Distribution Factors	60
Figure 70. 1-213 Imetrum and F.E.M. Truck Tandem Lane Rolling Passes Midspan Girder Deflection ..	61
Figure 71. 1-213 Imetrum and F.E.M. Truck Tandem Lane Rolling Passes Midspan Girder Deflection ..	62
Figure 72. 1-213 Imetrum and F.E.M. Truck Tandem Lane Rolling Passes Deflection LLDFs.....	63
Figure 73. 1-213 Imetrum and F.E.M. Truck Tandem Lane Rolling Passes Strain LLDFs	64

CHAPTER 1

Introduction

BACKGROUND

In the United States, bridges are required to be inspected for damage and deterioration within a 2-year period (Bell et al., 2013; AASHTO, 2016). Visual inspection has been found to be the most common form of inspection (Moore et al. 2001). Many state departments of transportation (DOTs) have adopted their own inspection procedures that exceed what is required by National Bridge Inspection Standards (NBIS) (NYSDOT 2007). Inspection results and condition and operating rating data can be used in part for asset management and understanding existing bridge conditions. Load testing is one load rating method that can be used when calculations and engineering models do not reveal satisfactory performance of a bridge (Alampalli et al. 2019) and more information is needed for assessment. Results from load testing may allow a bridge to remain in-service but with posted weight limits (Bell et al. 2013; AASHTO 2003). As of 2016, 0.6 percent of the bridges in the NBI were load rated using load testing (Alipour et al. 2019). This infrequency in load testing can be attributed to its associated costs and challenges to access the bridge, purchase data acquisition systems, physically mount sensors to the bridge, and potentially disrupt traffic, in some cases. However, useful information can be obtained from a load test to assess in-situ conditions, especially in terms of understanding lateral load distribution.

Replacing multiple discrete strains measurements with full field digital image correlation opens the door to making bridge testing easier, less expensive, and much more common as a solution to address the grand challenge of determining how and what is needed to properly allocate resources for deteriorating and aging bridges. To address some of these challenges associated with load testing, non-contact, advanced technologies have emerged over the years to offset some of the time-consuming processes like installing sensor arrays. For example, vision-based measurement systems have made more headway for structural applications and offer several advantages compared to traditional non-vision sensors that are directly mounted to a structure. Vision-based measurements reduce safety risks, add the ease of a contactless setup, and increase the versatility of managing different fields of view to gain measurements at varying locations along the structure (Sutton et al., 2009). Non-contact optical technology, computer vision-based and global positioning systems (GPS) based technology are currently popular methods to capture bridge displacements. There are sometimes issues with the alternatives such as high equipment cost, low sampling rate, and low resolution. GPS devices can measure static displacements in real-time; however, the current state of GPS technology limits these devices exclusively applicable to flexible structures, which have lower natural frequency ranges (Sohn et al., 2003). Contactless displacement sensing techniques have been heavily studied in recent years as an alternative to accelerometers. Laser vibrometry (Stanbridge et al. 2000) and microwave interferometry (Farrar et al. 1999) are examples of noncontact displacement sensing methods that have been studied before. One of the categories of contactless displacement measurement techniques is using digital cameras to record the intensity of visible light that is reflected from the surface of structures. Video cameras have different speeds (frequency) and precision (resolution). One can select

the appropriate camera for a specific case of displacement measurement. The challenging part of using video cameras as contactless sensors requires the recorded videos to be processed to extract displacement-related data from them (Chen et al. 2015). Fortunately, image processing and video-based computer vision approaches have matured over the past decade, though how these approaches work for full-scale bridge testing remains an understudied problem. Capturing non-contact, video-based measurements to quantify bridge deformations offers many advantages, especially when access to a bridge is limited and attaching sensor arrays becomes too tedious and physically challenging for precise sensor placement.

OBJECTIVES

The primary objective of this project is to develop and implement a procedure for determining live-load lateral distribution of bridges using non-contact, video-based measurements during full-scale load testing of a bridge, where methods to understand these measurements at full-scale and considering environmental and logistical conditions have been less studied (Brownjohn et al. 2017; Ye et al. 2016; Sony et al. 2019). The research team from the University of Delaware and George Mason University performed load tests on two bridges in Delaware using both contact and non-contact, video-based measurement techniques to develop methodologies to evaluate displacement measurements of girders at midspan from three main sources:

1. Video-based digital image correlation system (i.e., Imetrum with VideoGauge™ software)
2. Video-based computer vision
3. 3D point cloud

The measurements are compared to string-potentiometers attached to the bridge and strain gauges from Bridge Diagnostics Inc. (BDI) attached to the bottom flange of a bridge girder. The non-contact measurements collected from bridge live-load tests are analyzed and used to generate finite element models based on the strain and displacement measurements obtained from a commercial, vision-based digital image correlation system—Imetrum with VideoGauge™ software. Distribution factors generated from load tests and bridge models are compared to AASHTO methodology for determining live-load distribution factors (LLDF). In addition to using these measurements to calibrate more refined finite element models, strain and displacement distributions are compared and show similar distributions for the studied bridges, which may be used to inform bridge load rating and evaluation, which are typically based on strain, not displacement measurements, as described in the *Manual for Bridge Evaluation* (MBE) (AASHTO, 2018).

LITERATURE REVIEW

Bridge Load Testing

Bridge load testing is one load rating method that can be used when calculations and engineering models do not reveal satisfactory performance of a bridge (Alampalli et al. 2019) and more information is needed for assessment. Results from load testing may allow a bridge to remain in-service but with posted weight limits (Bell et al. 2013; AASHTO 2003). As of 2016, 0.6 percent of the bridges in the NBI were load rated using load testing (Alipour et al. 2019). There are two main types of load tests that can be conducted to evaluate a bridge response: (1) diagnostic load test and (2) proof load test. The load-carrying capacity of a bridge can be deduced from measured static and quasi-static displacements of a bridge deck due to heavy trucks. Load testing commonly consists of applying loading scenario(s), which evokes a response in the structural system that is indicative of operation load demands placed on the structure. Each load pass scenario is typically performed to elicit a particular response measurement (e.g., deflection, strain, acceleration, rotation). Recommendations to load rate bridges that lack existing as-built information are provided within the MBE (AASHTO, 2018) via load testing. Additional guidelines for both load tests are provided within the National Cooperative Highway Research Program (NCHRP, 1998).

A diagnostic load test deploys a predetermined load, which is close in gross vehicular weight to the bridge's load-carrying capacity, placed at several locations along the bridge to discern and quantify its response. Analytical models are used to compare theoretical measurements to what was measured in the field in one or more critical members. The results of diagnostic tests are used to verify and calibrate the analytical models. The calibrated model is then utilized to compute load-rating factors (AASHTO, 2018). From a survey submitted to the 50 state departments of transportation (DOTs) (Cuaron et al., 2020), 52% of those who responded said that they conduct load tests. The survey found that diagnostic tests were the most common method.

A proof load test consists of a set of loads, and the bridge response is monitored to ascertain whether the bridge can carry the assigned load without damage. To identify early signs of nonlinear behavior or distress, loads are applied in incremental order (AASHTO, 2018). The MBE (AASHTO, 2018) divides suitable candidate bridges for proof load tests into two groups: "known" and "hidden" bridges. The structural makeup of "known" bridges is known and could be analytically load rated. Proof load tests are viable for this type of bridge when calculated load ratings are low and load testing could provide quantifiable results and higher ratings (AASHTO, 2018). "Hidden" bridges are those without design plans or sufficient as-builts in which a load rating cannot be conducted due to insufficient information on their internal details and configuration (AASHTO, 2018). For "hidden" bridges, a proof load test is required to determine live-load capacity. The procedure for load rating bridges through load testing can be found in the MBE section 8.8 (AASHTO, 2018).

Bridge Load Rating and Evaluation

The *Manual for Bridge Evaluation* (AASHTO, 2018) sets forth standards for the load rating and posting of existing bridges. These standards are intended to be applied when evaluating commonly used types of highway bridges in the United States that are subjected to permanent and vehicular loads. Additional considerations and loadings beyond the MBE evaluation criteria must be considered for rating of complex and long span-bridges. The aforementioned information is applied to perform structural analysis to determine the forces and stresses caused by AASHTO and standard state agency legal loads. The load rating is then determined by comparing the forces and stresses with the strength limit state of the bridge. The MBE (AASHTO, 2018) maintains three load rating methods: Load and Resistance Factor Rating (LRFR), Load

Factor Rating (LFR), and Allowable Stress Rating (ASR). The LRFR method came to fruition to allot uniform reliability in bridge load rating, load posting, and permit decisions. The LFR method uses load factors to account for the uncertainty innate in load calculations to provide safety standard for bridge load rating. The ASR method merges the actual applied loadings to determine a maximum stress in bridge members, which shall not exceed the working or allowable stress. The MBE places no preference on rating method; however, common practice uses the rating method in line with the originally utilized design philosophy. Useful information can be obtained from a load test to assess in-situ conditions, especially in terms of understanding lateral live-load distribution.

Current AASHTO LRFD live-load distribution factors include parameters such as span length, slab thickness, and beam spacing. The research performed under the NCHRP Project 12-26 provided the groundwork for the moment and shear distribution factors used currently in AASHTO Section 4.6.2.2 (Zokaie, 2000). Current AASHTO Section 4.6.2.2 standards implement different formulas for numerous bridge types: slab bridges, multicell box girder, side-by-side and spread box beams, and beam-and-slab (reinforced concrete T-beam, prestressed concrete I-girder, and steel I-girder). The positioning of the live load is one of the key items in calculation of distribution factor. Grillage or finite-element analysis is acceptable as an accurate analysis for determining load distribution. The model must be prepared carefully to appropriately represent the behavior of the bridge. LRFD specifications use a factor that is found by using the lane load (full axle load) rather than wheel loads (Barker and Puckett, 2013). Live load and the capacity of a girder relative to the live load are points of interest for load ratings. The *Manual for Condition Evaluation and Load Rating of Highway Bridges Using Load Resistance Factor Philosophy* (NCHRP, 2001) specifies load ratings as rating factor for a particular live-load model. The primary focus of bridge load rating is the evaluation of the safety of bridges for live loads and fatigue. Engineering judgement is necessary in concluding an applicable bridge rating factor to preserve the safe use of the bridge and evaluating the need for assigning posting and permit decisions on the bridge (AASHTO, 2018).

Sensor Measurements Used for Bridge Load Testing

In this research project, the research team from the University of Delaware and George Mason University performed load tests on two bridges in Delaware using both contact and non-contact, video-based measurement techniques to develop methodologies to evaluate displacement measurements of girders at midspan.

Contact Sensors

Conventional contact sensors deployed for load testing consisted of strain gauges and string potentiometers, referred to later in this report as “stringpots.” In most diagnostic tests, strain data at specific locations are required, and the locations depend on the objectives of the test. Strain sensors are typically placed on critical members, where the response is recorded under static and quasi-static loading. Separate types of gauges are available for concrete and steel structures. The most frequently utilized sensors for field measurement of strains are vibrating wire gauges, strain transducers, weldable gauges, and bonded gauges. Vibrating wire gauges utilize a thin wire filament, while the other three gauge types use electric resistance strain gauges in combination with thin metal wire gauges (NCHRP, 1998).

Measuring strain has some limitations. Environmental conditions, like temperature and moisture, can impact reliability and quality specifically in the case of bonded gauges. Moisture is also a common cause of gauge failure (NCHRP, 1998). Certain adhesives used to install gauges require temperatures of 65 °F or higher to become adherent to structures. Special precautions are required when collecting strain measurements over extended periods of time due to changes in environmental conditions. Local conditions

where strain is being measured impact the accuracy of strain data; accurately measuring strain in a concrete member is challenging due to local cracking.

Common displacement-measuring instruments for bridge load testing are dial gauges and electrical transducers, which are typically in contact with the bridge for direct measurement. For measuring displacements from static loads, dial gauges are most frequently used. Setup for the gauges is easy and usually data accuracy sufficient for load tests (NCHRP 12-46, 2000). Potentiometers and linear variable differential transformers (LVDT) are electrical displacement transducers that transform displacement to proportional changes of electrical voltage. Dial gauges and electrical transducers can measure both static and dynamic displacements (NCHRP 12-46, 2000). A limitation of traditional displacement transducers is the need for a fixed reference point. In many cases, an additional temporary framework is required to provide a fixed reference point (Edberg, 1994). For overpasses, high bridges or bridges over water, installation of displacement instrumentation is challenging or impossible. Standard deflection transducers require power and signal conductors. The installation is time consuming, specifically for bridges over railways, highways, water, and bridges with high clearances.

Non-contact, Video-based Measurement Systems

Non-contact, video-based measurement systems like the commercial Imetrum system with VideoGauge™ and video-based computer vision system deployed on this project have several key advantages. The Imetrum system provides an integrated end-to-end product that includes cameras and the associated software package, minimizing setup and configuration time in the field, without the need to mount and calibrate physical sensors. Though not explicitly necessary, targets were installed on the structure in this study, and their installation was far faster and simpler than sensor systems. Digital image correlation (DIC)-based displacement computations are also not restricted in terms of the maximum amount of pixel movement allowed between images, a known issue with optical flow methods like the one used in this study (Wadhwa et al., 2013). However, this limitation was not a factor in the following case study. As with any vision-based system, there are a few disadvantages that may impact the accuracy of the measurements. Accuracy is a function of the lens' focal length, overall lighting, standoff or working distance, and skew from the camera to the point of interest. Standoff or working distance, which is the distance between the camera and the measurement object, is a key factor in understanding the uncertainty of the 2D DIC displacement data to account for skew effects or other alignment issues that could distort the field of view. Using lenses with longer focal lengths, and narrower fields of view, or measuring displacement at short working distances can decrease measurement uncertainty (Liu et al., 2016). Another key factor that can impact any computer vision method is the need to compensate for perspective distortion in the images. Calibrated targets are typically used to address this problem. Compared to laboratory-scale testing, optimizing data collection for these considerations is far more challenging under field conditions and leads to an anticipated loss of measurement accuracy.

Capturing strain measurements with digital image correlation opens the door to making bridge load testing less complex and less expensive, and overcoming accessibility challenges and the need to physically mount sensors and deploy data acquisition systems. These technologies are slowly gaining acceptance by owners and industry professionals, given the percent trade-off between performance and safety assessment. DIC provides an avenue of improvement in the ways engineers perform condition assessments and understand the in-service response due to loads. Capturing digital image measurements (DIM) and using computer vision in a non-contact way to quantify bridge deformations offer many advantages, especially when access to a bridge is limited and attaching sensor arrays becomes too tedious and physically challenging for precise sensor placement. Another disadvantage is that these techniques hardly detect subpixel motions, which is quite common in videos recorded from structures under normal loading conditions.

The Imetrum system with VideoGauge™ software uses DIC algorithms to approximate 2D displacements. For two comparative images, the 2D cross-correlation of pixel regions manually defined by the user is computed and used to provide a measure of relative displacement (Sutton et al., 2009; Yoneyama and Ueda, 2012). Standardized targets can be attached to the structure, aligned with the plane of movement under observation. While not explicitly necessary for the DIC process, these targets contain a series of sharp contrast concentric circles that improve the accuracy of the cross-correlation computation. The DIC technology supported by Imetrum (VideoGauge™) can detect displacements smaller than 1/200th of a pixel and strains smaller than three microstrain (pixel-to-pixel) (Imetrum-Website). 3D displacement measurements are possible for stereo camera configurations, but they were not considered in this study.

More recently, researchers have developed computer vision techniques to quantify displacements of structures by determining the optical flow between a pair of images. There are many optical flow computation methods, but most can be framed as optimization algorithms for computing measurements on a dense, sub-pixel basis (Shang and Shen, 2018). For this study, a phase-based optical flow method was selected and compared against the commercial Imetrum system, given its increasing usage in the research community (Wadhwa et al., 2013; Chen et al., 2015; Chen et al., 2017; Poozesh et al., 2017; Yang et al., 2017; Shang and Shen, 2018). A review of the literature suggests that phase-based optical flow is increasing in popularity due to its proven accuracy, robustness under field conditions, and computational efficiency. It was chosen here as a representative optical flow method with an established track record in bridge monitoring.

3D Point Cloud Measurements

In addition to the main study comparing video-based deformation tracking methods, this study also considered the use of photogrammetric point cloud analysis for static load testing. 3D deformation fields were computed through geometric analysis of remotely sensed point clouds generated through photogrammetric 3D reconstruction. This additional study is significant due to its use of point cloud data to measure deformations at the millimeter-scale, generally considered to be the current threshold for field-scale measurement capability (Jafari et al., 2017; Ziolkowshi et al., 2018; Cabaleiro et al., 2020). The study considered several critical aspects of the measurement process, including the point cloud registration process, metrics for quantifying deformation fields in point clouds, and practical implementation considerations.

CHAPTER 2

Methodology

OVERVIEW

This section of the report describes the methodology used for analyzing vision-based measurement systems with conventional mounted sensor arrays to measure midspan displacement measurements for two case studies of selected bridges in Delaware: 1-911S and 1-213. Strain transducers and string potentiometers (contact sensors) were attached to the bottom flanges of each girder (Figure 1). Bridge displacements were captured using the vision-based measurements per the Imetrum system and video-based computer vision techniques mentioned in the previous section. Also, 3D point cloud measurements were taken to add another dimension to the notion toward quantifying deformations when performing full-scale structural testing. One of the major benefits of the Imetrum VideoGauge™ software within the system controller is its video-based image processing technology that deploys algorithms for point-to-point tracking in the camera's field of view. For this study, two Imetrum cameras collected data and video recordings for all the rolling truck passes. The videos were postprocessed within the system controller after calibrating reference measurements within the image to determine displacement measurements of the bridge girders. The Imetrum recordings were complemented with an additional camera that recorded videos for the phase-based optical flow method used for comparative analysis. These videos were postprocessed independently using software generated by the research team.

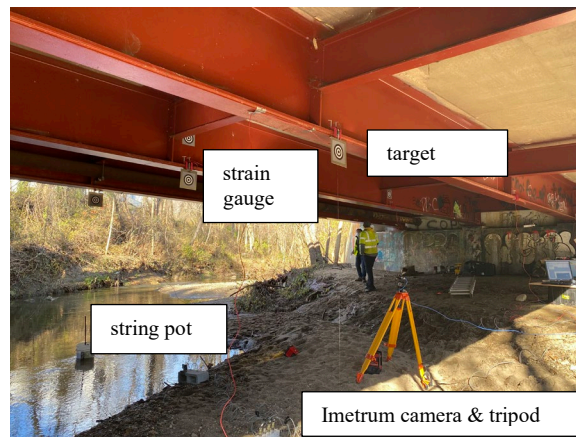


Figure 1. Overview of instrumentation placement under bridge.

During the static load tests, two additional cameras were used to collect sets of images (not videos) that were then converted into 3D point clouds via photogrammetry. Point clouds before and during static load testing were compared via computational geometric analysis to quantify the static 3D deformation fields. This process is illustrated in Figure 2. Captured images are first preprocessed to correct for lighting changes. The point cloud of the unloaded bridge (reference point cloud) and the point cloud for the statically loaded bridge (compared point cloud) were generated independently and then scaled and oriented to a global

reference frame using calibration targets attached to the structure (Figure 3). The two point clouds were then geometrically aligned and deformations were computed by measuring distances between points in each cloud.

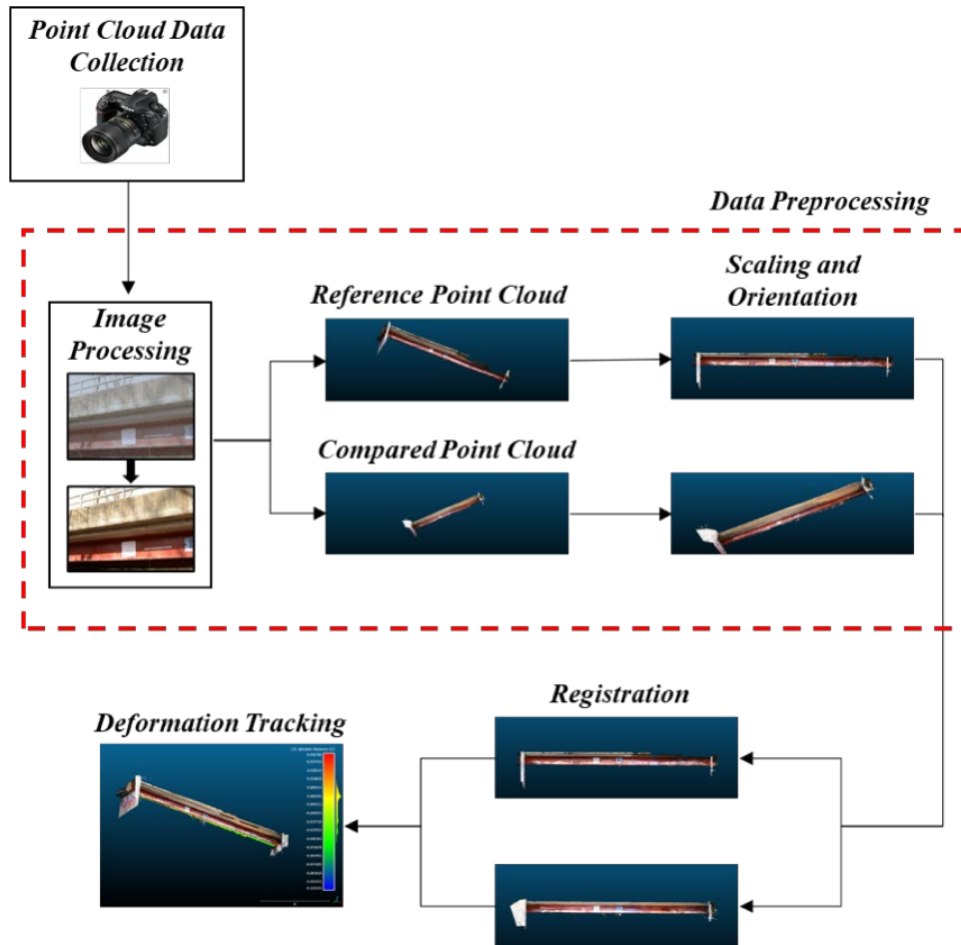


Figure 2. Overview of point cloud analysis methodology.

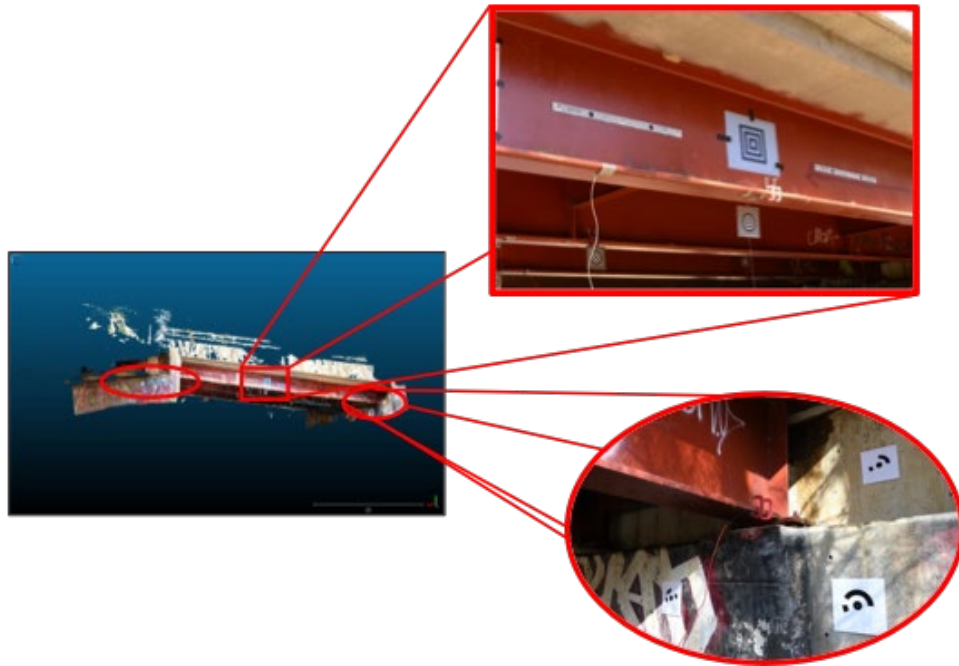


Figure 3. Placement of fiducial elements. The square zoom-in shows the non-coded target for orientation and the two bars for scaling. The oval zoom-in shows the targets used for registration of the two point clouds.

CASE STUDY: BRIDGE 1-911S

Description of Bridge

The first bridge tested is located in Smyrna, Delaware and was built in 2003 (referred to here as the 1-911S bridge). The single span, composite slab-on-steel girder bridge is simply supported, has a 19.8-m span length, and zero skew. This bridge was previously load tested in 2007 (Shenton III et al. 2007). The bridge consists of six W36x210 rolled I-beams spaced 2.74 m apart and a millimeter-thick reinforced concrete deck. The bays between girders contain four diaphragms located at the bridge bearings and at one-third and two-thirds along the span. The bridge maintains two southbound lanes and shoulders, all of which are 3.66 m wide. The bridge parapets run 864 mm (2.83 ft) high and are 406 mm (1.33 ft) wide. A section view of the bridge is shown in Figure 4.

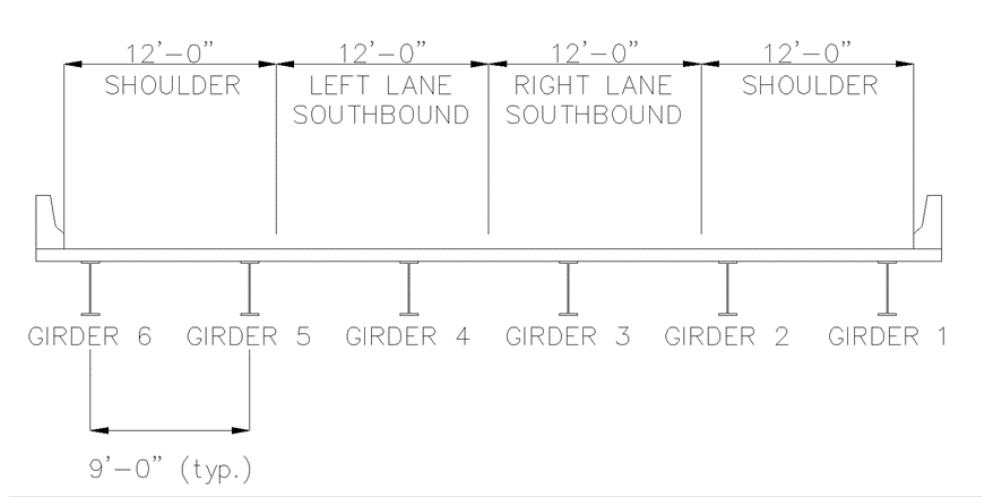


Figure 4. Bridge 1-911S cross-sectional view.

Instrumentation and Layout

The physical instrumentation, or sensor arrays, used for field testing are strain transducers and string potentiometers. The strain transducers and string potentiometers are mounted on the bridge and positioned at critical locations to directly measure deformations along the girders. For the 1-911S bridge tests, 18 strain transducers and six string potentiometers were attached to the bridge. Strain and displacement transducers were attached to the bottom flange at midspan of all six girders. Strain gauges were also placed one-foot offset from bridge bearings of girders three through six, and one quarter into the span of girders three and six. A plan view of the bridge's instrumentation plan is shown in Figure 5.

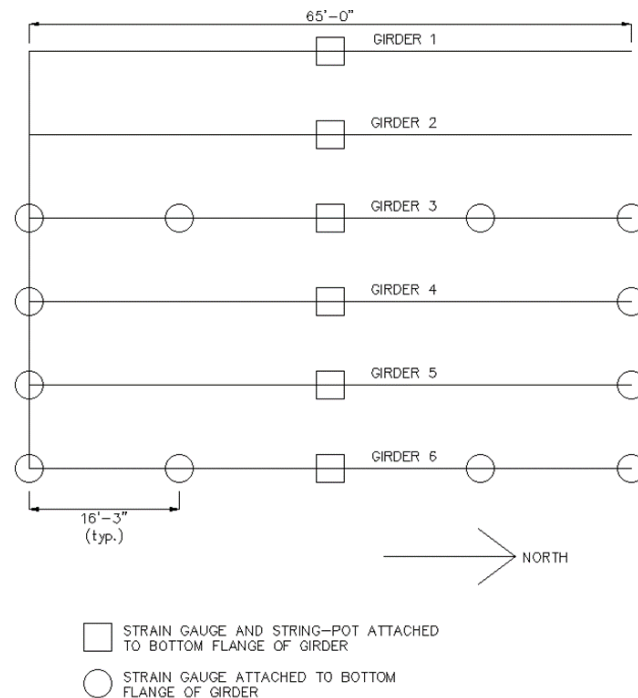


Figure 5. Bridge 1-911S load test instrumentation plan.

Test Procedure

The controlled load tests consisted of 10 pseudo-static tests and 3 static truck passes. The Delaware Department of Transportation (DelDOT) provided two 3-axle trucks, having gross vehicle weights of 61.32 and 64.58 kips, respectively. Each two-truck pass lane configuration was conducted twice, once where one truck was trailing the other, and another where the trucks passed over the bridge in tandem. The loading of the trucks was specified so that the two trucks passed over adjacent lanes or shoulder. Loading the bridge on both the right and left lanes and shoulders provided confirmation that the superstructure was acting symmetrically. Table 1 is the schedule of rolling passes that occurred during the 1-911S load tests; Figure 6 shows both trucks in tandem per Tests 1 and 3 noted in Table 1.

Table 1. 1-911S schedule of rolling passes for load tests.

Test	Brief Description	Truck 1 Position	Truck 2 Position	Notes
1	Single truck pass, 1 truck at a time (slowly)	Lane 1	Lane 2	Backup after Test
2	Side-by-side (tandem) pass, 2 trucks at a time (slowly)	Lane 1	Lane 2	Backup after Test
3	Single truck pass, 1 truck at a time (slowly)	Shoulder 1	Lane 1	Backup after Test
4	Side-by-side (tandem) pass, 2 trucks at a time (slowly)	Shoulder 1	Lane 1	Backup after Test



Figure 6. Single truck rolling pass (Test 1).

Two Imetrum cameras recorded videos for all quasi-static and dynamic truck passes. Two lenses, 12 mm (0.47 in) and 25 mm (0.98 in), were attached to the two Imetrum cameras. Imetrum Cam33, with a sensor diagonal of 6.3 mm (0.25 in), is a high-speed camera that records image files at a maximum frequency of 300 Hz in the ideal light and 50 Hz in sufficient lighting. Imetrum Cam37, with a sensor diagonal of 13.4 mm (0.53 in), can record image files at a maximum frequency of 50 Hz with sufficient lighting and has a wider field of view than Cam33. Attaching two separate lenses to Cam33 and Cam37 allowed for a comparison of different fields of view. A smaller lens allowed for a wider field of view, which can decrease the uncertainty of the known length used to calibrate measurements but creates uncertainty in the projection of the known length. Matte vinyl adhesive targets that are tracked within the Imetrum Video Gauge™ software were placed at midspan on the interior web of each girder. Videos were post-processed within the Imetrum system controller to determine displacement measurements of the bridge girders.

A challenge that arose during the 1-911S load tests was the inability to receive midspan displacement data of all six girders within the field of view at the same time. Only two Imetrum cameras were used during field testing, as getting a field of view that includes all girders would have compromised the working distance and increased uncertainty of the DIC displacement measurements. Depending on the lens used, the cameras were only able to track displacement measurements of one to three girders for each test based on the layout for this case study. Cam33, a camera with high-speed capabilities but a narrow field of view, was only able to track one or two girders depending on which lens was attached, while Cam37 with a wider field of view was able to track 2-3 girders depending on the attached lens.

The fields of view were limited based on the setup; however, careful planning to maximize the field of view and accuracy with the lens is extremely important. The discussion section will reveal how the global displacements for all six girders were stitched together to analyze the live-load distribution. This issue was alleviated for the 1-213 test by having one camera record midspan displacement data of all four girders within the field of view at the same time by attaching steel sheets with targets (Figure 7).



(a)



(b)

Figure 7. Imetrum target locations (a): 1-911S, (b): 1-213.

CASE STUDY: BRIDGE 1-213

Description of Bridge

The second bridge tested is located in Newark, Delaware and was built in 1989 (referred to here as the 1-213 bridge). This bridge is simply supported with a 21.34-m single-span bridge and zero skew. The composite girder bridge consists of four steel plate girders with web depth of 864 mm (2.83 ft), flange width of 311 mm (1.02 ft), spaced 2.59 m apart and reinforced concrete deck. Underneath the bottom flange along the inner 60% of each girder span are 19.1-mm (0.75-in) thick cover plates. The bays between girders contain five diaphragms located at the bridge bearings one-quarter, one-half, and three-quarters along the span. The bridge maintains a 7.92-m-wide roadway, which maintains northbound and southbound traffic and a 1.17-m-wide sidewalk (Figure 8).

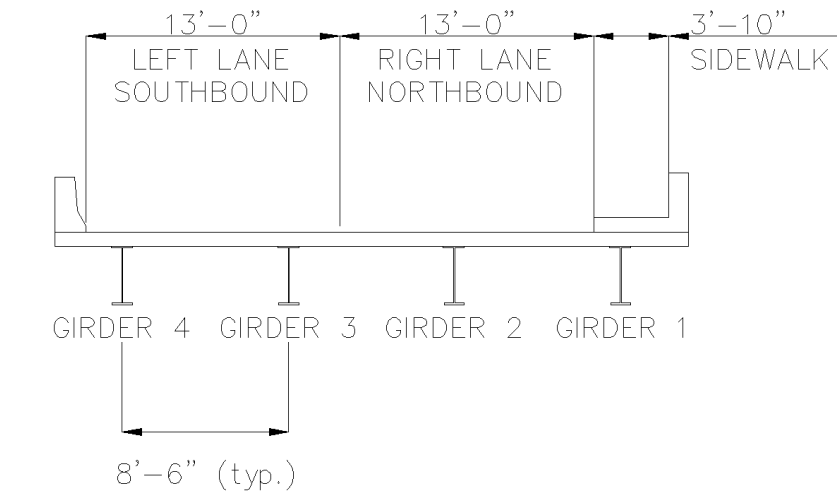


Figure 8. Bridge 1-213 cross-sectional view.

For the 1-213 bridge tests, 16 strain transducers and four string potentiometers were attached to the bridge. Strain and displacement transducers were attached to the bottom flange at midspan of all four girders. Strain gauges were also placed 1-ft offset from bridge bearings of each girder, and one quarter into the span of girders one and two. A plan view of the bridge's instrumentation plan is shown in Figure 9.

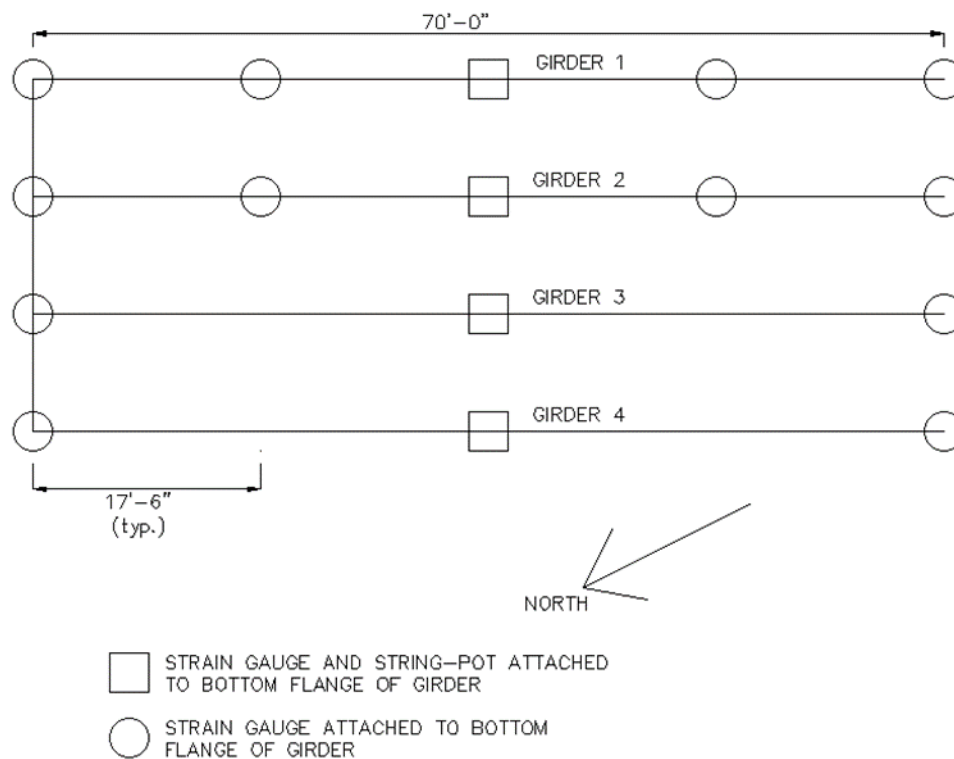


Figure 9. Bridge 1-213 load test instrumentation plan.

Test Procedure

The controlled load tests consisted of eight quasi-static tests, two posted-speed limit tests, and three static truck passes. For the pseudo-static tests, trucks rolled at a crawl speed 5-10 mph; for the posted-speed tests, trucks drove at 28-38 mph. The Delaware Department of Transportation provided two 3-axle trucks, having gross vehicle weights of 54.37 and 53.80 kips, respectively. Single and tandem truck passes occurred on both lanes. Table 2 is the schedule of rolling passes that occurred during the 1-213 load tests. For Tests 7 and 8, two trucks passed in the same lane, one trailing the other as closely as possible at a crawl speed.

Table 2. 1-213 schedule of rolling passes for load tests.

Test	Brief Description	Truck 1 Position	Truck 2 Position	Notes
1	Single truck pass, 1 truck at a time (slowly)	Left Lane	Right Lane	Backup after Test
2	Single truck pass, 1 truck at a time (slowly)	Left Lane	Right Lane	Backup after Test
3	Side-by-side (tandem) pass, 2 trucks at a time (slowly)	Left Lane	Right Lane	Backup after Test
4	Side-by-side (tandem) pass, 2 trucks at a time (slowly)	Left Lane	Right Lane	Backup after Test
5	Single truck pass, 1 truck at a time (posted speed)	Left Lane	Right Lane	Backup after Test
6	Single truck pass, 1 truck at a time (posted speed)	Left Lane	Right Lane	Backup after Test
7	Trailing trucks pass in same lane, one trailing the other as close as possible (slowly)	Right Lane	Right Lane	Backup after Test
8	Trailing trucks pass in same lane, one trailing the other as close as possible (slowly)	Right Lane	Right Lane	Backup after Test
9	Repeat Test #3; Side-by-side (tandem) pass, 2 trucks at a time (slowly)	Left Lane	Right Lane	Backup after Test

Just like in the previous case study, two cameras recorded videos for all quasi-static and dynamic truck passes. These videos were post-processed within the system controller, the critical hardware of the equipment, to determine displacement measurements of the bridge girders. Two lenses, 12 mm (about 0.47 in) and 25 mm (about 0.98 in), were attached to the two Imetrum cameras, which had 6.3 mm (about 0.25 in) and 13.4 mm (about 0.53 in) sensor diagonals, respectively. Cam33 remained in one location for every load pass while Cam37 was relocated once during the test. The 25mm (about 0.98 in) lens was attached to Cam33 and positioned 20 ft offset from the bridge to net the vertical deflection at midspan of all four girders. Cam37, with the 12-mm (about 0.47 in) lens, was placed in between the northeast bearings of girders 2 and 3 and then relocated underneath the midspan of girder 2, focused on the midspan of girders 3 and 4. Figure 10 is the field of view of Cam33 for the duration of the 1-213 load test.

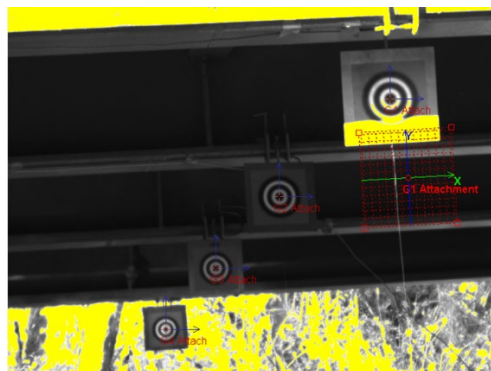


Figure 10. Imetrum Camera 33 field of view for DE 1-213 bridge load test.

CHAPTER 3

Findings

BRIDGE LIVE LOAD TEST RESULTS

Case Study: Bridge 1-911S

Single truck pass, 1 truck at a time (slowly) time histories

Test 1 is a quasi-static load test that consists of one truck passing over the right lane followed by a second truck passing over the left lane of the bridge roadway. Test 2 is a quasi-static load test that consists of two side-by-side trucks passing at once over the right and left lanes of the bridge roadway. Figures 11 through 14 are time-histories versus midspan displacement plots from Tests 1 and 2. Figures 15 and 16 are time-histories of the midspan bottom flange strain plots from Tests 1 and 2. Figure 11 shows the raw displacement time history measurement post-processed with Imetrum Video Gauge™ software for Test 1. Figure 12 shows the raw displacement time history measurement from the string potentiometers for Test 1. Figure 13 shows the post-processed Imetrum results for Test 2. Figure 14 shows the raw time history measurement from the string-potentiometers results for Test 2. Figure 15 shows the raw strain time history measurement from the BDI strain gauges processed with the BDI system for Test 1. Figure 16 shows the raw strain time history measurement from the BDI strain gauges processed with the BDI system for Test 2.

The string potentiometer measurements from the 1-911 load tests resulted in time-history plots that plateaued where maximum midspan displacements were expected. The reason for this error is not exactly known but is likely a fundamental issue with the measurement transducer. This issue was more noticeable for the 1-911 tests than for the 1-213 tests. There was noticeably stronger wind onsite the day of the 1-911S field test than on the day of the 1-213 test; the inclement weather may have impacted the string potentiometer measurements. Comparing the Imetrum midspan displacement from the 1-911S Tests 1 and 2 of individual girders matches what is expected based on superposition. The same is not the case for the midspan displacements read from the string pots. In Test 1, the deflection measurements for Girder 2 (G2) are nearly equal to the deflection of Girder 3 (G3). This could be an example of inexact data from measurement devices since it is expected that Girder 3 (G3) would have more deflection than Girder 2 (G2).

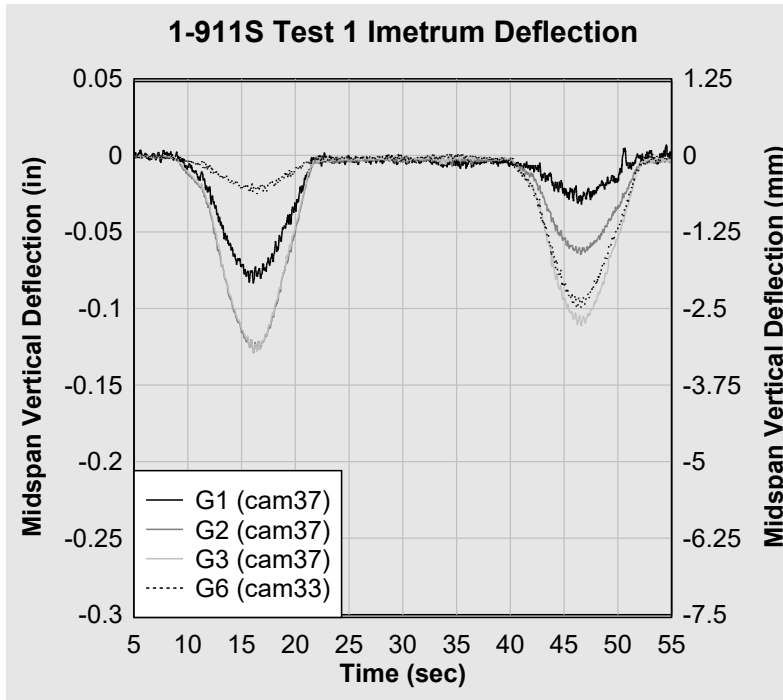


Figure 11. 1-911S Test 1 Imetrum midspan deflection.

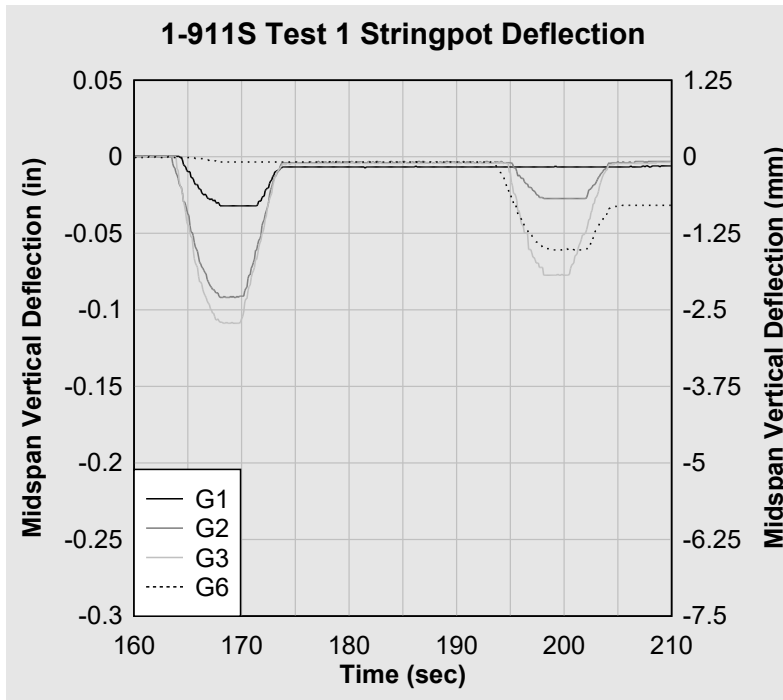


Figure 12. 1-911S Test 1 string pot midspan deflection.

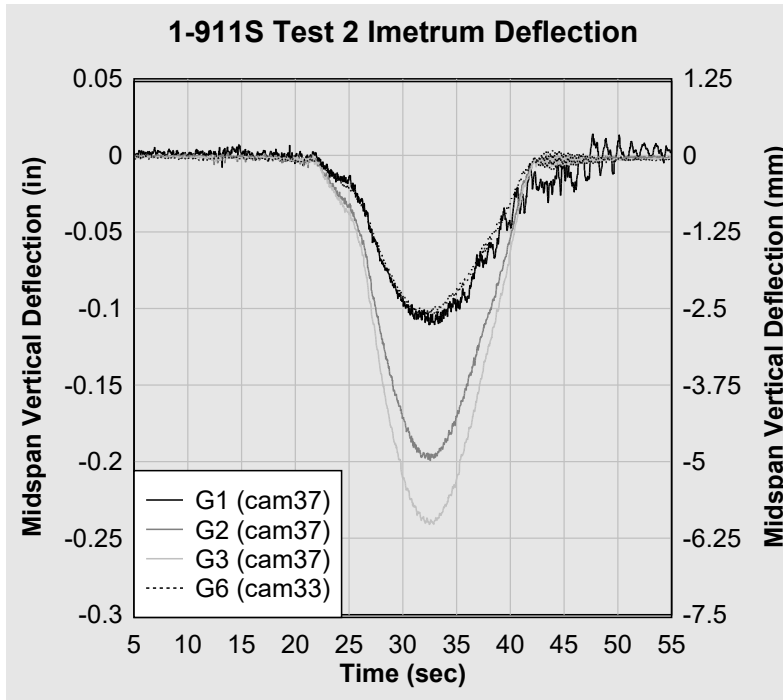


Figure 13. 1-911S Test 2 Imetrum midspan deflection.

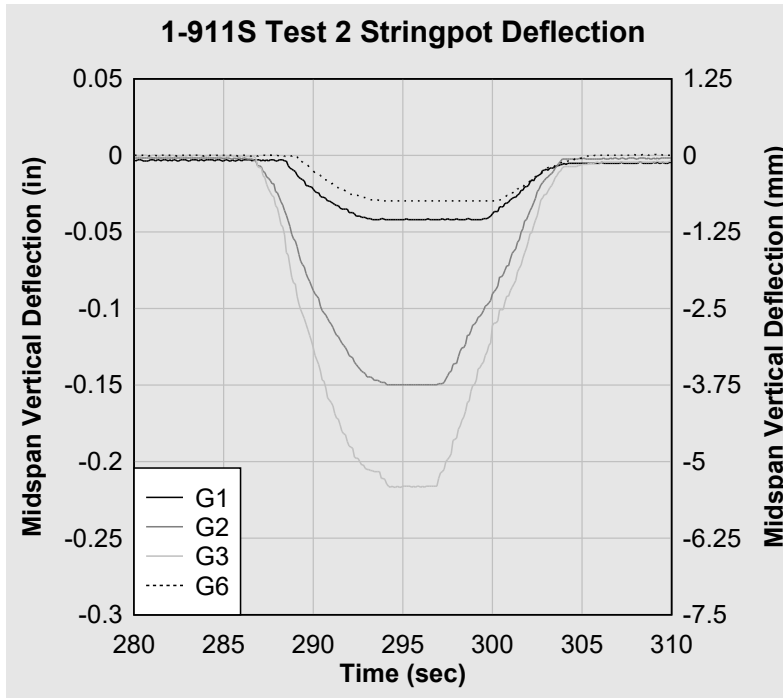


Figure 14. 1-911S Test 2 string pot midspan deflection.

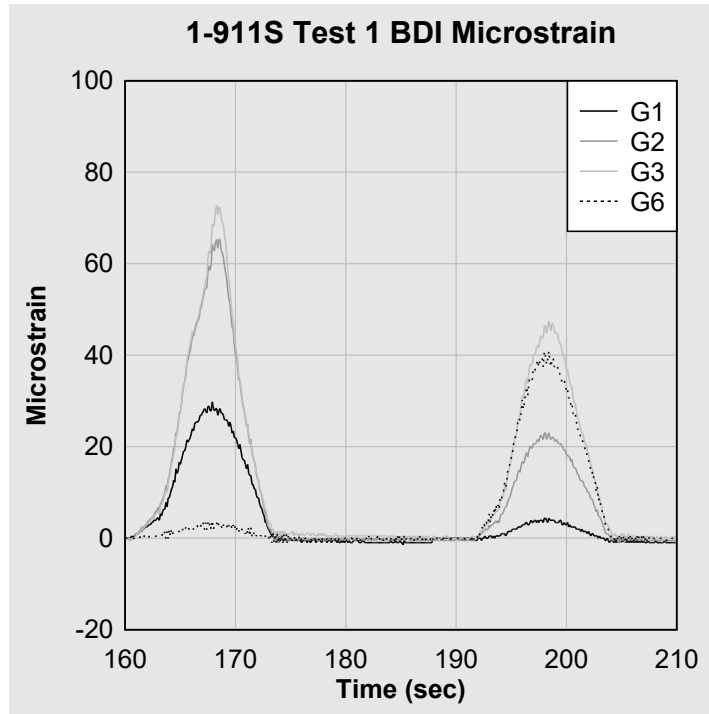


Figure 15. 1-911S Test 1 midspan bottom flange BDI microstrain.

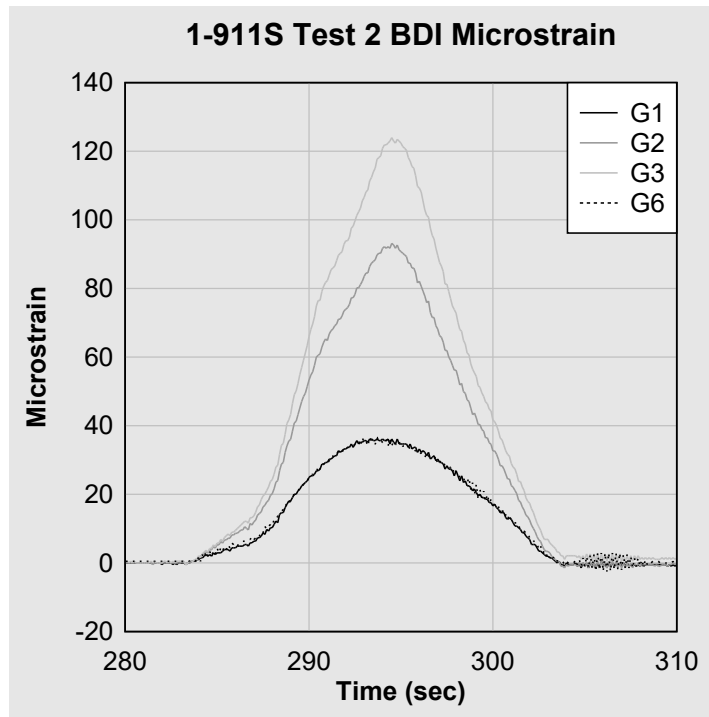


Figure 16. 1-911S Test 2 midspan bottom flange BDI microstrain.

Side-by-side (tandem) pass, 2 trucks at a time (slowly) time histories

Test 3 is a pseudo-static load test that consists of one truck passing over the right shoulder followed by a second truck passing over the right lane of the bridge roadway. Test 4 is a pseudo-static load test that consists of two side-by-side trucks passing at once over the right shoulder and right lane of the bridge roadway. Figures 17 through 20 are time-histories versus midspan displacement plots from Tests 3 and 4. Figures 21 and 22 are time-histories versus midspan bottom flange strain plots from Tests 1 and 2. Figure 17 shows the raw displacement time history measurement post-processed with Imetrum Video Gauge for Test 3. Figure 18 shows the raw displacement time history measurement from the string-potentiometers for Test 3. Figure 19 shows the post-processed Imetrum results for Test 4. Figure 20 shows the raw time history measurement from the string-potentiometers results for Test 4. Figure 21 shows the raw strain time history measurement from the BDI strain gauges processed with the BDI system for Test 3. Figure 22 shows the raw strain time history measurement from the BDI strain gauges processed with the BDI system for Test 4.

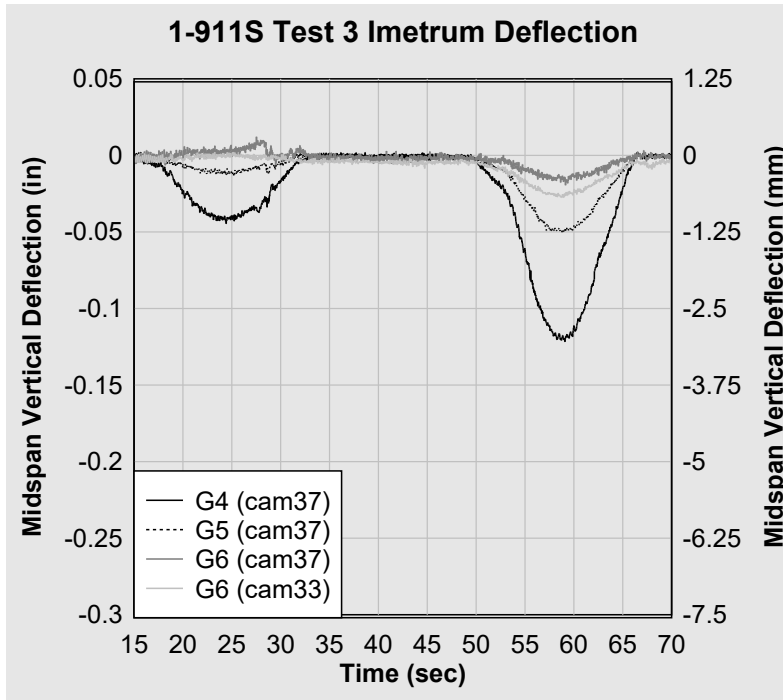


Figure 17. 1-911S Test 3 Imetrum midspan deflection.

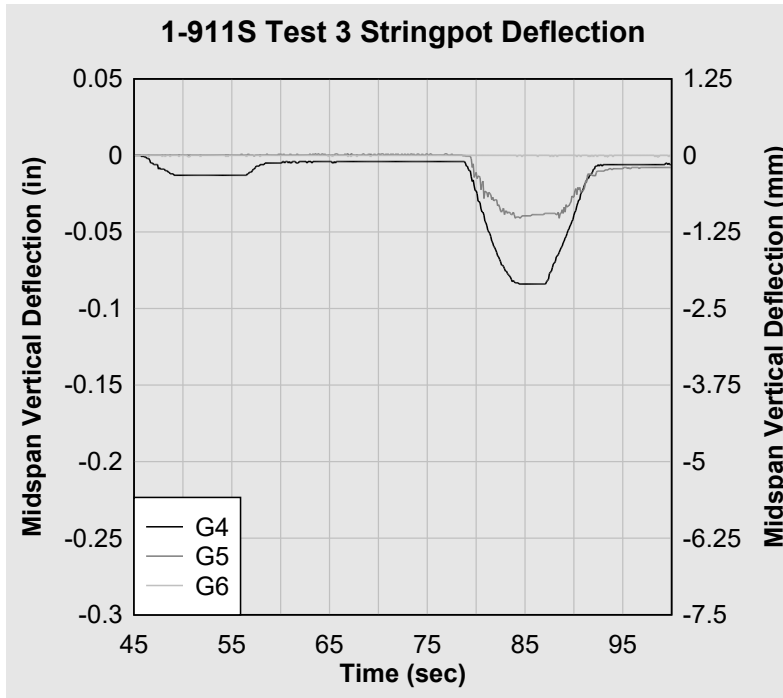


Figure 18. 1-911S Test 3 string pot midspan deflection.

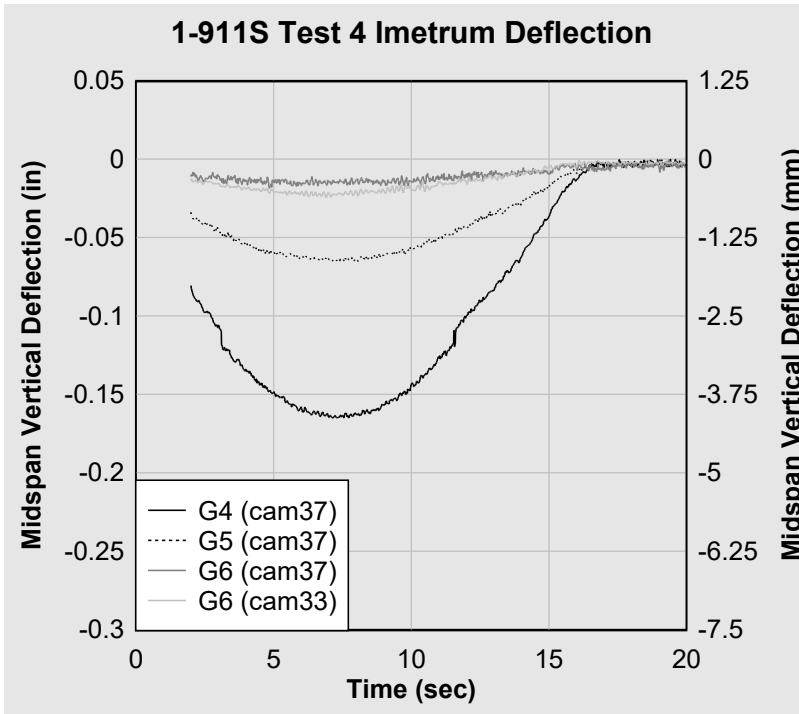


Figure 19. 1-911S Test 4 Imetrum midspan deflection.

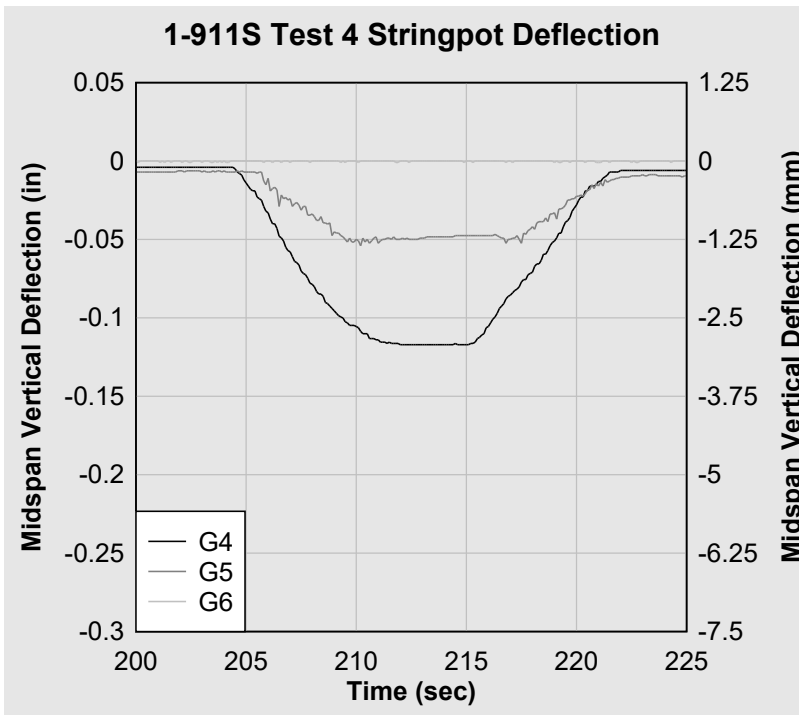


Figure 20. 1-911S Test 4 string pot midspan deflection.

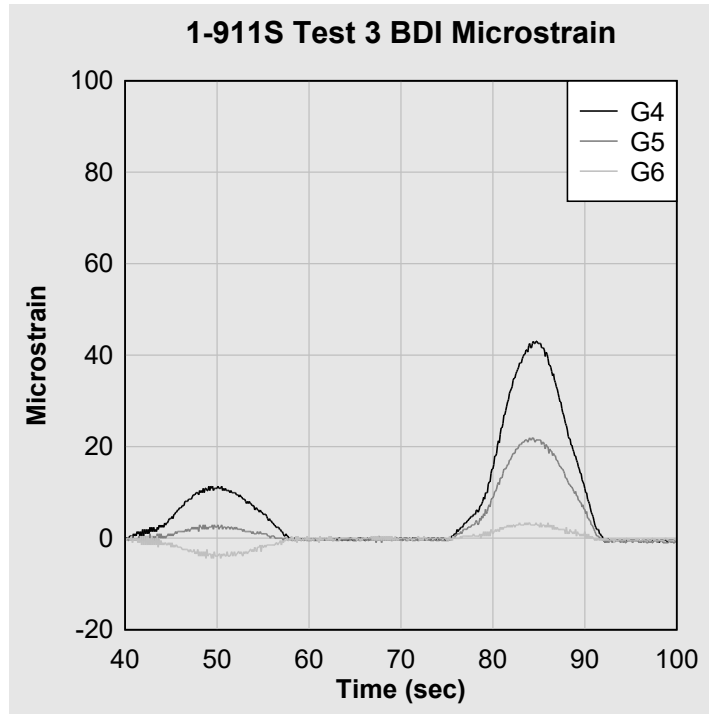


Figure 21. 1-911S Test 3 midspan bottom flange BDI microstrain.

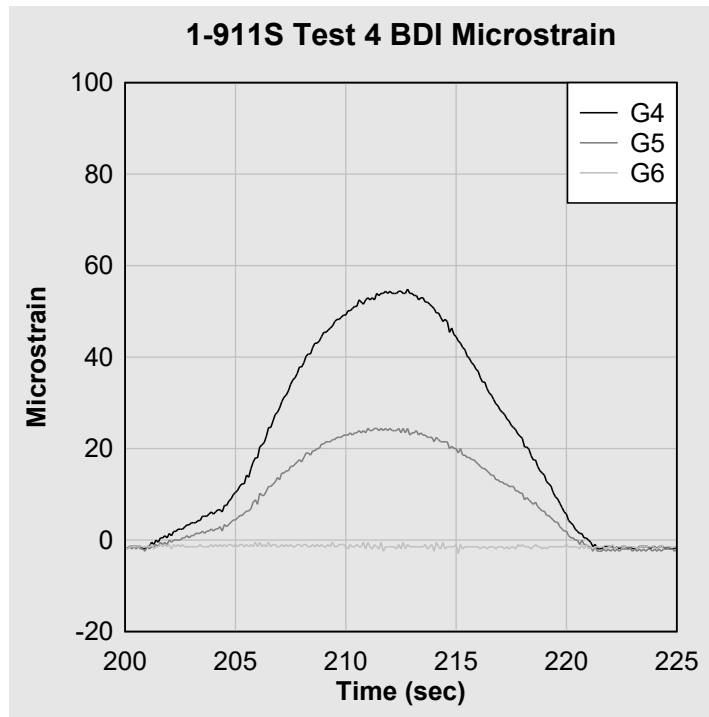


Figure 22. 1-911S Test 4 midspan bottom flange BDI microstrain.

Girder Midspan Displacement Comparison

Since each truck loading scenario occurred twice, once where one truck was trailing the other and another where the trucks passed through the bridge in tandem, superposition results of individual girders were easily evaluated. The results from the Imetrum system concurred with superposition measurements, while the string potentiometers did not. Time-histories of midspan displacements of selected girders for Tests 1 through 4 were captured. The farthest web target from Cam37 field of view in Tests 1 and 2 was the one attached to G1. For Tests 1 and 2 the G1 Cam37 target resulted in the noisiest data.

The farthest web target from Cam37 field of view in Tests 3 and 4 was the one attached to Girder 6 (G6). For Tests 3 and 4, the G6 Cam37 target resulted in the noisiest data. The G6 Cam33 target presents a nice comparison of data from a camera focused on a girder compared to the G6 Cam37, which is in the background of its video file. For Truck Pass 4, the Imetrum system did not start running until after the two trucks started passing over the bridge. By setting the average of the measured displacements after the trucks passed over the bridge over each data array as zero, vertical displacements show reasonable displacement readings. Even when data collection is started in the middle of a truck pass/loading scenario, the video file can measure accurate displacement readings. Tables 3 shows a comparison of Imetrum VideoGauge™ and string-potentiometer displacement measurements from Test 1 (trailing truck passes in lanes 1 and 2) and Test 2 (tandem truck pass in lanes 1 and 2). The Imetrum results match based on superposition better than the results from the string-potentiometer.

Table 3. 1-911S girder midspan displacement comparison.

Aspect	Girder 1		Girder 2		Girder 3		Girder 6	
	Ime	STP	Ime	STP	Ime	STP	Ime	STP
Lane 1 (mm)	2.1	0.8	3.3	2.2	3.2	2.8	0.5	0.3
Lane 2 (mm)	0.8	0.2	1.6	0.6	2.8	1.9	2.5	1.5
Tandem (mm)	2.8	1.0	5.0	3.8	6.1	5.5	2.6	0.8

Note: Ime = Imetrum; STP = String pot.

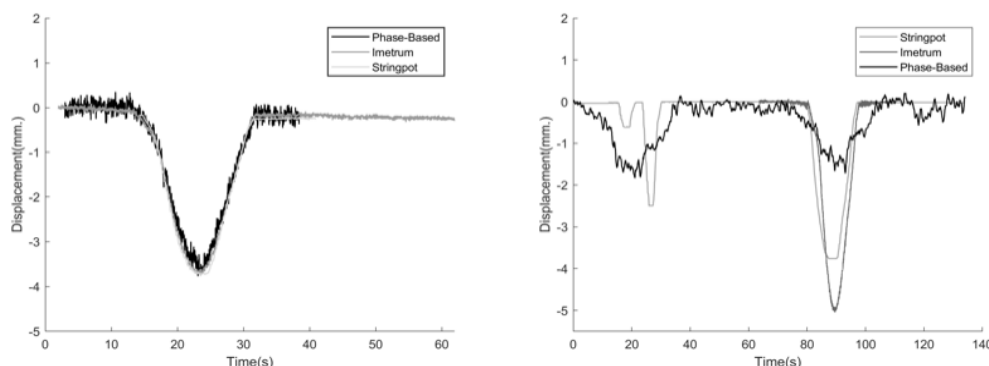


Figure 23. Comparison of measurement methods: (a) strong correlation of results for fascia girder nearest to the phase-based camera and (b) inaccurate results for the phase-based approach, for girder farther away from camera.

Lateral Live Load Distribution

The lateral distribution of live load from the field test was assessed using both strain transducers located at the midspan of each girder and the Imetrum system, which captured the vertical deflections at midspan using video-based measurements. The displacement data from the string potentiometers and Imetrum system midspan displacement measurements were compared. For all load passes, the Imetrum system measured larger displacement measurements than the string potentiometers. The displacement time-history plots of the string potentiometers plateaued in value when the peak displacement measurements were expected, while the Imetrum system measurements had a smooth peak. Since each truck loading scenario occurred twice, once where one truck was trailing the other and another where the trucks passed through the bridge in tandem, superposition results of individual girders were easily evaluated and evident with the tandem load results shown in Figures 13 through 15; the maximum displacement captured by the Imetrum system was slightly less than 6.35 mm (0.25 in). The results from the Imetrum system concurred with superposition measurements while the string potentiometers did not.

Live-load distribution factors for each truck load per beam were calculated using the midspan displacements measurement from the strain transducers placed on the bottom flange of each girder at midspan and from the Imetrum system. Tables 4 and 5 show the results from the strain and Imetrum displacement measurements along with the LLDFs computed per girder for the heavier loaded truck (Truck 1) and tandem trucks (Trucks 1 and 2).

Table 4. Live-load distribution factors (LLDFs) for lane 1 truck pass.

Girder	1	2	3	4	5	6
Strain ($\mu\epsilon$)	28	65	73	41	21	3
Displacement (mm)	2.1	3.3	3.3	2.8	1.6	0.8
LLDF $\mu\epsilon$	0.12	0.28	0.31	0.18	0.09	0.01
LLDF Δ	0.15	0.24	0.24	0.20	0.12	0.06

Table 5. Live-load distribution factors (LLDFs) for lanes 1 and 2 tandem truck pass.

Girder	1	2	3	4	5	6
Strain ($\mu\epsilon$)	36	93	123	121	81	34
Displacement (mm)	2.8	5.1	6.1	6.1	5.1	2.8
LLDF $\mu\epsilon$	0.15	0.38	0.51	0.50	0.33	0.14
LLDF Δ	0.2	0.36	0.44	0.44	0.36	0.20

SAP2000 is utilized to create a bridge model for the finite element analyses. Hand calculations for the composite W36x210 rolled beam were performed and compared to the SAP2000 results. LLDFs were computed using conventional methods per the *AASHTO LRFD Bridge Design Specifications (2020)*, Lever Rule Grillage Model, and Finite Element Model data for moment, deflection, and shear to evaluate the lateral distribution due to live load. The lateral distribution live-load distribution factor for truck load per beam (LLDF_{truck}) was calculated and compared. The bridge grillage model in SAP2000 consists of frame sections for the non-composite W36x210 rolled beam and the bridge deck were defined separately and connected by fully rigid linear link elements every 305 mm (1 ft) along the beam's 19.8 m (65 ft) span.

Non-rigid link elements were used to link girder decks to their nearest girder, where the vertical displacement and in-plane moments were analyzed and compared to the data from the load test.

Once the bridge model was generated, it was used to calibrate the model using the results from the load test. Based on the strain measurements from strain gauges placed near the bridge bearings, it was discovered that the bearings provided significant restraint. A single girder line analysis was performed using a composite beam in SAP2000. Based on the vision-based measurement data from the Imetrum system, the lateral distribution of girder deflection from a truck passing over Lane 1 one girder received 25% of the superstructure’s deflection. Applying 25% of the three axles from the DelDOT Truck 2735 load in SAP2000 resulted in displacements and strains within 5% difference of what was measured during the load test shown in Tables 2 and 3. Initially, SAP2000 estimated the summation of midspan girder displacement, $\Delta=7.4$ mm (0.29 in) whereas the measured displacement from the load test at the midspan girder was 13.97 mm (0.55 in). To adjust the estimated displacement from the grillage model, frame properties stiffness modification factors were applied. Having a steel girder and concrete deck stiffness modification factor of 0.72 resulted in a displacement of 3.4 mm (0.134 in) in Girder 3, 26% of the girder system’s lateral distribution of live load deflection.

Tables 6 and 7 show LLDFs for deflection and moment based on different methods. A single girder line analysis using BRASS-GIRDER was also performed for a DelDOT 2735 truck and resulted in a displacement of 3.86 mm (0.15 in) compared to 3.3 mm (0.13 in) of displacement obtained from the vision-based measurement. Tables 6 and 7 show a comparison of the LLDF obtained from BRASS, load testing (measured field data), finite element modeling using SAP2000 for 1-lane (single lane) and multiple lanes (M-lanes), and AASHTO LRFD (2020) approximates for the distribution factors (mg) for moment, assuming non-composite beam behavior.

Table 6. Comparison of LLDFs for deflection computed using various methods.

Deflection					
BRASS (mg)		Field Test (mg)		SAP2000 (mg)	
1-lane	M-lanes	1-lane	M-lanes	1-lane	M-lanes
0.20	0.43	0.30	0.44	0.39	0.49

Table 7. Comparison of LLDFs for moment computed using various methods.

Moment							
AASHTO (mg)		BRASS (mg)		Field Test (mg)		SAP (mg)	
1-lane	M-lanes	1-lane	M-lanes	1-lane	M-lanes	1-lane	M-lanes
0.48	0.67	0.52	0.72	0.38	0.51	0.41	0.52

Case Study: Bridge 1-213

Single truck pass, 1 truck at a time (slowly) time histories

Tests 1 and 2 are duplicate quasi-static load tests, which consist of one truck passing over the left lane followed by a second truck passing over the right lane. Figures 24 through 27 are time-histories versus midspan displacement plots from Tests 1 and 2. Figures 28 and 29 are time-histories versus midspan bottom flange strain plots from Tests 1 and 2.

Figure 24 shows the raw displacement time history measurement post-processed with Imetrum Video Gauge for Test 1. Figure 25 shows the raw displacement time history measurement from the string-potentiometers for Test 1. Figure 26 shows the post-processed Imetrum results for Test 2. Figure 27 shows the raw time history measurement from the string-potentiometers results for Test 2. The Imetrum and string-potentiometer data resulted in similar midspan displacement readings for the first of two truck passes. The second of two truck passes of these pseudo-static loads resulted in max displacement that had a larger differential than the first of the trailing truck passes. The string-potentiometer's difficulty rebounding during trailing truck passes is an example of error that can occur with physical instrumentation. This same error cannot occur from post-processing video recordings if the Imetrum cameras remain stationary for the duration of each load pass individual video file can be postprocessed and recalibrated. Figure 23 shows the raw strain time history measurement from the BDI strain gauges processed with the BDI system for Test 1. Figure 23 shows the raw strain time history measurement from the BDI strain gauges processed with the BDI system for Test 2.

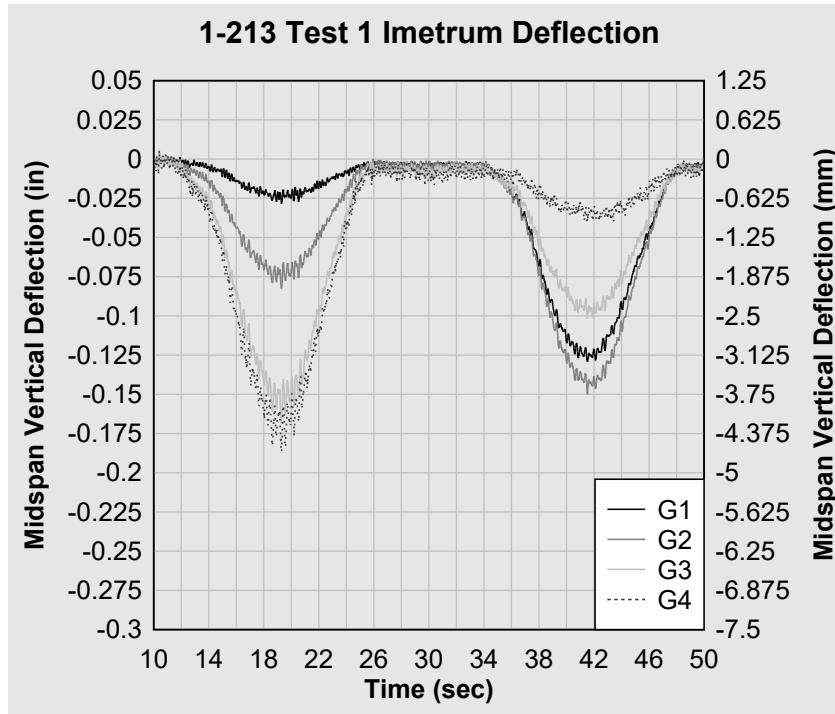


Figure 24. 1-213 Test 1 Imetrum midspan deflection.

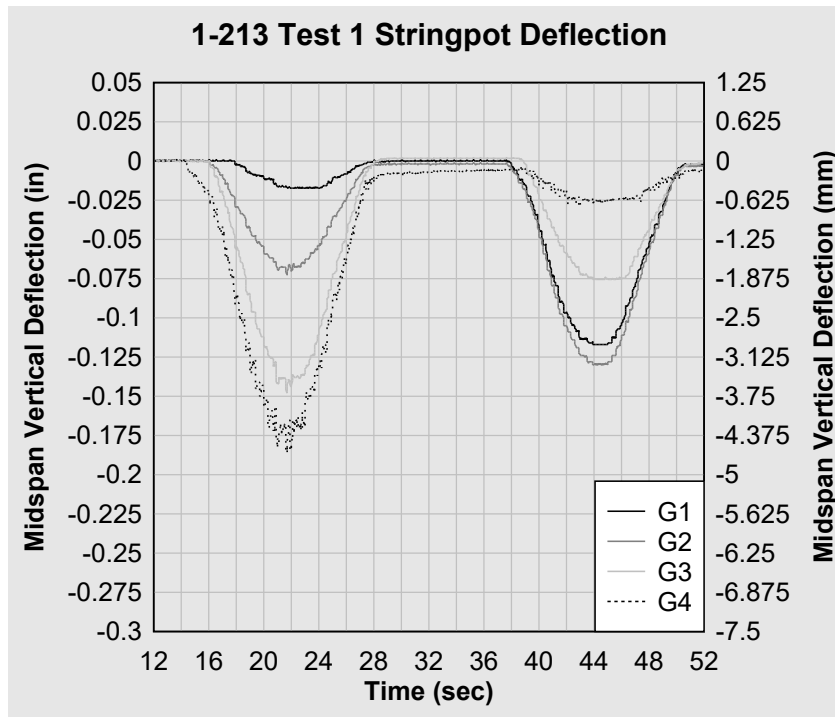


Figure 25. 1-213 Test 1 string pot midspan deflection.

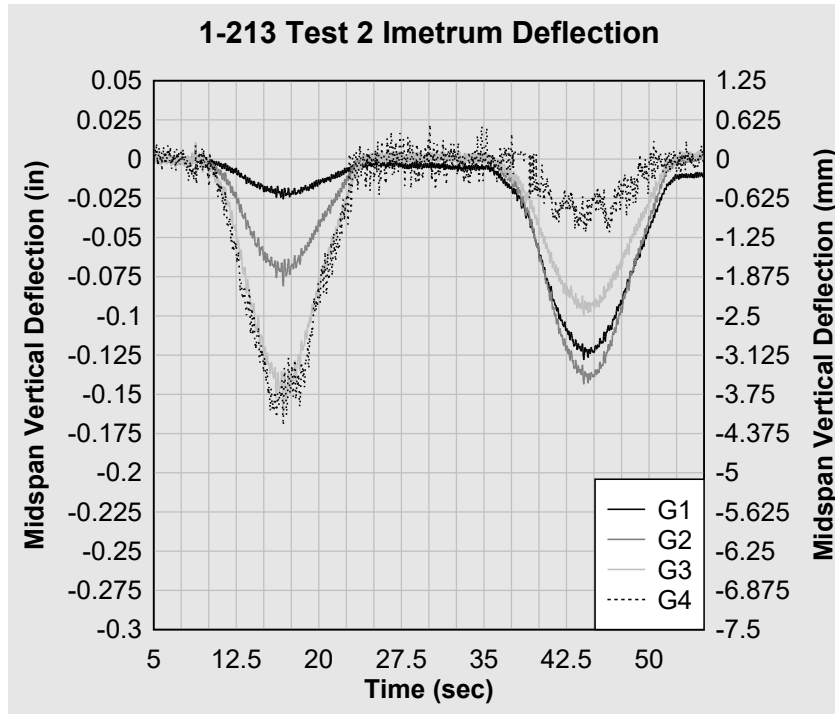


Figure 26. 1-213 Test 2 Imetrum midspan deflection.

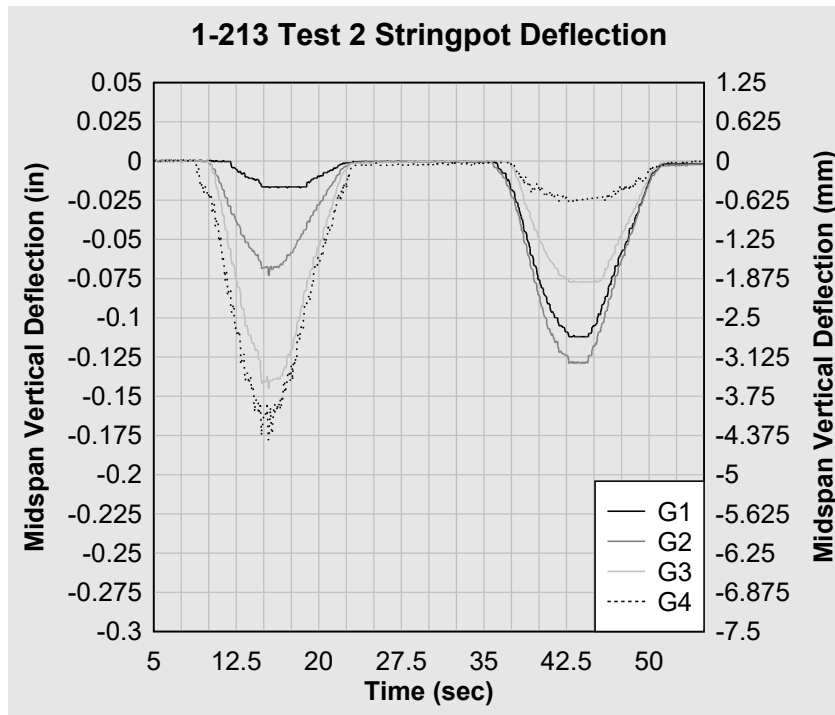


Figure 27. 1-213 Test 2 string pot midspan deflection.

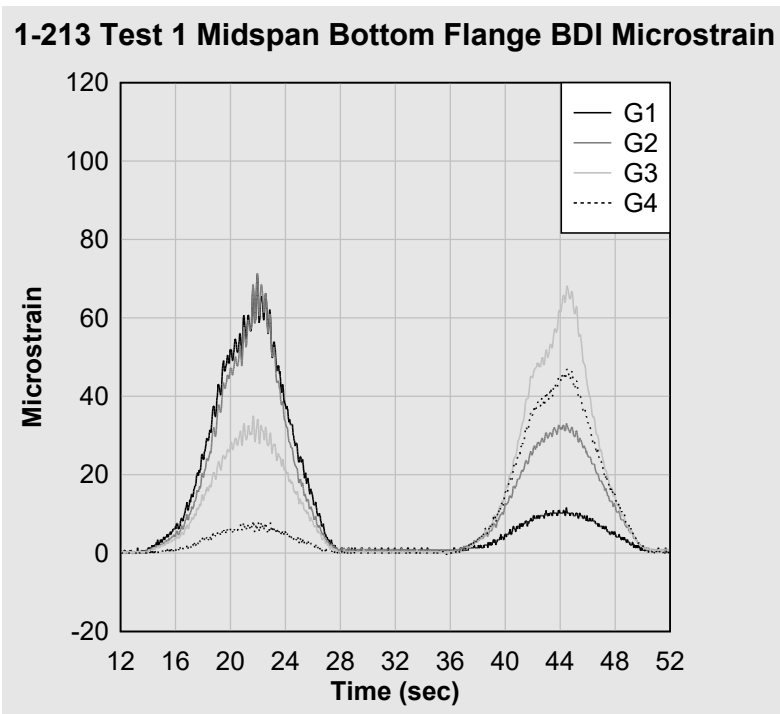


Figure 28. 1-213 Test 1 midspan bottom flange BDI microstrain.

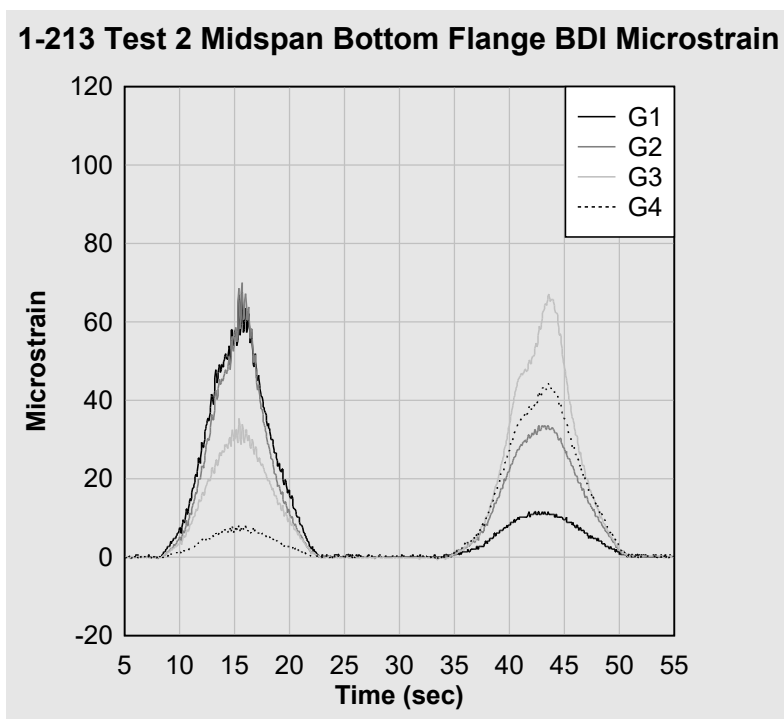


Figure 29. 1-213 Test 2 midspan bottom flange BDI microstrain.

Side-by-side (tandem) pass, 2 trucks at a time (slowly) time histories

Tests 3, 4, and 9 are duplicate pseudo-static load tests that consist of two side-by-side trucks passing at once over the left and right lanes of the bridge roadway. Figures 30 through 35 are time-histories versus midspan displacement plots from Tests 3, 4, and 9. Figures 36 through 38 are time-histories versus midspan bottom flange strain plots from Tests 3, 4, and 9.

Figure 30 shows the raw displacement time history measurement post-processed with Imetrum Video Gauge for Test 3. Figure 31 shows the raw displacement time history measurement from the string-potentiometers for Test 3. Figure 32 shows the post-processed Imetrum results for Test 4. Figure 33 shows the raw time history measurement from the string-potentiometer results for Test 4. Figure 34 shows the post-processed Imetrum results for Test 9. Figure 35 shows the raw time history measurement from the string-potentiometers result for Test 9.

Figure 36 shows the raw strain time history measurement from the BDI strain gauges processed with the BDI system for Test 3. Figure 37 shows the raw strain time history measurement from the BDI strain gauges processed with the BDI system for Test 4. Figure 38 shows the raw strain time history measurement from the BDI strain gauges processed with the BDI system for Test 9.

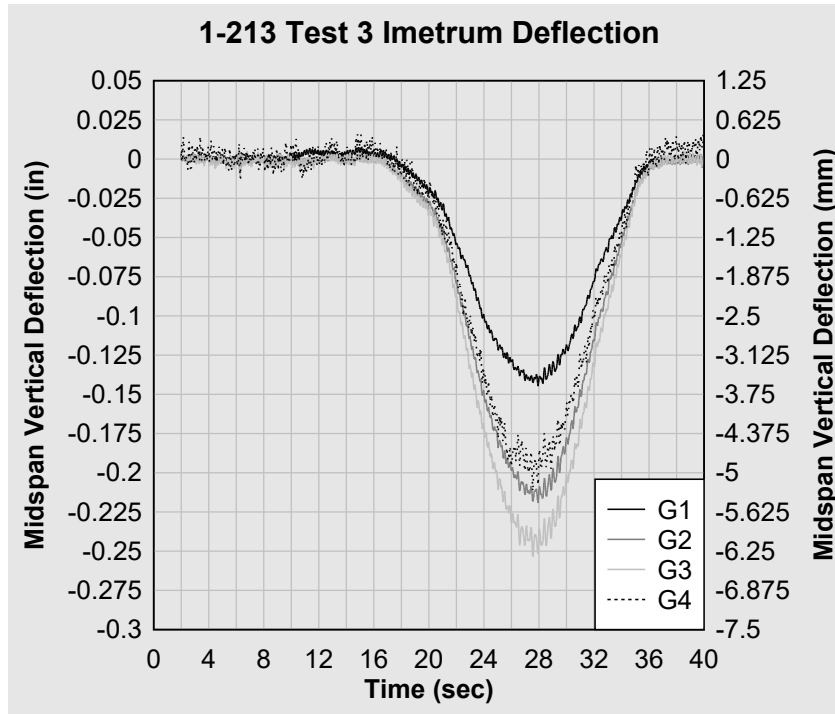


Figure 30. 1-213 Test 3 Imetrum midspan deflection.

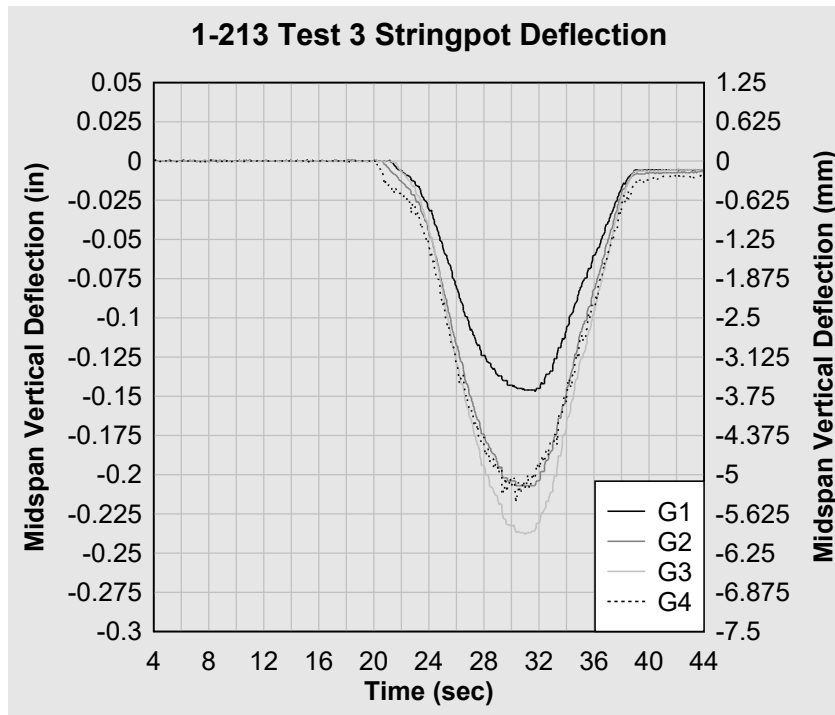


Figure 31. 1-213 Test 3 string pot midspan deflection.

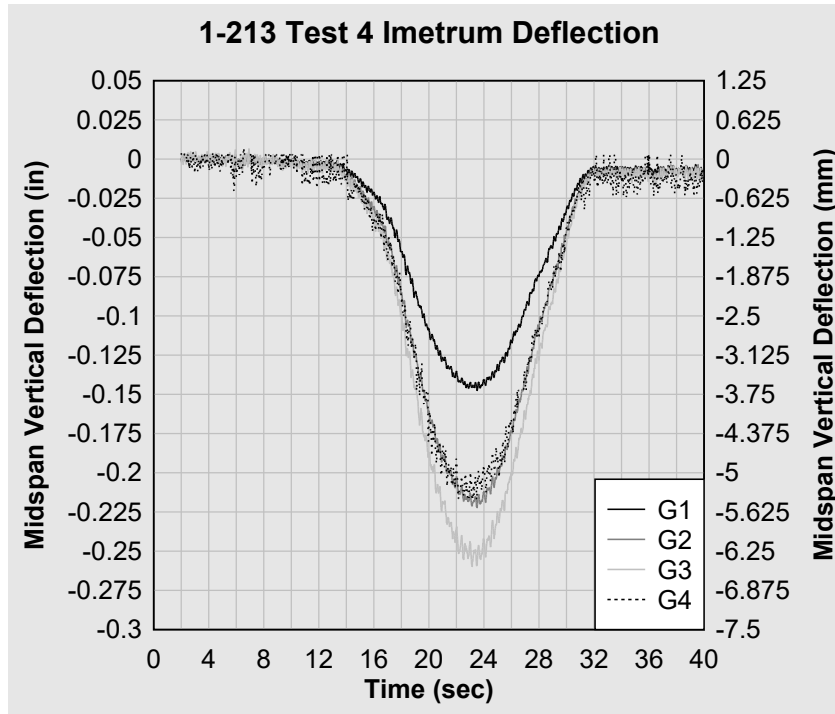


Figure 32. 1-213 Test 4 Imetrum midspan deflection.

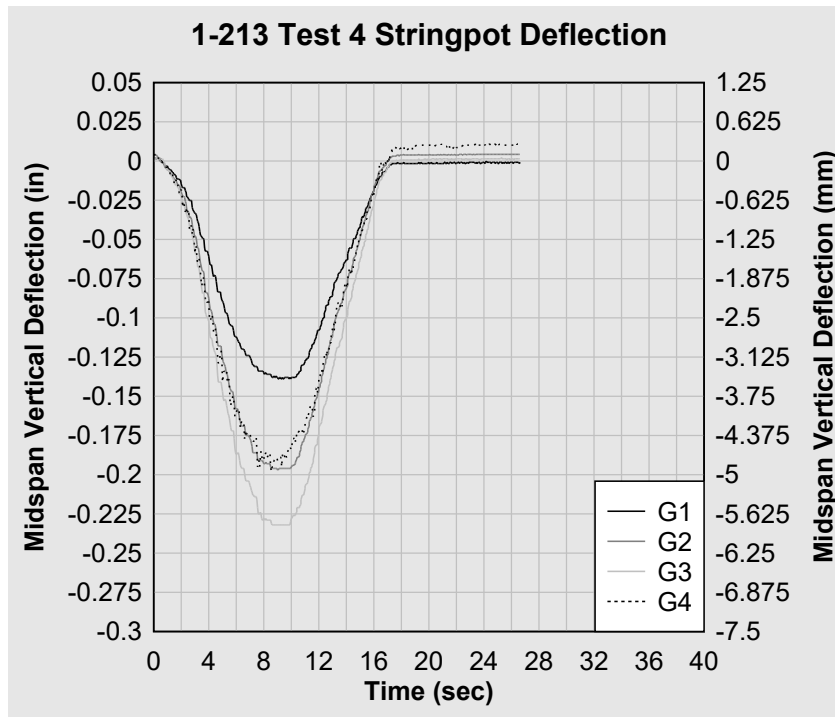


Figure 33. 1-213 Test 4 string pot midspan deflection.

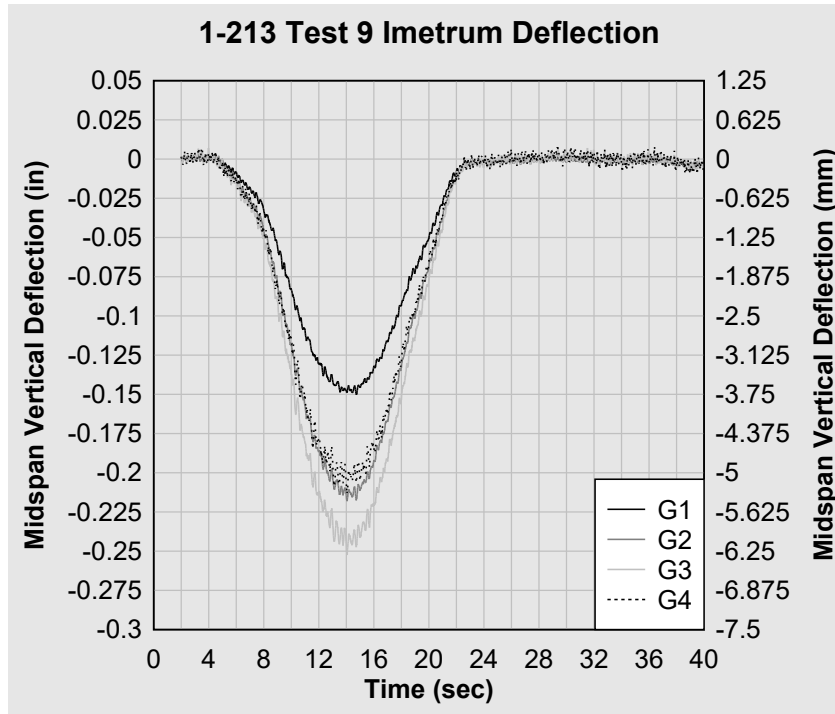


Figure 34. 1-213 Test 9 Imetrum midspan deflection.

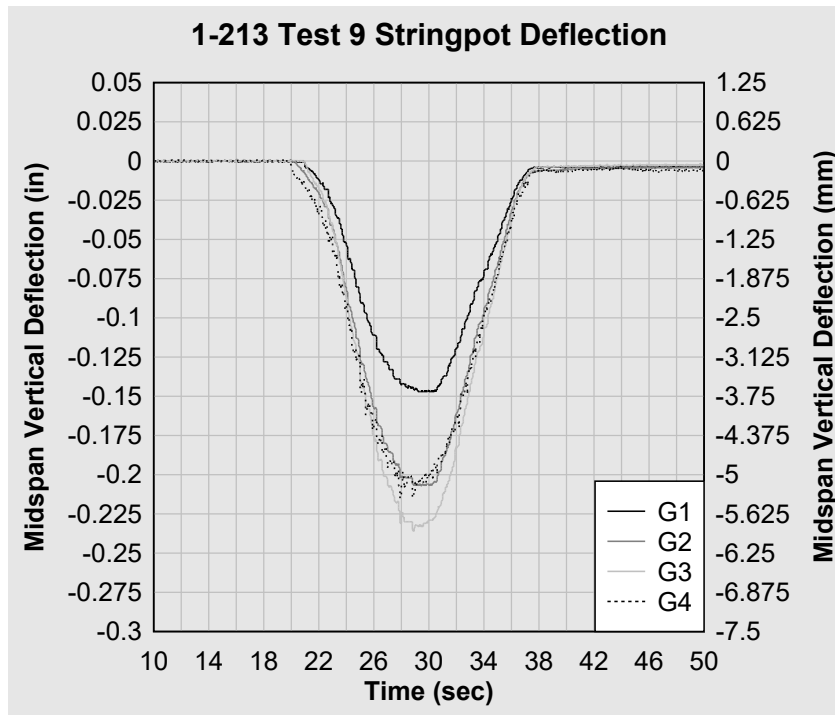


Figure 35. 1-213 Test 9 string pot midspan deflection.

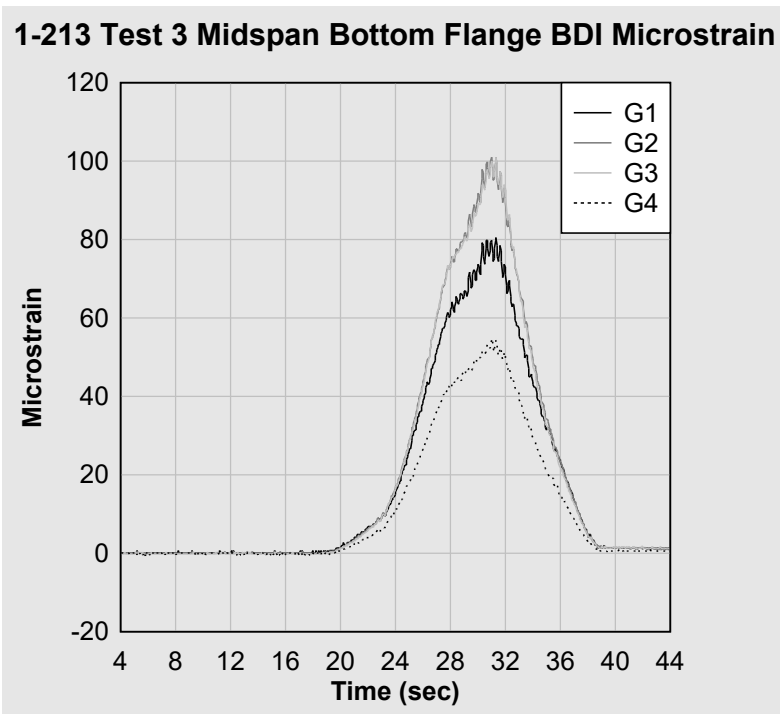


Figure 36. 1-213 Test 3 midspan bottom flange BDI microstrain.

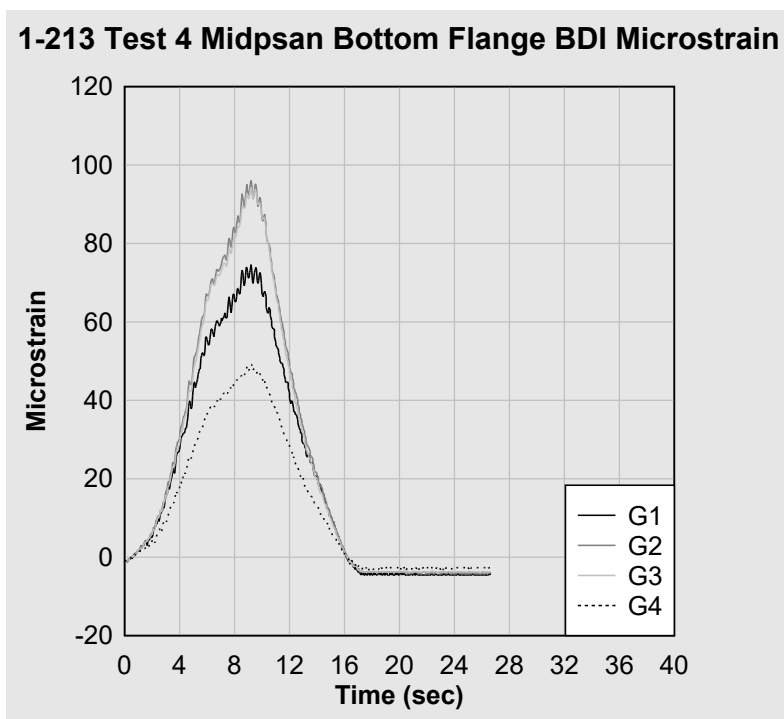


Figure 37. 1-213 Test 4 midspan bottom flange BDI microstrain.

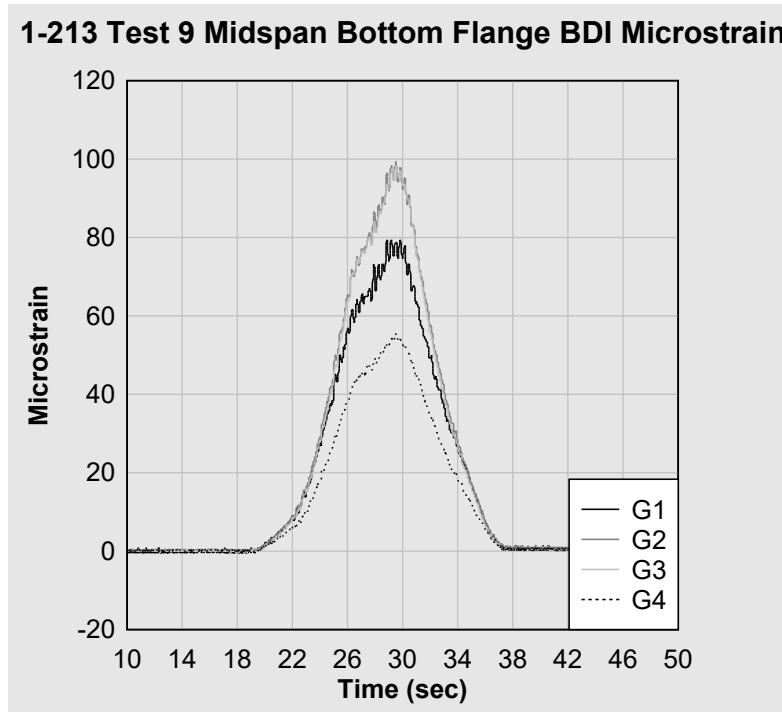


Figure 38. 1-213 Test 9 midspan bottom flange BDI microstrain.

Single truck pass, 1 truck at a time (posted speed) time histories

Tests 5 and 6 are duplicate posted speed limit load tests that consist of one truck passing over the left lane followed by a second truck passing over the right lane of the bridge roadway. Figures 39 through 46 are time-histories versus midspan displacement plots from individual truck passes of Tests 5 and 6. Figures 47 through 50 are time-history versus midspan bottom flange strain plots from individual truck passes of Tests 5 and 6. Figure 39 shows the raw displacement time history measurement post-processed with Imetrum VideoGauge™ software for Test 5 truck pass 1. Figure 40 shows the raw displacement time history measurement from the string-potentiometers processed with the BDI system for Test 5 truck pass 1. Figure 41 shows the post-processed Imetrum results for Test 5 truck pass 2. Figure 42 shows the raw time history measurement from the string-potentiometers results for Test 5 truck pass 2. Figure 43 shows the post-processed Imetrum results for Test 6 truck pass 1. Figure 44 shows the raw time history measurement from the string-potentiometer results for Test 6 truck pass 1. Figure 45 shows the post-processed Imetrum results for Test 6 truck pass 2. Figure 46 shows the raw time history measurement from the string-potentiometer results for Test 6 truck pass 2. Imetrum and string-potentiometer resulted in similar midspan displacement readings for the first of two truck passes. The second of two truck passes of these pseudo-static loads resulted in max displacement that had a larger differential than the first of the trailing truck passes. The discrepancy in deflection readings for the second of two trailing truck passes were similar to the discrepancies in results from Tests 1 and 2. Figure 47 shows the raw strain time history measurement from the BDI strain gauges for Test 5 truck pass 1. Figure 48 shows the raw strain time history measurement from the BDI strain gauges processed with the BDI system for Test 5 truck pass 2. Figure 49 shows the raw strain time history measurement from the BDI strain gauges processed with the BDI system for Test 6 truck pass 1. Figure 50 shows the raw strain time history measurement from the BDI strain gauges processed with the BDI system for Test 6 truck pass 2.

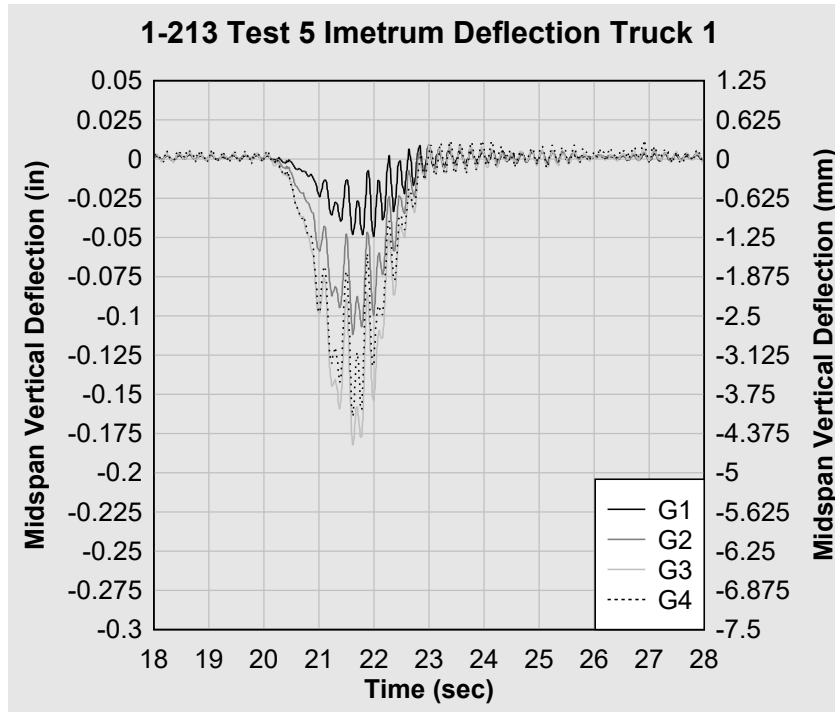


Figure 39. 1-213 Test 5 Imetrum truck 1 midspan deflection.

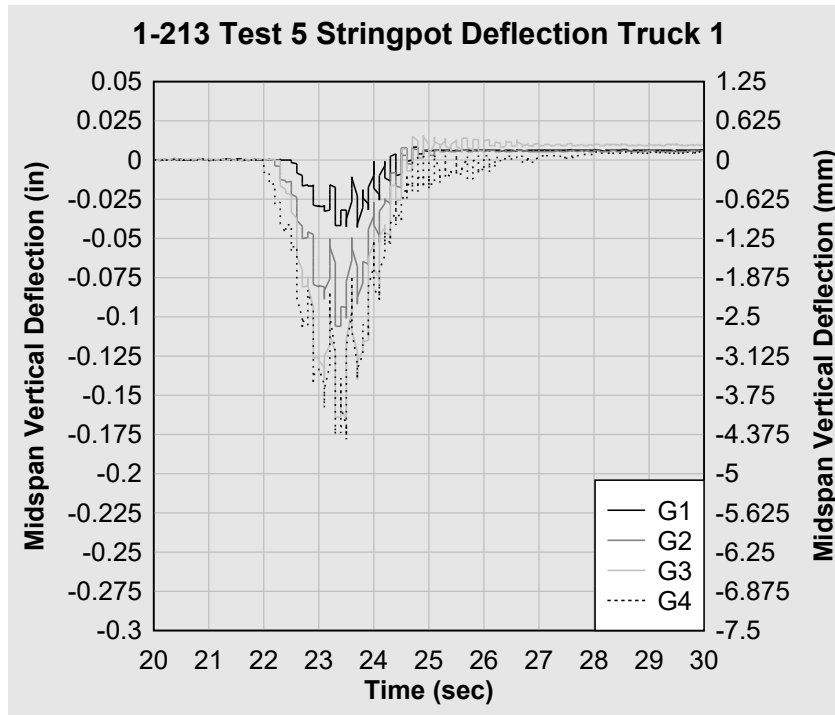


Figure 40. 1-213 Test 5 string pot truck 1 midspan deflection.

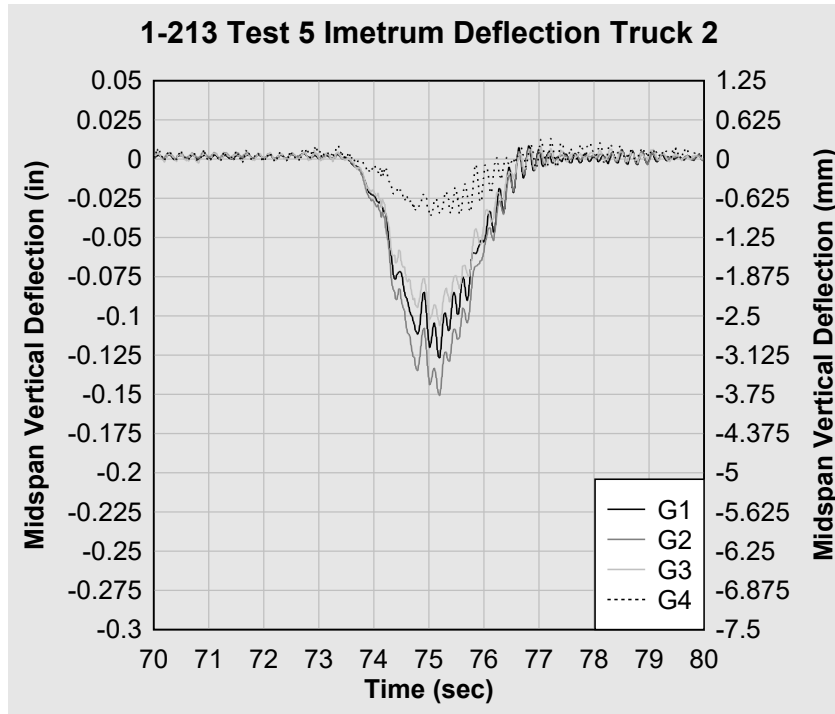


Figure 41. 1-213 Test 5 Imetrum truck 2 midspan deflection.

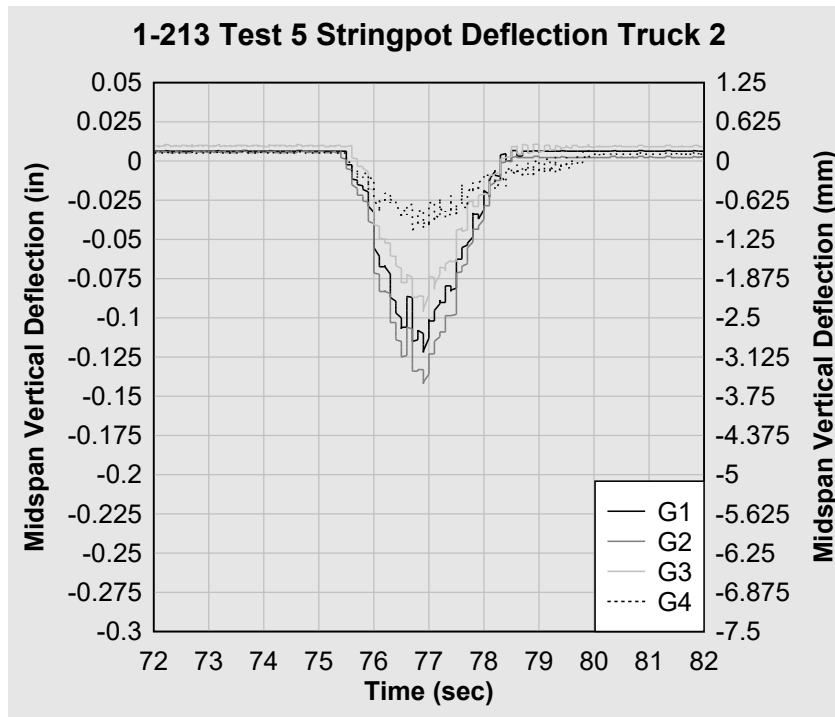


Figure 42. 1-213 Test 5 string pot truck 2 midspan deflection.

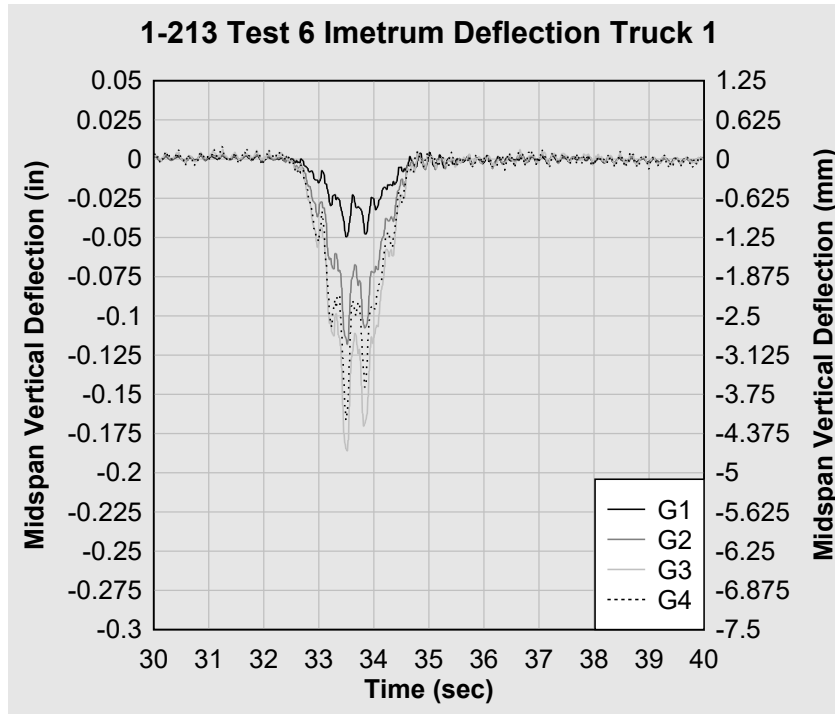


Figure 43. 1-213 Test 6 Imetrum truck 1 midspan deflection.

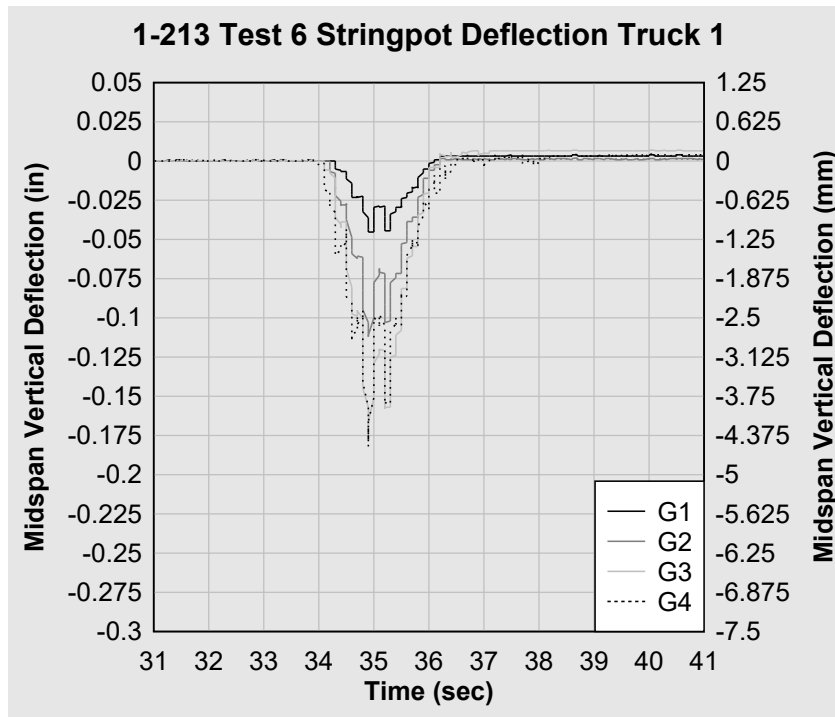


Figure 44. 1-213 Test 6 string pot truck 1 midspan deflection.

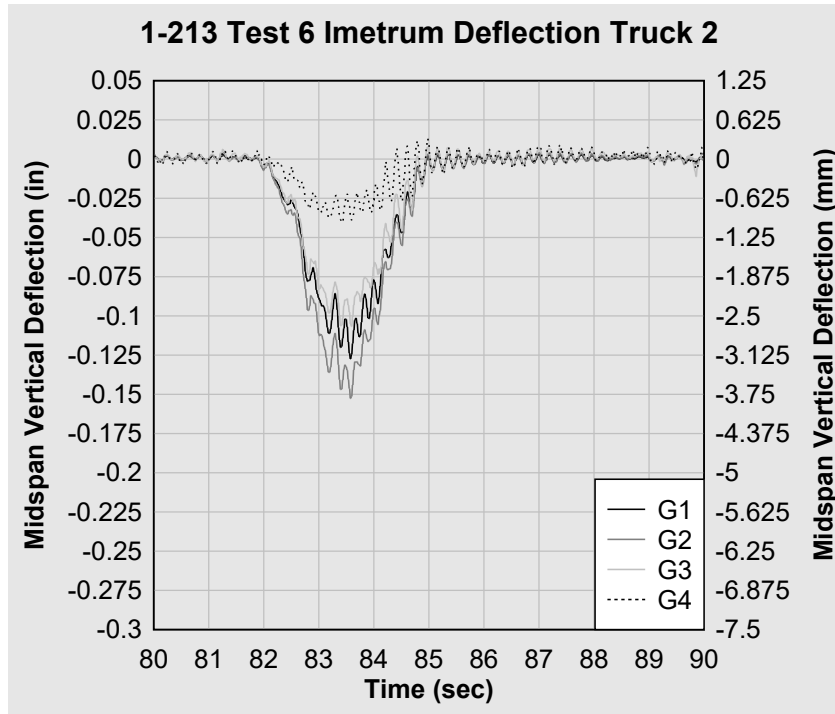


Figure 45. 1-213 Test 6 Imetrum truck 2 midspan deflection.

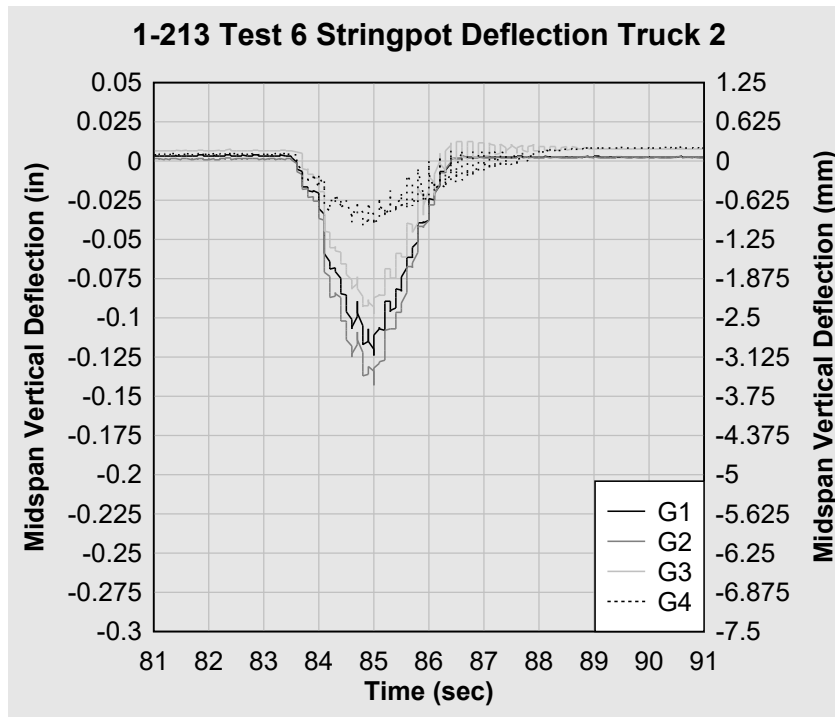


Figure 46. 1-213 Test 6 string pot truck 2 midspan deflection.

1-213 Test 5 Truck 1 Midspan Bottom Flange BDI Microstrain

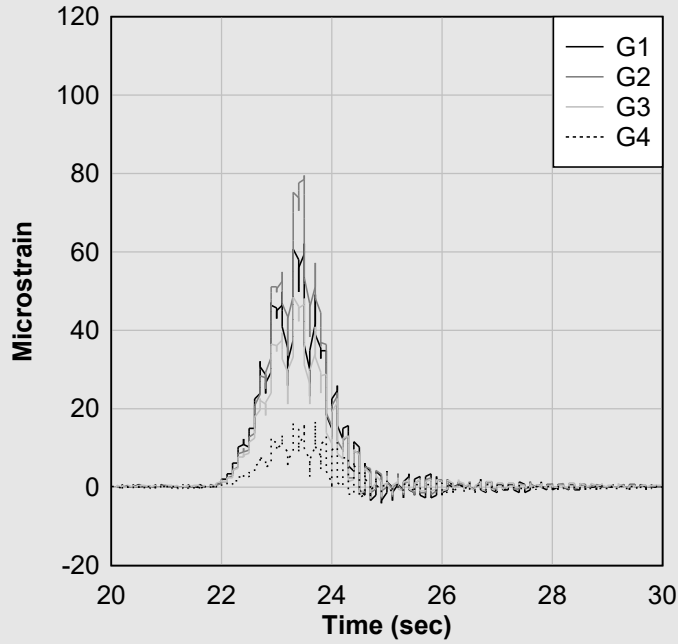


Figure 47. 1-213 Test 5 truck 1 midspan bottom flange BDI microstrain.

1-213 Test 5 Truck 2 Midspan Bottom Flange BDI Microstrain

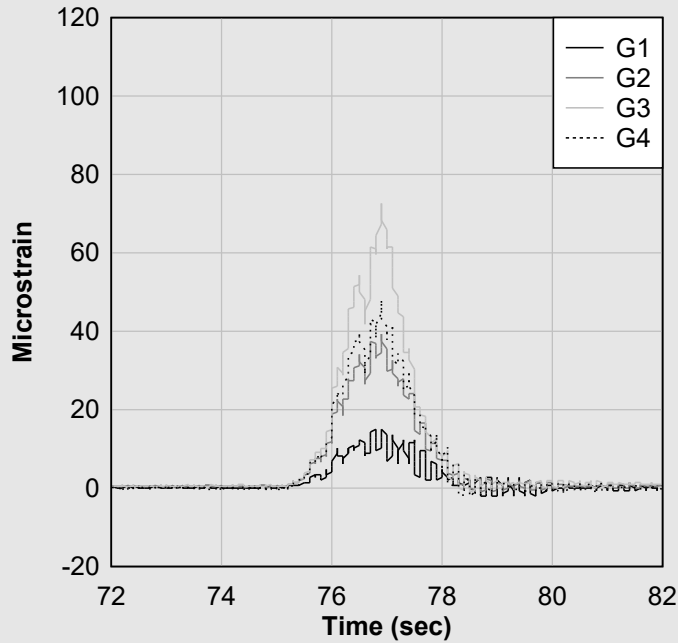


Figure 48. 1-213 Test 5 truck 2 midspan bottom flange BDI microstrain.

1-213 Test 6 Truck 1 Midspan Bottom Flange BDI Microstrain

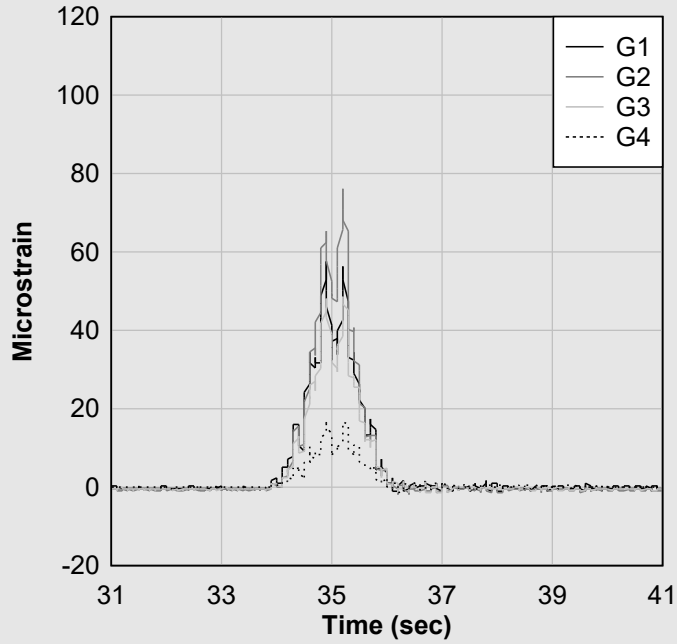


Figure 49. 1-213 Test 6 truck 1 midspan bottom flange BDI microstrain.

1-213 Test 6 Truck 2 Midspan Bottom Flange BDI Microstrain

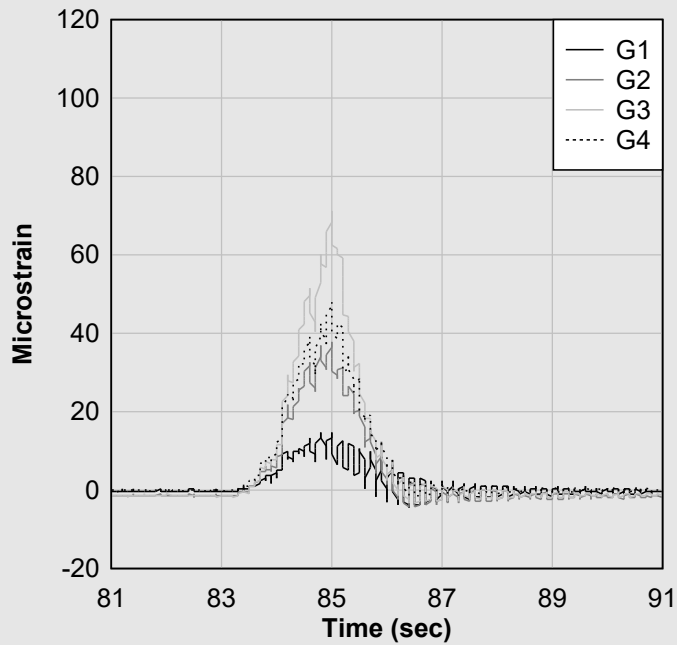


Figure 50. 1-213 Test 6 truck 2 midspan bottom flange BDI microstrain.

Trailing trucks pass in the same lane, one trailing the other as close as possible (slowly) time histories

Tests 7 and 8 are duplicate pseudo-static load tests that consist of two trucks passing over the right lane, with the second truck trailing the first as close as possible. Figures 51 through 54 are time-histories versus midspan displacement plots from Tests 7 and 8. Figures 55 and 56 are time-histories versus midspan bottom flange strain plots from Tests 7 and 8. The Imetrum and string-potentiometer resulted in similar midspan displacement readings. Tests 7 and 8 resulted in the largest displacement for Girder 1 (G1). The midspan strain readings display two separate peaks when the two trucks individually cross midspan, while the midspan deflection readings display one maximum. This dissimilarity occurs since deflection can be considered a global phenomenon, while strain is a seemingly more localized phenomenon.

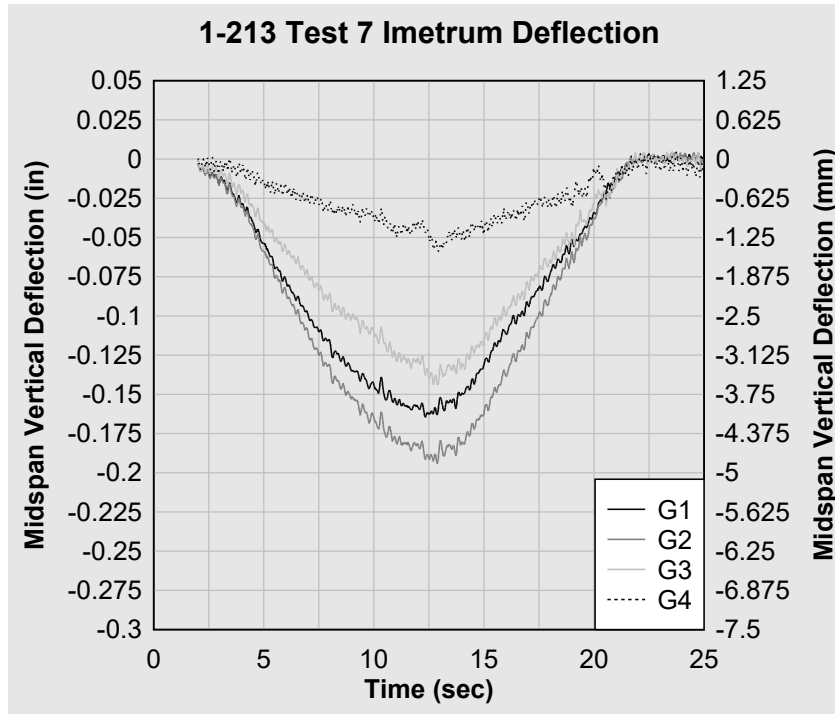


Figure 51. 1-213 Test 7 Imetrum midspan deflection.

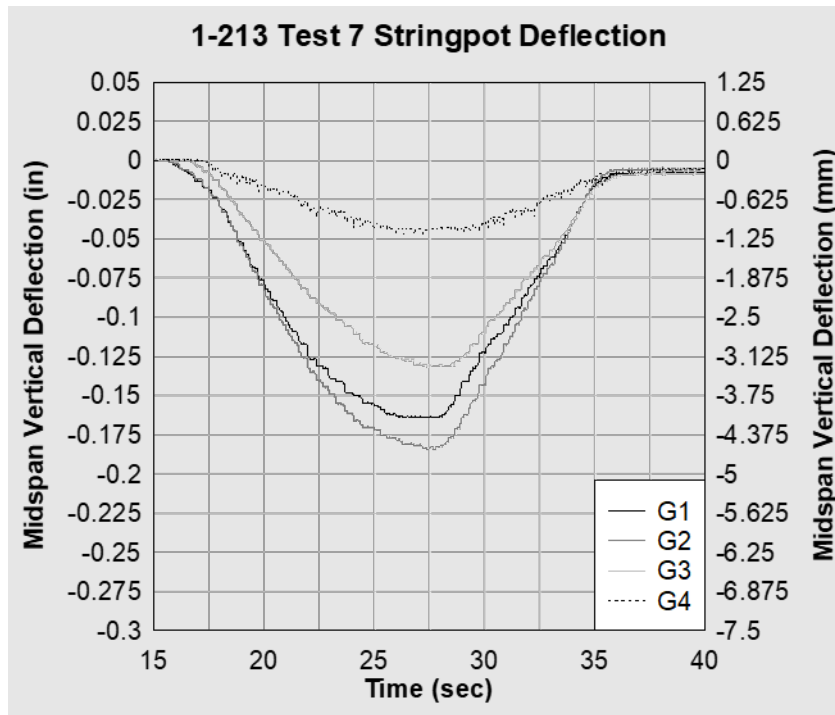


Figure 52. 1-213 Test 7 string pot midspan deflection.

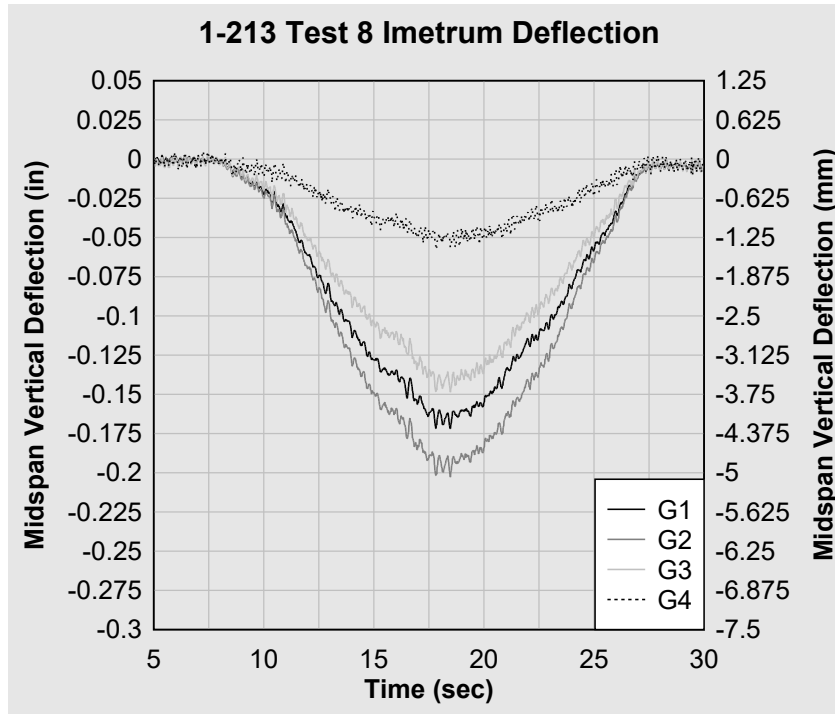


Figure 53. 1-213 Test 8 Imetrum midspan deflection.

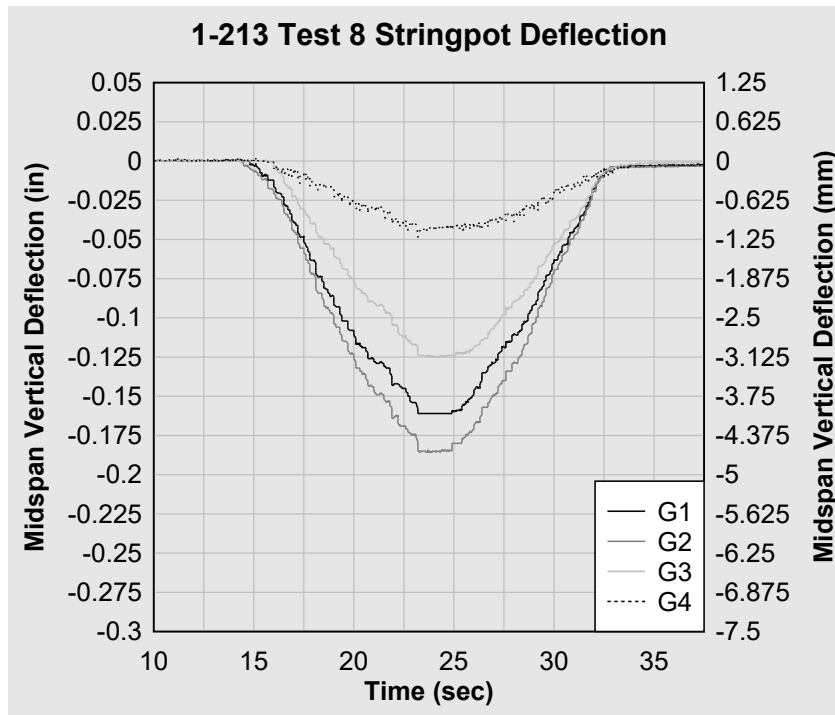


Figure 54. 1-213 Test 8 string pot midspan deflection.

1-213 Test 7 Midspan Bottom Flange BDI Microstrain

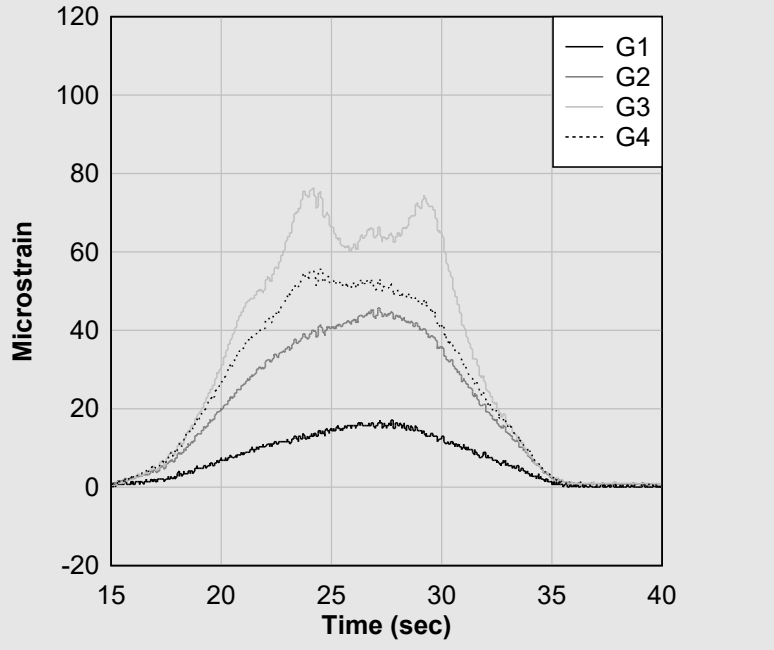


Figure 55. 1-213 Test 7 midspan bottom flange BDI microstrain.

1-213 Test 8 Midspan Bottom Flange BDI Microstrain

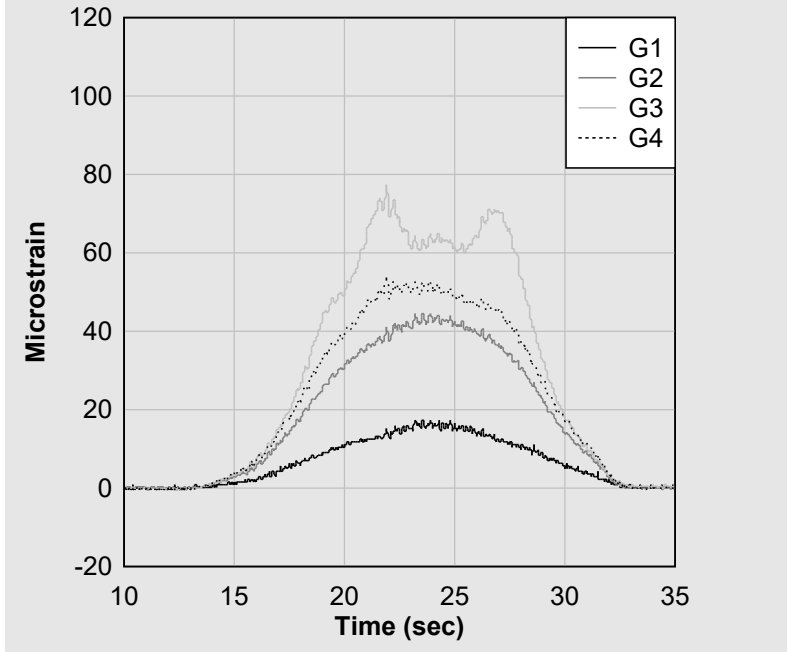


Figure 56 1-213 Test 8 midspan bottom flange BDI microstrain.

Girder Midspan Deflection Comparison

Figure 57 shows the maximum midspan deflection readings for all four girders of the left lane rolling truck pass of Tests 1 and 2. Figures 58 and 59 show the maximum midspan deflection readings for Tests 1 and 2, and midspan bottom flange BDI microstrain for truck tandem lane rolling passes for Tests 3, 4, and 9, respectively. The string-potentiometers, which were physically attached to the bottom of the target attachments, measured vertical displacements slightly less than the Imetrum system. Despite this differential between two data acquisition methods, the displacements are close enough in magnitude to assume that the displacement measurements are accurate to a high degree of confidence. This is a significant improvement from the 1-911S displacement results. The left-lane truck passes resulted in similar measurements from the Imetrum and string-potentiometers. While the right-lane truck passes resulted in similar measurements, there was a larger differential between the two systems than the left-lane passes. The right-lane passes were the second of two rolling passes; the non-contact Imetrum system was able to track the second truck of two consecutive passes more accurately than the attached string-potentiometers.

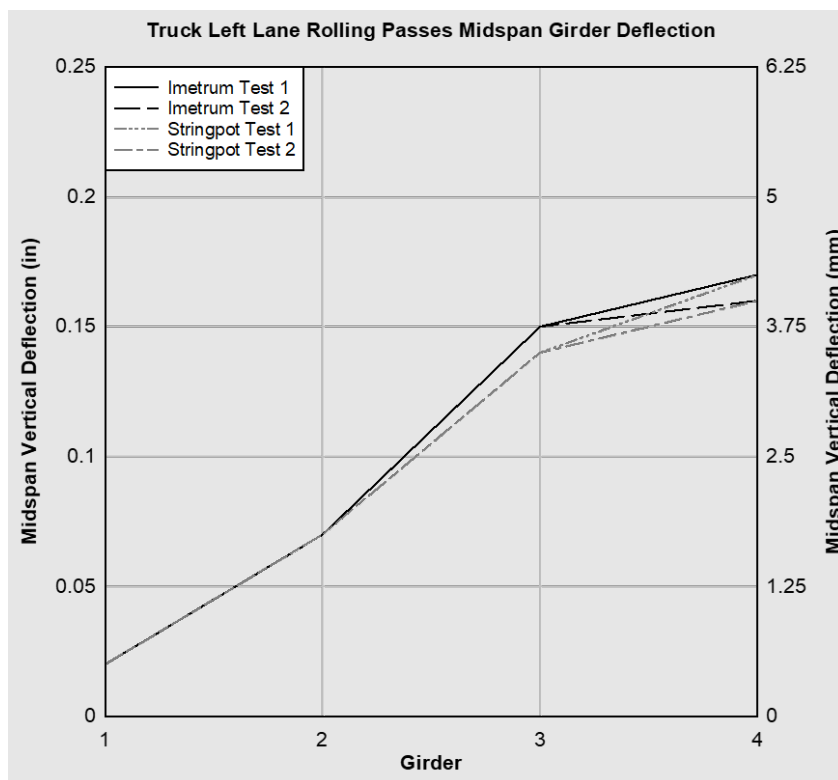


Figure 57. 1-213 Test truck left lane rolling passes midspan girder deflection.

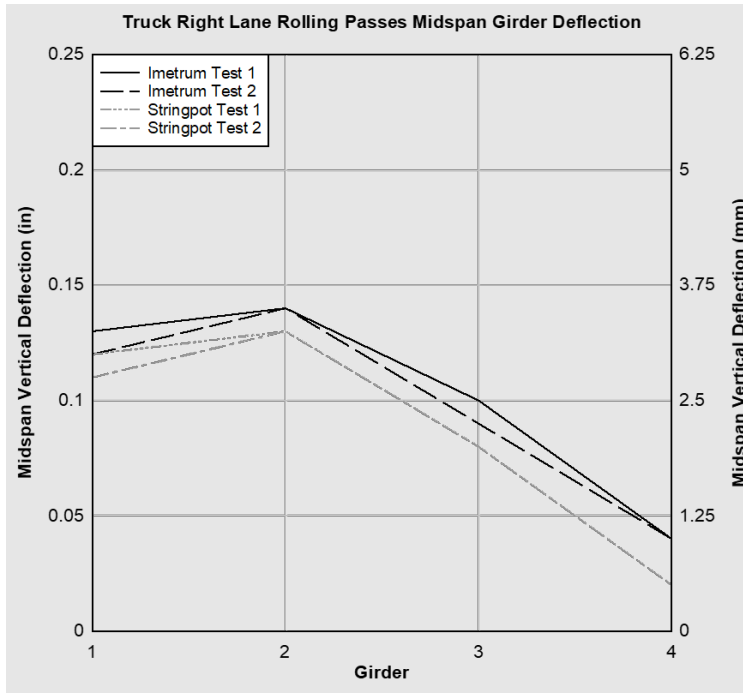


Figure 58. 1-213 Test truck left lane rolling passes midspan girder deflection.

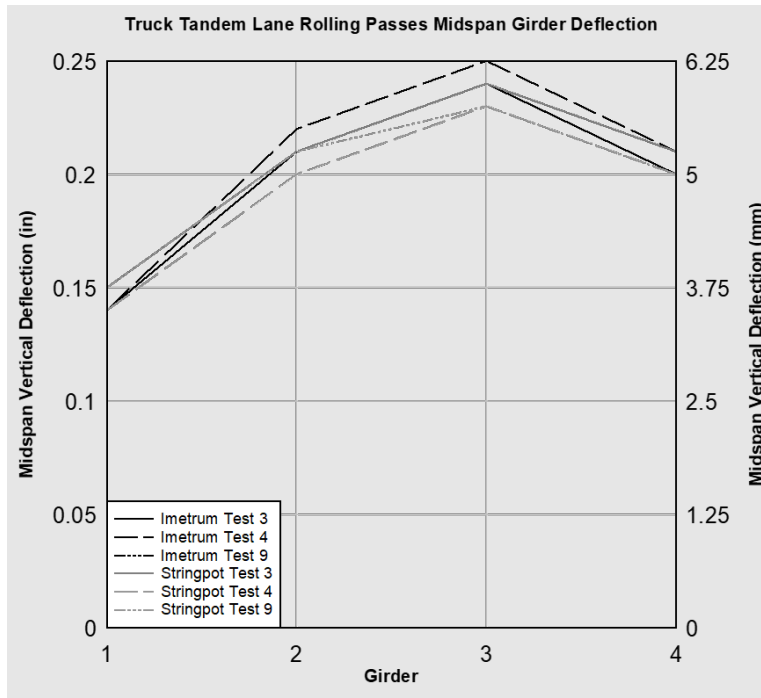


Figure 59. 1-213 Truck tandem lane rolling passes midspan girder deflection.

Girder Midspan Bottom Flange Strain and Live Load Distribution Factors Comparison

Figures 60 through 62 present maximum strain measurement from each girder’s midspan bottom flange BDI strain gauges. Figure 60 shows each girder’s maximum strain measurements for the left-lane truck passes. Figure 61 shows each girder’s maximum strain measurements for the right-lane truck passes. Figure 62 shows each girder’s maximum strain measurements for the tandem lanes truck passes. Figures 63 through 65 show comparisons of the lateral live-load distribution from three different methods of data acquisition: Imetrum displacement, string-potentiometers and BDI strain gauges. Figure 63 shows the lateral live-load distribution for the left-lane truck passes. Figure 64 shows the lateral live-load distribution for the right-lane truck passes. Figure 65 shows the lateral live-load distribution for the tandem lanes truck passes.

The string-potentiometers, which were physically attached to the bottom of the target attachments, measured vertical displacements slightly less than the Imetrum system. The differential between the two systems displacements is close enough in magnitude to assume that the displacement measurements are accurate to a high degree of confidence. Strain gauges on the bottom flange of each girder resulted in different distribution of live load. The left-lane truck passes show that Girder 3 (G3) carries the largest amount of midspan strain, while Girder 4 (G4) had the largest midspan deflection. The right-lane truck passes show Girder 2 (G2) taking the largest amount of midspan strain and deflection. For the right-lane passes, Girder 2 (G2) takes a larger portion of the total midspan strain than deflection. The tandem lanes truck passes show Girder 2 taking the largest amount of midspan strain, while Girder 3 (G3) had the largest deflection at midspan.

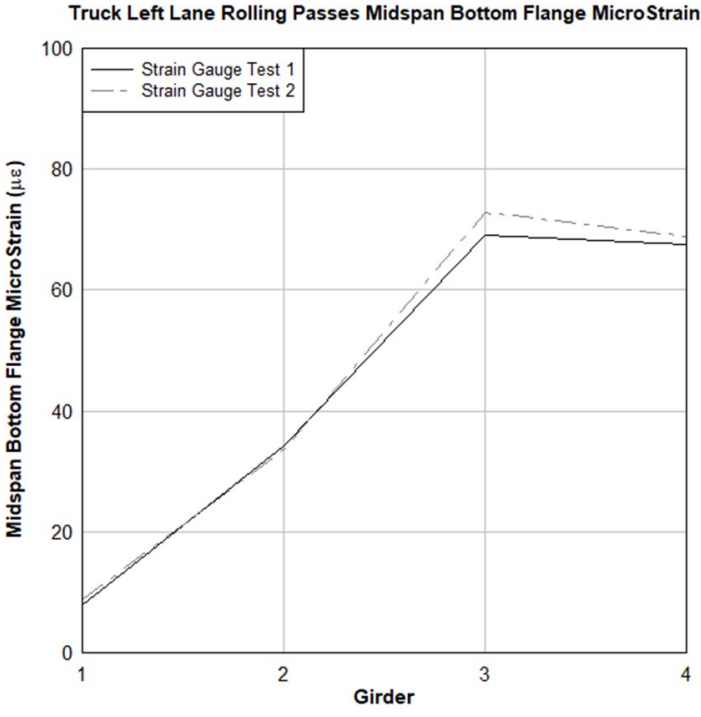


Figure 60. 1-213 Truck left lane rolling passes midspan bottom flange microstrain.

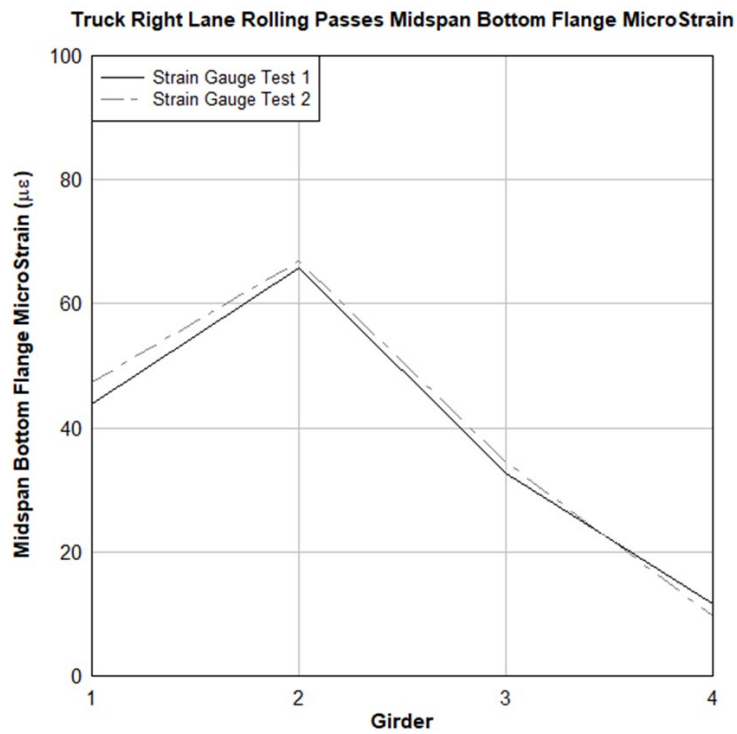


Figure 61. 1-213 Truck right lane rolling passes midspan bottom flange microstrain.

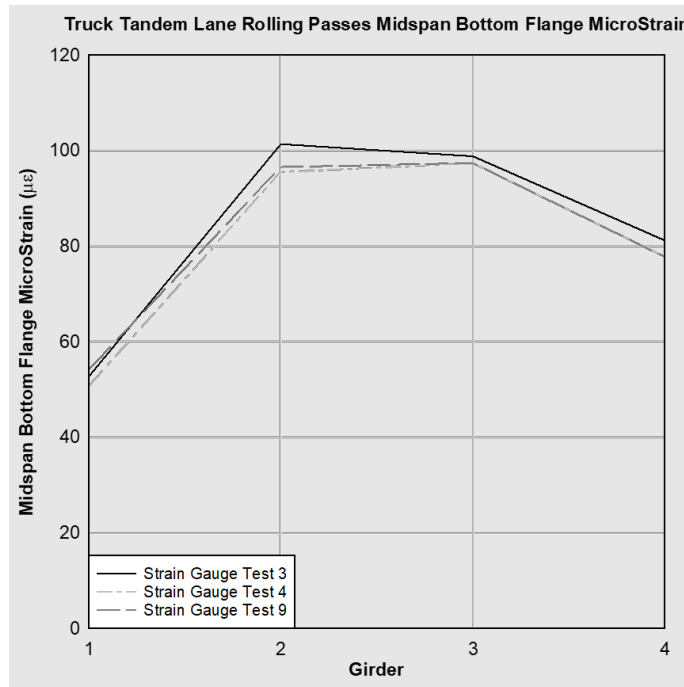


Figure 62. 1-213 Truck tandem lane rolling passes midspan bottom flange strain.

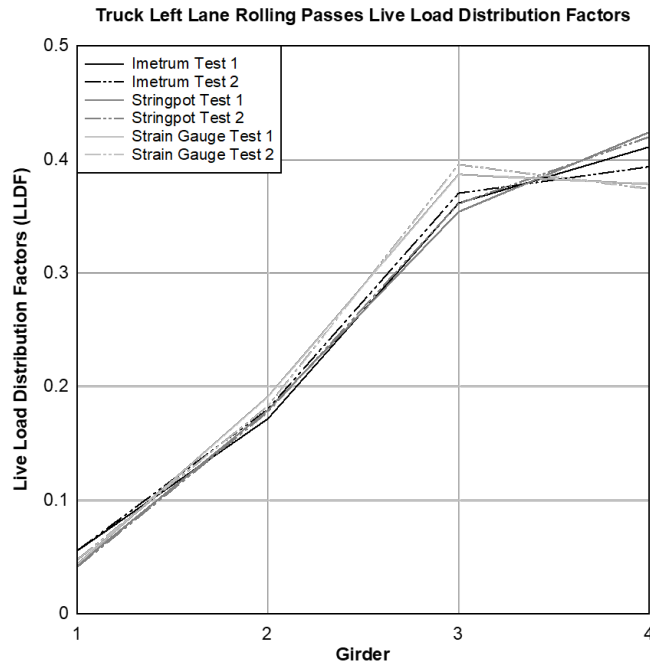


Figure 63. 1-213 Truck left lane rolling passes live load distribution factors.

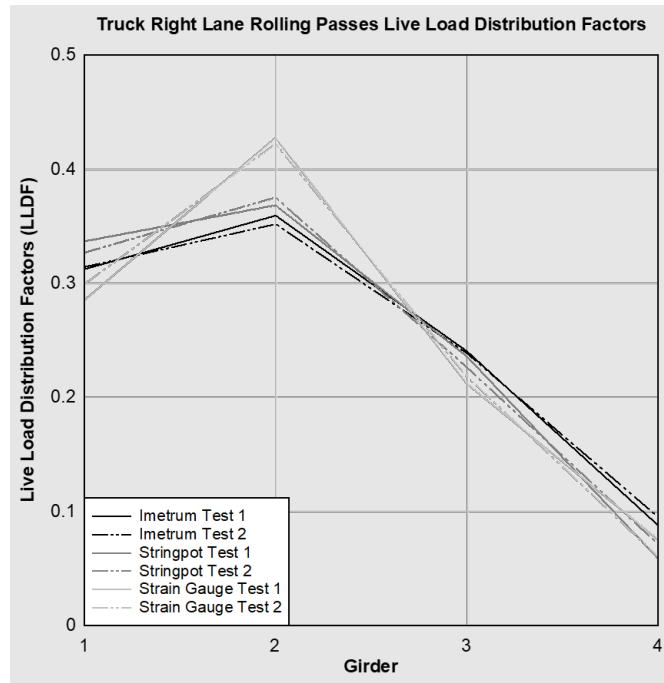


Figure 64. 1-213 Truck right lane rolling passes live load distribution factors.

Truck Tandem Lane Rolling Passes Live Load Distribution Factors

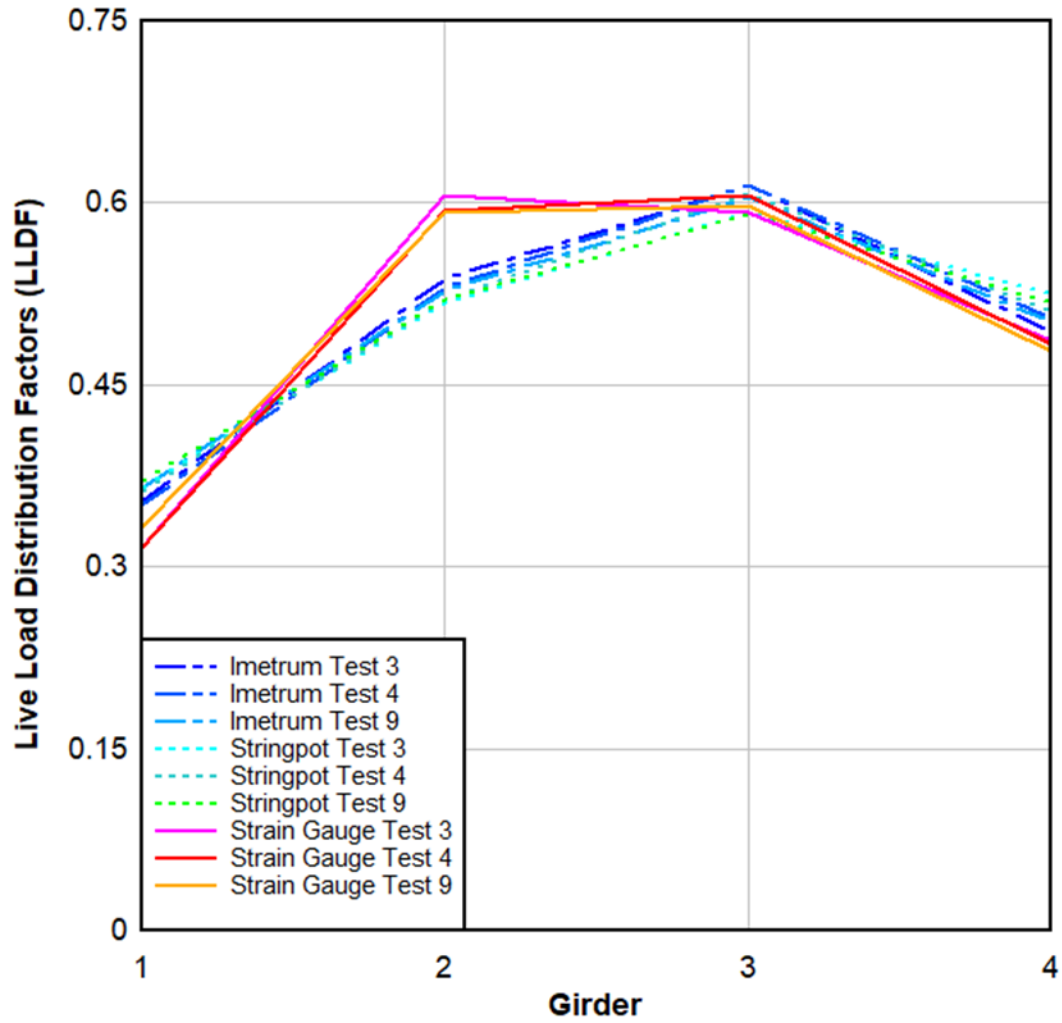


Figure 65. 1-213 Truck tandem lane rolling passes live load distribution factors.

Girder Midspan Displacement Tables Comparison

Table 8 shows a comparison of average maximum midspan displacement measurements by Imetrum VideoGauge™ and string-potentiometer of three rolling truck pass scenarios. The left-lane truck pass results are from the first truck pass of Tests 1 and 2. The right-lane truck pass results are from the second truck pass of Tests 1 and 2. The tandem lane truck pass results are from the tandem pass of Tests 3, 4, and 9. The Imetrum results match according to superposition better than the results from the string-potentiometer.

Table 8. 1-213 Girder midspan displacement comparison.

System	Girder 1		Girder 2		Girder 3		Girder 4	
	Ime	STP	Ime	STP	Ime	STP	Ime	STP
Left Lane (mm)	0.6	0.4	1.8	1.8	3.8	3.6	4.2	4.3
Right Lane (mm)	3.2	2.9	3.6	3.3	2.4	2.0	0.9	0.6
Tandem (mm)	3.7	3.7	5.4	5.2	6.3	6.0	5.1	5.2

Note: Ime = Imetrum; STP = Stringpot

Live-load distribution factors for each truck load per beam were calculated using the midspan strain and displacement measurement from the strain transducers and string-potentiometers placed on the bottom flange of each girder at midspan, and from the Imetrum system. Tables 9, 10, and 11 show the results from the strain, string-potentiometer and Imetrum displacement measurements along with the LLDFs computed per girder for the left lane, right lane, and tandem lanes truck passes.

Table 9. Live load distribution factors (LLDF) for left lane truck pass.

Girder	1	2	3	4
Strain ($\mu\epsilon$)	8	34	71	68
Imetrum Disp (mm)	0.6	1.8	3.8	4.2
Stringpot Disp (mm)	0.4	1.8	3.6	4.3
LLDF $\mu\epsilon$	0.05	0.19	0.39	0.38
LLDF Δ Imetrum	0.06	0.18	0.37	0.40
LLDF Δ Stringpot	0.04	0.18	0.36	0.42

Table 10. Live load distribution factors (LLDF) for right lane truck pass.

Girder	1	2	3	4
Strain ($\mu\epsilon$)	46	66	34	11
Imetrum Disp (mm)	3.2	3.6	2.4	0.9
Stringpot Disp (mm)	2.9	3.3	2.0	0.6
LLDF $\mu\epsilon$	0.29	0.42	0.22	0.07
LLDF Δ Imetrum	0.31	0.36	0.24	0.09
LLDF Δ Stingpot	0.33	0.37	0.23	0.07

Table 11. Live load distribution factors (LLDF) for tandem lane truck pass.

Girder	1	2	3	4
Strain ($\mu\epsilon$)	53	98	98	79
Imetrum Disp (mm)	3.7	5.4	6.3	5.1
Stringpot Disp (mm)	3.7	5.2	6.0	5.2
LLDF $\mu\epsilon$	0.32	0.60	0.60	0.48
LLDF Δ Imetrum	0.36	0.53	0.61	0.50
LLDF Δ Stringpot	0.37	0.52	0.60	0.52

Bridge 1-213 Finite Element Model Development

ABAQUS/CAE (2019) is utilized to create a bridge model for the finite element analyses. Using ABAQUS, the superstructure of the 70-ft span, four steel girder with composite concrete deck was modeled with three separate groups of solid elements: the four steel girders, the concrete deck, the sidewalk, and two bridge parapets. Since bridge plans were not available, the concrete deck's strength of the bridge parapets and sidewalk are unknown. All the dimensions in the model are based on measurements from on-site measurements. No concrete coring was taken through the bridge deck; the most common thickness for a composite steel girder bridge of this size and span length of 8.5" thick was assumed. Models with and without lateral stiffeners connecting girders at their end spans, quarter spans, and midspans were compared. Studies concluded that the effects of lateral bracing in the model had a negligible impact on the model displacements, strains, and distributions of load. Figure 66 shows the stiffeners on the bridge and the ABAQUS model.

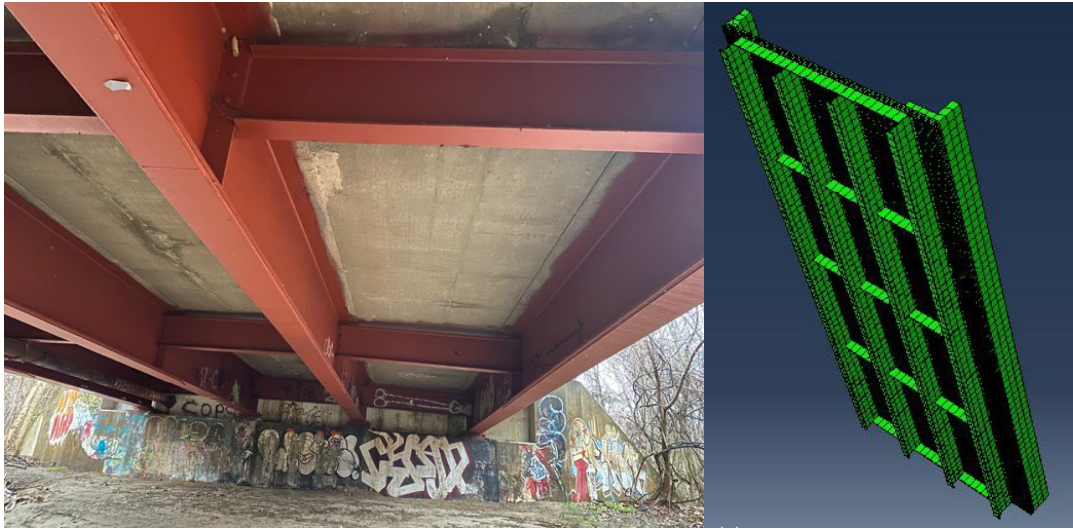


Figure 66. Underside of bridge superstructure photo and ABAQUS model (ABAQUS/CAE 2019).

All solid elements were discretized as 8-node linear hexahedral bricks. A mesh sensitivity analysis was performed for the steel girders and the concrete deck; mesh convergence of the steel girders occurred at a courser mesh than the concrete deck. The final meshing maintained typical element for the concrete deck of 3" and 12" for the steel girders. The bridge parapets and sidewalk were modeled with a mesh over 12". Meshing the concrete deck with a finer mesh than 3" resulted in computer crashes. The model included two defined materials: steel and reinforced concrete. Steel with a mass density of $2.84E-4$ kips/in³; a Young's modulus of $E = 29,000$ ksi; and a Poisson's ratio = 0.3. Concrete with a mass density of $8.391E-05$ kips/in³; a concrete compressive strength varying from 3865 ksi – 5,762 ksi; and a Poisson's ratio = 0.2).

The Imetrum midspan displacement readings were used to calibrate the model. Live-load distribution factors are computed using conventional methods per the *AASHTO LRFD Bridge Design Specifications* (2020) and the finite element model data for moment and deflection to evaluate the lateral distribution due to live load. The lateral distribution LLDF for truck load per beam (LLDF_{truck}) was calculated and compared. Tables 12 and 13 show a comparison of the LLDF load testing (measured field data), finite element modeling using ABAQUS for 1-lane (single lane) and multiple lanes (M-lanes), and AASHTO LRFD (2020) approximates for the distribution factors (mg) for moment, assuming non-composite beam behavior.

Table 12. Comparison of LLDFs for deflection computed using various methods.

Deflection					
Field Test Ime (mg)		Field Test STP (mg)		ABAQUS (mg)	
1-lane	M-lanes	1-lane	M-lanes	1-lane	M-lanes
0.40	0.61	0.42	0.60	0.45	0.62

Table 13. Comparison of LLDFs for moment computed using various methods.

Moment					
AASHTO (mg)		Field Test (mg)		ABAQUS (mg)	
1-lane	M-lanes	1-lane	M-lanes	1-lane	M-lanes
0.46	0.63	0.39	0.60	0.44	0.61

Bridge 1-213 Finite Element Modeling: Parametric Studies

Parametric studies using the ABAQUS finite element model were conducted to assess the sensitivity of the following parameters on the model results: (1) concrete compressive strength, (2) model boundary conditions for the bearings, and (3) positioning of truck load within the cross-section. Analyses with compressive strength ranging from 4,500 psi – 10,000 psi were performed. The bearings were modeled as pin and roller. Table 14 shows a comparison of midspan deflections for the tandem truck pass loading for four different concrete compressive strengths as well as the average reading from the Imetrum system from truck passes 3, 4, and 9.

Concrete compressive strength

The model with the 4,500-psi concrete measured midspan deflections closest to the average Imetrum readings from the live-load test for the tandem truck passes. The distribution of deflections from the generated model did not match the results from the field tests. To have the model have a similar load distribution to the field tests, parametric studies on the locations of the truck loads were computed and are discussed in more detail (Timber, 2022) after an investigation on representing the boundary conditions of the beams.

Table 14. 1-213 Bridge model midspan deflection comparison of concrete compressive strength versus load test readings.

f'c (psi)	G1 Δ (mm)	G2 Δ (mm)	G3 Δ (mm)	G4 Δ (mm)
4500	3.50	5.67	6.27	4.64
6000	3.38	5.37	5.95	4.44
8000	3.20	4.99	5.52	3.98
1000	3.06	4.70	5.19	3.76
Imetrum	3.66	5.45	6.28	5.12

Boundary conditions

Three approaches to modeling the boundary conditions for this single-span bridge with DeIDOT standardized fixed-expansion bearings were analyzed. The *first* approach idealized the bearings as pin and roller. The fixed-ended side of the girders allowed no translation in all three cartesian directions on the fixed bridge end. The expansion-ended side allowed no translation in the vertical direction. The *second* approach idealized the bearings as fixed and roller. The fixed-ended side of the girders allowed no translation or rotation in all three cartesian directions on the fixed bridge end. The expansion-ended side allowed no translation in the vertical direction. The *third* approach consisted of applying slight moment restraint to the fixed bearings and modeling the expansion bearings as pins restricting vertical and longitudinal movement. To determine how much rotational displacement should be applied to the fixed bearings, the method of virtual work for beams and frames was utilized. The method of virtual work was applied for a three-axle load scenario for a simply supported beam spaced out based on the distance between DeIDOT truck axles. Equation 3.1 is the method of virtual work, which was used to determine the amount of rotation at the beam's two ends from a three-axle load. M is internal moment in the beam caused by the axle loading, m is the applied rotation of 1*kip*in*rad at the fixed bearing. Integration occurred over four separate segments along the span.

$$\theta = \int \frac{m * M}{EI} * dx \tag{3.1}$$

Using virtual work, rotational displacements, θ , were computed by assigning the amount of load on each beam based on the distribution of the Imetrum midspan displacements. θ was determined for all four girders using composite girder moment of inertia for concrete compressive strength $f'c$, of 4,500 psi. Table 15 shows rotational displacement for all girders based on concrete compressive strength.

Table 15. Rotational displacement for all girders based on concrete compressive strength.

f'c (psi)	G1 θ (rad)	G2 θ (rad)	G3 θ (rad)	G4 θ (rad)
4,500	0.0031	0.0046	0.0053	0.0043

With the proper rotational displacements computed and applied to individual models, the three boundary condition approaches could be compared. Table 16 shows a comparison of midspan deflections for the tandem truck pass loading for the three-boundary condition approaches as well as the average reading from the Imetrum system from truck passes 3, 4, and 9.

Table 16. 1-213 bridge model midspan deflection comparison of boundary condition versus load test readings.

BC	G1 Δ (mm)	G2 Δ (mm)	G3 Δ (mm)	G4 Δ (mm)
pin-rol	3.50	5.67	6.27	4.64
fix-rol	2.17	4.31	5.04	3.75
θ- rol	2.27	4.89	5.92	4.96
Imetrum	3.66	5.45	6.28	5.12

The first approach, which idealized the bearings as pin and roller, resulted in midspan deflections closest to the Imetrum load test readings. However, the distribution of deflection did not match the Imetrum readings. To have the model more accurately represent how the bridge measured midspan deflections, the loading of the bridge was investigated.

Loading position

To understand the effect of the load positioning on the bridge, analyses were conducted to assess the load placement, since the trucks may not have been exactly centered in the driving lane. Figure 67 shows the initially assumed axle locations along the cross-section of the bridge. The two DeIDOT trucks were represented by idealizing each wheel load as point loads. The alignment of the loads along the cross-section of the bridge was initially modeled along the centerline of the two 13-ft-wide lanes.

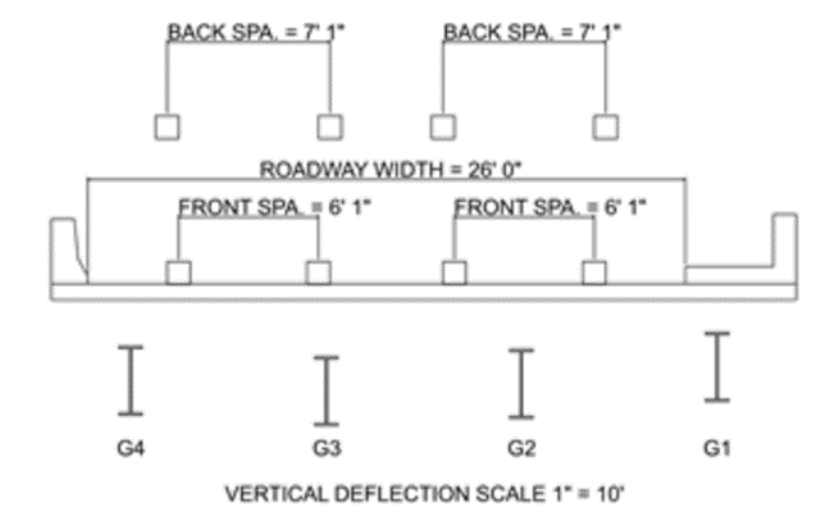


Figure 67. Bridge section view and truck axle locations, assuming trucks pass at the centerline of both lanes.

The distribution of displacement and strains in the ABAQUS model did not match what was measured in the load test and photos of the tandem truck passes. Figure 68 includes photos of the trucks passing over the bridge. In the photo it appears that the trucks are not passing along the centerline of the two lanes. To investigate how the bridge was loaded, a series of models were analyzed where the wheel loads were offset 1 ft and 2 ft closer to the bridge parapet without a sidewalk.



(a)



(b)

Figure 68. 1-213 Bridge field test tandem truck pass photos (a) and (b).

Analyses varying axle loading locations along the bridge cross-section found that placing the truck that was closer to the sidewalk along the lane centerline and placing the second truck 2 ft offset from the lane centerline toward the lane's parapet netted midspan displacements quite like the Imetrum measurements. Figure 69 shows a comparison of Imetrum midspan displacements for 1-213 Tests 3, 4, and 9 tandem truck pass and the ABAQUS model loaded in four different ways. The model that had midspan displacement most like the load test had the right truck along the centerline of the right lane and the left truck 2 ft offset toward the parapet from the centerline of the left lane. The concrete deck strength for these models was 4,500 psi.

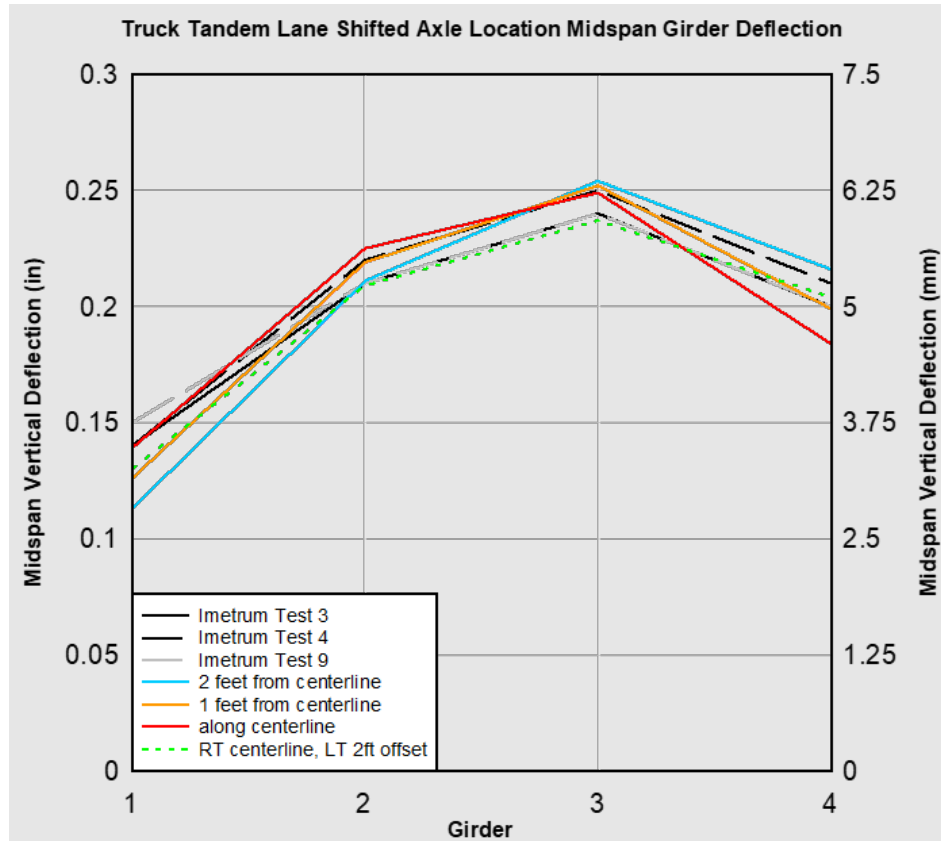


Figure 69. Bridge Imetrum and F.E.M. truck tandem lane shifted axle location midspan girder deflection.

Figure 70 shows a comparison of Imetrum midspan displacements for 1-213 Tests 3, 4, and 9 tandem truck pass and the ABAQUS model. The finalized ABAQUS model resulted in midspan deflections in close range to the field test results from the Imetrum system.

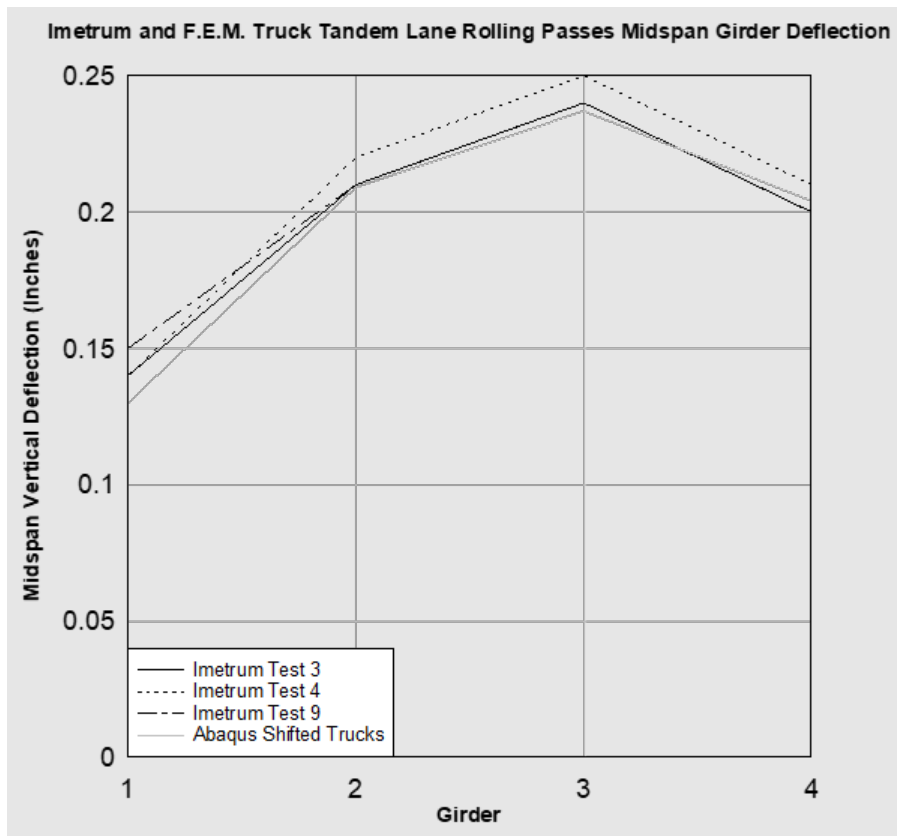


Figure 70. 1-213 Imetrum and F.E.M. truck tandem lane rolling passes midspan girder deflection.

Figure 71 shows a comparison of BDI midspan bottom flange strain for 1-213 Tests 3, 4, and 9 tandem truck pass and the ABAQUS model. The finalized ABAQUS model resulted in noticeably different midspan bottom flange strain than the field test results from the BDI system.

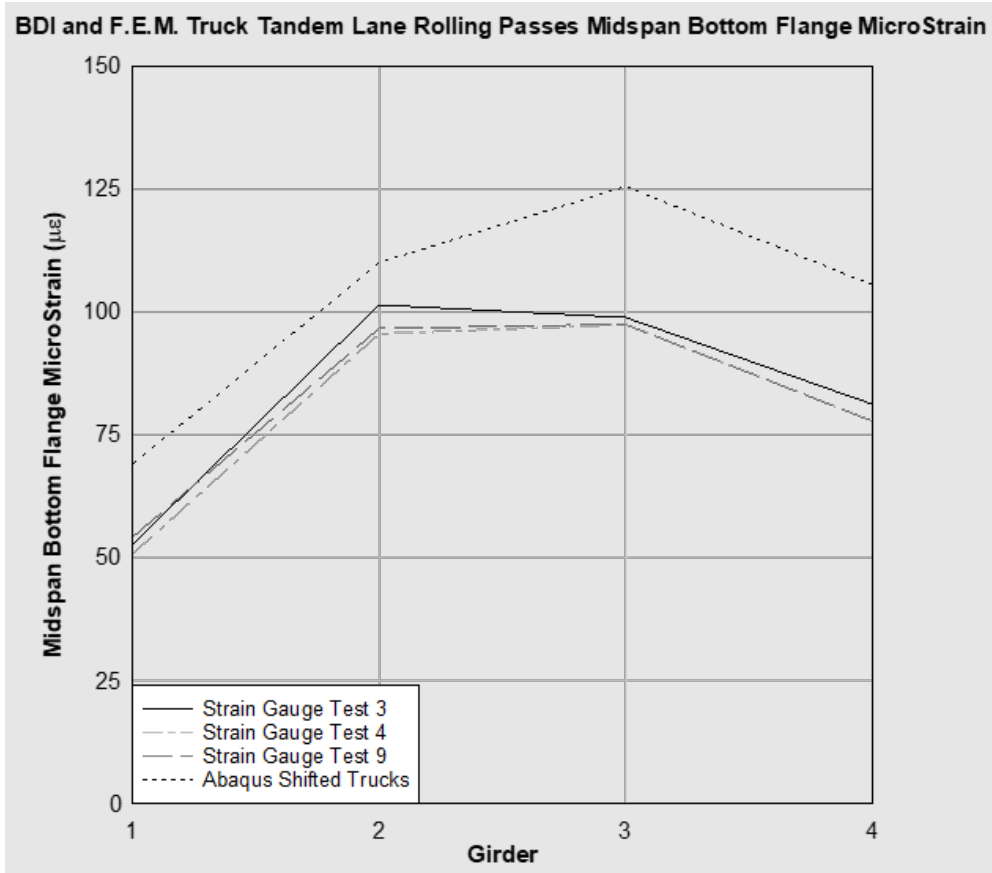


Figure 71. 1-213 Imetrum and F.E.M. truck tandem lane rolling passes midspan girder deflection.

Final Selection of Bridge Model Calibrated from Load Test Results

Figure 65 shows the LLDF based on midspan bottom flange strain results from Tests 3, 4, and 9 tandem truck pass and the ABAQUS model of DE bridge 1-213. The finalized ABAQUS model resulted in midspan deflection LLDF similar to the field test results from the Imetrum system. Figure 66 shows the LLDF based on midspan bottom flange strain results from Tests 3, 4, and 9 tandem truck pass and the ABAQUS model of bridge 1-213. The finalized ABAQUS model resulted in midspan bottom flange strain LLDF that distributed the truck loads differently than the field test's strain gauges. The ABAQUS model distributed midspan deflection and strain similarly, which was not the case from the field test.

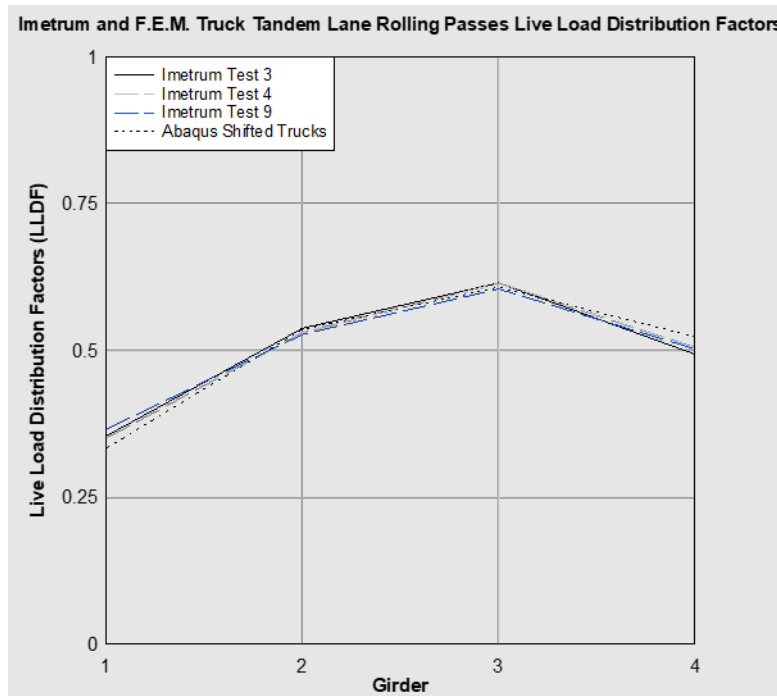


Figure 72. 1-213 Imetrum and F.E.M. truck tandem lane rolling passes deflection live load distribution factors.

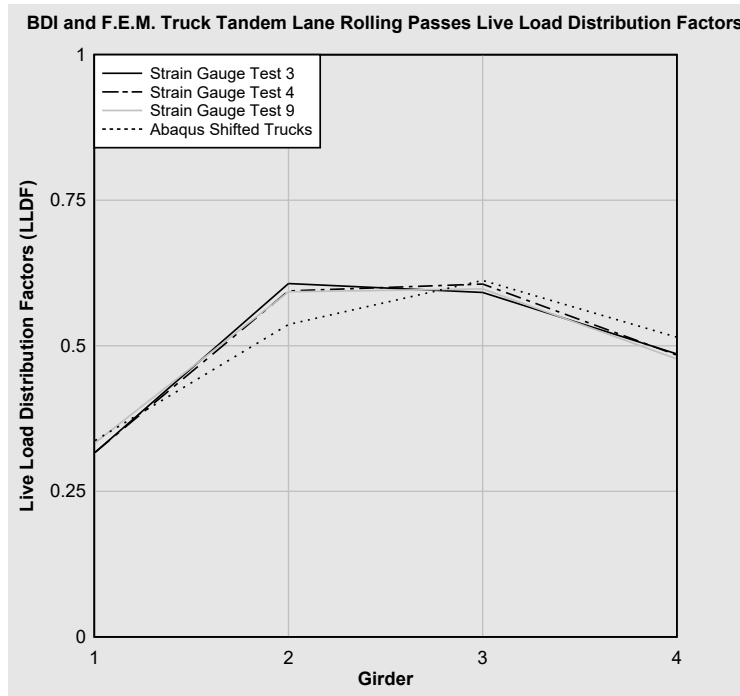


Figure 73. 1-213 Imetrum and F.E.M. truck tandem lane rolling passes strain live load distribution factors.

Without any bridge plans, midspan displacement and strain distributions can be used to adjust finite element models with some success. Many models were able to generate similar displacements to the field tests but not similar strains. Placing strain gauges on the top flange of girders would have helped with understanding how compositely the girder and concrete deck are acting.

Live-load distribution factor comparisons

All of these models could be used to compare distribution factors with standard AASHTO methodology and load tests results. Tables 17 and 18 show a comparison of the LLDF load testing (measured field data), finite element modeling using ABAQUS for 1-lane (single lane) and multiple lanes (M-lanes), and AASHTO LRFD (2020) approximates for the distribution factors (mg) for moment, assuming non-composite beam behavior.

Table 17. Comparison of LLDFs for deflection.

Deflection					
Field Test lme (mg)		Field Test STP (mg)		ABAQUS (mg)	
1-lane	M-lanes	1-lane	M-lanes	1-lane	M-lanes
0.40	0.61	0.42	0.60	0.45	0.62

Table 18. Comparison of LLDFs for moment.

Moment					
AASHTO (mg)		Field Test (mg)		ABAQUS (mg)	
1-lane	M-lanes	1-lane	M-lanes	1-lane	M-lanes
0.46	0.63	0.39	0.60	0.44	0.61

Standard AASHTO methodology provides more conservative distribution factors than load test results and finite element models; therefore, there are benefits to load testing and modeling bridges that have substandard load capacity based on inspection report or AASHTO methodology. This is a good example of a case where some key features related to the physical structure are unavailable and thus complicate the construction of a valid mathematical model.

Results from 3D Point Cloud Analysis

The photogrammetric 3D point cloud analysis was used to generate measurements of the static load test deflections at the midspan. Overall measurement accuracy was indicated to be approximately +/- 1 mm. For example, for a static load deflection of 3.5 mm, as measured by the string potentiometers, the point cloud measurement methods varied between 2.8 mm and 4.6 mm. Observed variances were due to algorithmic choices in the alignment and registration processes, as well as the choice of distance metric employed to quantify deflections. Overall, the results show potential, but care must be taken to ensure that the measurement threshold of 1mm is not exceeded in a desired field application.

CHAPTER 4

Recommendations

LIVE LOAD DISTRIBUTION FACTORS USING DEFLECTION MEASUREMENTS

Currently AASHTO (2020) has equations for determining live-load distribution factors for moment and shear but not for displacement. The AASHTO equations are provided in tables based on the type of bridge superstructure. The equations provided below are applicable for the following superstructures: Concrete Deck or Filled Grid, Partially Filled Grid, or Unfilled Grid Deck Composite with Reinforced Concrete Slab on Steel or Concrete Beams; Concrete T-beams, T- and Double T-sections.

Equation 4.1 is used to quantify Live Load Distribution Factor for Moment in Interior Beams for One Design Lane Loaded. Equation 4.2 is used to quantify Live Load Distribution Factor for Moment in Interior Beams for Two or More Design Lanes Loaded, where S is the spacing of beams or webs (ft), L is the span of beam (ft), and t_s is the depth of concrete slab. Kg is the longitudinal stiffness parameter quantified using Equation 4.3, where E_b is the modulus of elasticity of beam material (ksi), E_d is the modulus of elasticity of deck material (ksi), A is the non-composite cross section area (in²), and e_g is the distance between the centers of gravity of the basic beam and deck (in).

$$DF = 0.06 + \left(\frac{S}{14}\right)^{0.4} * \left(\frac{S}{L}\right)^{0.3} * \left(\frac{Kg}{12.0 * L * t_s^3}\right)^{0.1} \quad (4.1)$$

$$DF = 0.075 + \left(\frac{S}{9.5}\right)^{0.6} * \left(\frac{S}{L}\right)^{0.2} * \left(\frac{Kg}{12.0 * L * t_s^3}\right)^{0.1} \quad (4.2)$$

$$Kg = \frac{Eb}{Ed} * (1 + A) * (e_g)^2 \quad (4.3)$$

The level rule is used to quantify the LLDF for Moment in Exterior Longitudinal Beams for One Design Lane Loaded. Equation 4.4 is used to quantify Live Load Distribution Factor for Moment in Exterior Beams for Two or More Design Lanes Loaded, where $g_{interior}$ is live-load distribution factor representing the number of design lanes and the correction factor, e , is quantified using Equation 4.5.

$$g = e * g(interior) \quad (4.4)$$

$$e = 0.77 + \frac{de}{9.1} \quad (4.5)$$

Equation 4.6 is used to quantify Live Load Distribution Factor for Shear in Interior Beams for One Design Lane Loaded. Equation 4.7 is used to quantify Live Load Distribution Factor for Shear in Interior Beams for Two or More Design Lanes Loaded.

$$DF = 0.36 + \frac{S}{25} \quad (4.6)$$

$$DF = 0.2 + \frac{S}{12} - \left(\frac{S}{35}\right)^{2.0} \quad (4.7)$$

The level rule is used to quantify Live Load Distribution Factor for Shear in Exterior Beams for One Design Lane Loaded. Equation 4.8 is used to quantify Live Load Distribution Factor for Shear in Interior Beams for Two or More Design Lanes Loaded, where $g_{interior}$ is the live-load distribution factor representing the number of design lanes and the correction factor, e , is quantified using Equation 4.9.

$$g = e * g(interior) \quad (4.8)$$

$$e = 0.64 + \frac{de}{12.5} \quad (4.9)$$

Despite there being no AASHTO LLDF equations based on deflection measurements, the distribution factors provided for moment could be compared to deflection. The results from the bridge live-load tests conducted in this research as well as the finite element models generated could be compared to the AASHTO moment LLDF. The standard AASHTO equations provided are more conservative than the results from load testing and bridge models.

Discussion

The Imetrum VideoGauge™ was able to be calibrated effectively with and without targets placed on the bridge. To calibrate a plane with a significant perspective within a video file, the minimum amount of information required is one known length and two auxiliary lines that are parallel. To track displacement at a particular location, there needs to be a distinct difference between that tracking location and the area surrounded by the location. For the two bridges evaluated, the LLDFs based on deflection measurements were in good agreement with the lateral distribution factors obtained from the strain measurements, which are needed input per the MBE (AASHTO, 2018) to perform a load rating. The deflection LLDF measurements were like the moment results from the load test. More studies will need to be conducted to verify this load testing approach.

The results of the two controlled load tests demonstrated that both the Imetrum and phase-based analysis methods were able to measure displacement magnitudes similar to those captured by string potentiometers installed on the bridge. It should be noted that there was no specified acceptable accuracy threshold for these tests. Rather, the goal was to gain an understanding of practical measurement limits of each approach under field conditions. To that end, several observations of the relative measurement accuracy can be made. The first is that the Imetrum system more closely matched the string potentiometer measurements across all tests, with a maximum relative error of 0.4 mm. The maximum relative error for the phase-based system was 0.7 mm. Some of this difference is likely due to the additional signal processing applied to both the string potentiometer data and the Imetrum data. The Imetrum camera system may also have been better optimized for image capture due to its placement underneath the bridge. However, further analysis suggests that the target-tracking of the Imetrum system may be less prone to environmental variations and pixel-scale distortions in the video data as well. These differences are most notable at intervals of lower displacement amplitudes.

From a logistical point of view, setup for the video measurement methods was significantly faster than mounting physical instrumentation and minimized traffic disruptions. The trade-off for this logistical convenience was the additional complexity of the camera setup process and data processing. This additional complexity includes the choice of camera focal length, camera positioning, target installation (for the Imetrum method), and the need for more sophisticated calibration and data processing. Many of these choices are not as readily obvious as the ideal location for sensor placements and require specialized technical training.

In comparing the two vision methods, the differences can be thought of as a trade-off between flexibility of deployment and measurement accuracy. The Imetrum system required target installation for optimal accuracy. While not nearly as disruptive to traffic as a sensor installation, this still necessitated traffic stoppages. The Imetrum approach also restricted camera placement and required additional space for computing peripherals, though this also allowed for data visualization in the field. As a result, the phase-based method was more flexible and less disruptive to deploy. However, the logistical advantages of the phase-based method were offset by a loss of measurement accuracy and increased sensitivity to variations in camera configurations and recording setups. Although the results of the phase-based method show that in all cases the algorithm captures the overall behavior of the system, systemic measurement under-prediction was observed, and it was clear that the signal processing embedded in the commercial Imetrum system yielded a more readily usable result.

Lessons Learned: Implications for Load Rating of Bridges Using Deflection Measurements

For trailing truck passes, Imetrum and string potentiometer resulted in similar midspan displacement readings for the first of two truck passes. The second of two truck passes of these pseudo-static loads resulted in max displacement that had a larger differential than the first of the trailing truck passes. The string potentiometer's difficulty rebounding during trailing truck passes is an example of error that can occur with physical instrumentation. This same error cannot occur from post-processing video recordings if the Imetrum cameras remain stationary for the duration of each load pass.

The discrepancy in deflection readings for the second of two trailing truck passes from the 1-911S load Tests 1 and 3 matched the results from the four trailing truck passes from the 1-213 bridge load test: Tests 1, 2, 5, and 6. Placing strain gauges on the top flange of girders would have helped with understanding how compositely the girder and concrete deck are acting. The lack of accessible 1-213 bridge plans and not having a strain gauge on one girder's top flange for the bridge load test impacted analysis and the ability to properly understand and model the bridge's in-situ condition.

Summary

Using the Imetrum VideoGauge™ system to obtain vision-based measurements provides a practical means to collect displacement measurements in a non-contact, accurate manner. The cameras and system controller are relatively easy to connect and set up to collect data, significantly reducing the time needed to attach sensors and run cabling for conventional wired systems used for structural monitoring. The Video Gauge™ software is quite robust but has a user-friendly graphical user interface (GUI) to aid in the setup, real-time viewing during a test, and post-processing the results. In addition to viewing the data on a screen during a test, video feeds of the test(s) can be saved in digital format to be replayed and archived. Having this feature helps to assure the user(s) of the data being collected and note any irregularities if they occur in real time. One challenge that can be overcome with the Imetrum system is the need to accurately calibrate planes that are used to assist point-to-point tracking. Calibrating planes requires mapping a 2D grid with known measurements onto a 2D plane within the field of view, which aids the point-to-point tracking process. Bullseye-like targets are used to provide a contrast of black and white concentric circles used to identify a known measurement (e.g., the perimeter of a square target with known dimensions) with a 2D plane in the field of view. Although not a prerequisite for the Imetrum system, placing targets on the structure within the field of view aids in the calibration process, which influences the accuracy of the measurements obtained. From this study, results revealed minimal differences between the measurements from the mounted sensors (i.e., string pots and strain gauges) versus the digital measurements using vision-based techniques to track displacements at the same locations.

Based on the two controlled bridge load tests, it was demonstrated that the Imetrum system can measure displacement magnitudes like readings captured by string potentiometers that are directly connected to the bridge. Different Imetrum cameras with varying lens focal lengths and standoff distances from targets measured the same displacement magnitudes. Setup time for the Imetrum system is significantly faster than mounting physical instrumentation, which was time-consuming for this case study like past studies. If there are enough known distances and dimensions of objects within a camera's field of view, displacements can be measured accurately. Reasonably accurate measurements were found to be captured from locations where there was graffiti or at locations where there is difference in texture (i.e., bolt patterns, blemishes, etc.) from the location where displacement is being tracked from the surrounding area. The results from this study showed how live-load distribution factors obtained from strain measurements compared favorably to the distributions obtained from vision-based displacement measurements for this bridge during a diagnostic load test. The use of computer vision and other vision-based measurements offer many options for conducting load tests and obtaining the necessary data without having direct contact on the bridge via mounted sensor arrays. The results from this study revealed the sensitivity and accuracy of the displacement measurement when compared to conventional string potentiometer readings when mounted directly to the flange of the girder. While there is not one optimal technique for measuring structural displacements based on a video, different techniques have different performance levels, and the applicability of these various methods may vary from case to case. The goal of this study was to compare the performance and accuracy of vision-based displacement measurements in the form of a field experiment on a bridge, and how the data can be used to calibrate finite element models to perform a more accurate load rating based on in-situ conditions.

The primary goal of the live-load testing was to confirm that the distribution factors per *AASHTO LRFD Bridge Design Specifications* (2020) were revealed to be conservative when compared to measured data obtained from non-contact, vision-based measurements that were used to calibrate a finite element model. Calculations to determine load ratings were also performed per AASHTO LRFR rating factors and compared to results obtained from vision-based measurements and strain readings obtained directly from load testing. Based on the findings, a procedure to evaluate live-load distribution and perform load ratings

may be possible based on the distribution of displacements using vision-based measurements that are simpler and require less time and resources to complete while being accurate and reliable. However, more research is needed to validate that displacement data obtained from non-contact, vision-based methods can be used to calibrate finite element models, which, in turn, can be used to better approximate live-load distributions and therefore perform a load rating using the AASHTO LRFR rating factors.

Recommendations for Future Work

Video-based measurements can be used to calibrate finite element bridge models and determine live-load distribution factors more accurately and in a non-contact way in cases where strain and displacement distributions are similar. LLDFs are needed to understand how the moments and forces are distributed, which is needed for load ratings used to evaluate existing bridges. It is known that the LLDF equations captured by *AASHTO LRFD Bridge Design Specification (2020)* tend to produce conservative values. Capturing vision-based measurements during load testing shows promise toward quantifying deformations needed to determine the live-load distribution based on in-situ conditions, which can differ from theoretical calculations due to unintended composite action, uncertain material properties, skew effects, and end fixity, to name a few. The Imetrum Dynamic Monitoring Station (DMS) has been shown to be a useful tool to accurately capture data and quantify displacements that may be used for evaluating bridges (and other structures) more efficiently and in a non-contact manner.

References

American Association of State Highway and Transportation Officials (AASHTO) (2020). *AASHTO LRFD Bridge Design Specifications*, 9th Edition, Washington, DC.

American Association of State Highway and Transportation Officials (AASHTO) (2018). *Manual for Bridge Evaluation*, 3rd edition, 2018 interim revisions. American Association of State Highway and Transportation Officials, Washington, DC.

Alipour, M., Washlesky, S.J., and Harris, D.K. (2019). Field Deployment and Laboratory Evaluation of 2D Digital Image Correlation for Deflection Sensing in Complex Environments. *Journal of Bridge Engineering*, 24(4):1–15. [https://doi.org/10.1061/\(ASCE\)BE.1943-5592.0001363](https://doi.org/10.1061/(ASCE)BE.1943-5592.0001363).

Al-Khateeb, H., Shenton, H.W. III, and Chajes, M.J. (2018). Computing continuous load rating factors for bridges using structural health monitoring data. *Journal of Civil Structural Health Monitoring*, 8:721–735.

Betti, R.M., Sloane, M.J., Khazem, D., and Gatti, C. (2016). Monitoring the structural health of main cables of suspension bridges. *Journal of Civil Structural Health Monitoring*, 6:355–363.

Brownjohn, J.M., Kripakaran, W.P., Harvey, B., Kromanis, R., Jones, P., and Huseynov, F. (2016). Structural health monitoring of short to medium span bridges in the United Kingdom, *Structural Monitoring Maintenance*, 3:259–276.

Cabaleiro, M., Riveiro, B., Conde, B., and Sanchez Rodriguez, A. (2020). A case study of measurements of deformations due to different loads in pieces less than 1 m from lidar data. *Measurement*, 151:107196.

Chen, J.G., Wadhwa, N., Cha, Y.-J., Durand, F., Freeman, W.T., and Buyukozturk, O. (2015). Modal identification of simple structures with high-speed video using motion magnification. *Journal of Sound and Vibration*, 345:58–71.

Chen, J.G., Davis, A., Wadhwa, N., Durand, F., Freeman, W.T., and Büyüköztürk, O. (2017). Video Camera-Based Vibration Measurement for Civil Infrastructure Applications. *Journal of Infrastructure Systems*, 23(3).

Das, S., and Saha, P. (2018). A review of some advanced sensors used for health diagnosis of civil engineering structures. *Measurement*, 129:68–90.

Doebling, S.W., Farrar, C.R., Prime, M.B., and Shevitz, D.W. (1996). Damage identification and health monitoring of structural and mechanical systems from changes in the vibration characteristics: A literature review. *The Shock and Vibration Digest*, 30, DOI:10.2172/249299.

Eom, J., and Nowak, A.S. (2001). Live Load Distribution for Steel Girder Bridges. *Journal of Bridge Engineering*, 6(6):489–497.

- Farrar, C.R., Darling, T.W., Migliori, A., Baker, W.E. (1999). Microwave interferometers for non-contact vibration measurements on large structures. *Mech Syst Signal Process*, 13:241–53.
- Harris, D. (2010). Assessment of flexural lateral load distribution methodologies for stringer bridges. *Engineering Structures*, 32(11):3443–3451. <http://doi.org/10.1016/j.engstruct.2010.06.008>
Retrieved from: <https://digitalcommons.mtu.edu/michigantech-p/6351>.
- Jafari, B., Khaloo, A., and Lattanzi, D. (2017). Deformation Tracking in 3D Point Clouds Via Statistical Sampling of Direct Cloud-to-Cloud Distances. *Journal of Nondestructive Evaluation*, 36(4):65.
- Kim, Y.J., Murison, E., and Mufti, A. (2010). Structural health monitoring: A Canadian perspective. *Proc Inst Civ Eng-Civ Eng*, 163:185–191.
- Kim, S., and Nowak, A.S. (1997). Load Distribution and Impact Factors for I-Girder Bridges. *Journal of Bridge Engineering*, 2(3):97–104.
- National Bridge Inventory (NBI) (2021). <<https://www.fhwa.dot.gov/bridge/nbi.cfm>>.
- NYSDOT (2007). *Reliability of visual inspection for highway bridges*. NYSDOT Engineering Division Office of Structures, Albany, NY.
- Poozesh, P., Sarrafi, A., Mao, Z., Avitabile, P., and Niezrecki, C. (2017). Feasibility of extracting operating shapes using phase-based motion magnification technique and stereo photogrammetry. *Journal of Sound and Vibration*, 407:350–366.
- Seo, J., Phares, B., Lu, P., Wipf, T., and Dahlberg, J. (2013). Bridge rating protocol using ambient trucks through structural health monitoring system. *Engineering Structures*, 46:569–580.
- Seo, J., Duque, L., and Wacker, J. (2018). Drone-enabled bridge inspection methodology and application. *Automation in Construction*, 94:112–126. 10.1016/j.autcon.2018.06.006.
- Shang, Z., and Shen, Z. (2018). Multi-point vibration measurement and mode magnification of civil structures using video-based motion processing. *Automation in Construction*, 93:231–240.
- Shenton, H.W. III, Al-Khateeb, H.T., Chajes, M.J., and Wenzel, G. (2017). Indian River Inlet Bridge (Part A): Description of the bridge and the structural health monitoring system. *Bridge Structures* 13(1):3–13.
- Stanbridge, A.B., Martarelli, M., and Ewins, D.J. (2000). Measuring area vibration mode shapes with a continuous-scan LDV. *Proc. SPIE 4072, Fourth International Conference on Vibration Measurements by Laser Techniques: Advances and Applications*, (22 May 2000). <https://doi.org/10.1117/12.386746>.
- Sohn, H., Farrar, C.R., Hemez, F., and Czarnecki, J. (2001). A review of structural health. *Library.Lanl.Gov*, 1–7. <https://library.lanl.gov/cgi-bin/getfile?00796820.pdf>
- Sony, S., Laventure, S., and Sadhu, A. (2019). A literature review of next-generation smart sensing technology in structural health monitoring. *Structural Control and Health Monitoring*, 26(3):e2321_eprint: <https://onlinelibrary.wiley.com/doi/pdf/10.1002/stc.2321>.

- Sun, L., Shang, Z., Xia, Y., Bhowmick, S., and Nagarajaiah, S. (2020). Review of Bridge Structural Health Monitoring Aided by Big Data and Artificial Intelligence: From Condition Assessment to Damage Detection. *Journal of Structural Engineering*, 146(5):04020073.
- Timber, L. (2022). Live Load Distribution and Evaluation of Bridges Using Digital Image Measurements. Master's thesis, Department of Civil and Environmental Engineering, University of Delaware.
- Transportation Research Board (TRB) (2019). *Primer on Bridge Load Testing*. Transportation Research Circular, Number E-C257, November 2019.
- Wadhwa, N., Rubinstein, M., Durand, F., and Freeman, W.T. (2013). Phase-based video motion processing. *ACM Transactions on Graphics*, 32(4):1.
- Xu, Y., and Brownjohn, J.M.W. (2018). Review of machine-vision based methodologies for displacement measurement in civil structures. *Journal of Civil Structural Health Monitoring*, 8(1):91–110.
- Yang, Y., Dorn, C., Mancini, T., Talken, Z., Kenyon, G., Farrar, C., and Mascareñas, D. (2017). Blind identification of full-field vibration modes from video measurements with phase-based video motion magnification. *Mechanical Systems and Signal Processing*, 85:567–590.
- Ziolkowski, P., Szulwic, J., and Miskiewicz, M. (2018). Deformation Analysis of a Composite Bridge during Proof Loading Using Point Cloud Processing. *Sensors*, 18(12):4332.
- Zokaie, T. (2000). AASHTO-LRFD Live Load Distribution Specifications. *Journal of Bridge Engineering*, 5(2):131–138.